Ph. D. Dissertation

Spin Dynamics of Magnetic Nanoparticles and Its Application for Magnetic Hyperthermia

자성 나노 입자의 스핀 동역학과 이를 이용한 자성 온열 치료 응용 연구

by

Min-Kwan Kim

February 2018

Department of Materials Science and Engineering

College of Engineering

Seoul National University

ABSTRACT

Spin dynamics of magnetic nanoparticles and its application for magnetic hyperthermia

Min-Kwan Kim
Department of Materials Science and Engineering
The Graduate School
Seoul National University

Localized magnetic particle hyperthermia heating treatment using magnetic nanoparticles continue to be an active area of cancer research. In magnetic hyperthermia, magnetic nanoparticles are subjected in alternating magnetic field, thus forced to release energy-dissipation as a heat (via various mechanisms: Néel-Brown relaxation, hysteresis loss) in their surrounding while neighboring cancer cells undergo severe thermal shock and potential destruction. One of the critical issues of the mechanisms for describing the conventional hyperthermia treatment is relatively low heating power, which is not enough to kill cancer cells. To improve the heating performance of magnetic nanoparticles, there have been numerous researches using various analysis methods. However, since the mechanism of heat generation from magnetic nanoparticles is not newly proposed, the reported researches have limitations on the degree of improvement in heating power. Here, we have proposed a new mechanism for the energy-dissipation of magnetic nanoparticles based on resonance of collective spin dynamics that can maximize the heating power.

First, we explored robust non-linear magnetization dynamics and the associated

high-efficiency energy-dissipation effect in single-domain soft magnetic nanospheres, as excited by oscillating magnetic fields of different frequencies and amplitudes under given static magnetic fields. We conducted micromagnetic simulations to explore the novel magnetization dynamics of soft magnetic particles and additional analytical derivations of the energy-dissipation rate for the steady-state regime by varying the frequency and strength of rotating magnetic fields for different Gilbert damping constants and static magnetic field strengths. All of the simulation results and analytical calculations agree well quantitatively. The dynamic origin of such a high-efficiency energy-dissipation mechanism is completely different from those of the typical ones used in bio-applications.

Furthermore, we have extended the object of the energy-dissipation study by the magnetic resonance phenomenon from the single-domain state to the magnetic-vortex state. Using both micromagnetic simulations and semi-analytical analysis, we addressed the similarities and differences between the single-domain state and magnetic-vortex state in terms of the temporal evolutions of the spin dynamics and energy-dissipation calculated for all variables given to the system. The energy-dissipation generated by resonant excitation of magnetic vortex was smaller than the energy-dissipation of single-domain state, and it is directly related to $\langle m_{\Gamma} \rangle$, where $\langle m_{\Gamma} \rangle$ is the average magnetization component over the sphere volume in the vortex-core orientation.

Finally, we identify the existence of spin-dynamics driven energy-dissipation in magnetic nanoparticles from ferromagnetic resonance experiments using vector network analyzer and compare the results with analytical calculation and

micromagnetic simulation. From the experiments, we observed that the energy-dissipation released by the resonance of spins inside the nanoparticles well corresponded to the calculated results.

This work provides further insights into the fundamentals of magnetization dynamics in magnetic particles and the associated energy-dissipation effect, and suggests a highly efficient means of magnetic-hyperthermia-applicable energy dissipation.

Keywords: Magnetic nanoparticle, energy-dissipation, resonance, single-domain, magnetic-vortex, micromagnetic simulation, vector network analyzer.

Student Number: 2011-20626

Table of Contents

List of Tables

List of Figures

(uniform magnetization) and external static field and time-varying circular-rotating field. $\mathbf{H}_{rot}$ is always on the plane perpendicular to the static field direction. Three torque terms $\boldsymbol{\tau}_{stat}$, $\boldsymbol{\tau}_{rot}$, and $\boldsymbol{\tau}_{damp}$ are displayed acting on **m** with θ, which are the angles between **m** with $\mathbf{H}_{stat}$,. The angle that shows the phase delay of **m** from $\mathbf{H}_{rot}$, ϕ, also is displayed. Temporal evolution of x (black), y (red), and z (blue) -components of (b) $\boldsymbol{\tau}_{rot}$ (c) $\boldsymbol{\tau}_{damp}$ for different strengths of circular-rotating fields H_{AC} = 4, 5, and 6 in resonant case (f_{CCW} = 280 MHz). (d) Steady-state values of z-components of $|\boldsymbol{\tau}_{rot}|$ and $|\boldsymbol{\tau}_{damp}|$ as function of H_{AC}. (e) Steady-state values of θ, ϕ as functions of H_{AC}. The symbols denote the micromagnetic simulation results, while the solid lines correspond to the analytical calculation data. The static field strength H_{DC} = 100 Oe and damping constant α = 0.05 were used for all of the simulations shown in this figure.

Figure 3.4. Temporal evolution of energy-dissipation rate, Q, (solid line) and its time average $\langle Q \rangle$ (dashed line) for excitation of Py nanosphere of diameter $2R$ = 20 nm by H_{AC} = 5 Oe, H_{DC} = 100 Oe, α = 0.05, for (a) non-resonant case (f_{CCW} = 200 MHz) and (b) resonant case ($f_{CCW} = f_L$ = 280 MHz). The intervals between 0.1 ns and 100 ns are distinguished by the gray color.

Figure 3.5. Temporal evolution of energy-dissipation rate (blue), negative dual power density (red), and negative time derivative of total energy density (black) for excitation of Py nanosphere of diameter $2R$ = 20 nm by H_{AC} = 5 Oe, H_{DC} = 100 Oe, α = 0.05, for (a) non-resonant case (f_{CCW} = 200 MHz) and (b) resonant case ($f_{CCW} = f_L$ = 280 MHz).

Figure 3.6. Energy-dissipation rate in steady-state regime as function of frequency of

Chapter 1

General Introduction

Magnetic hyperthermia is the research field of treating cancer by applying heat to tumor cells using magnetic nanoparticles and AC magnetic field. This method could be promising to treat small or deeply located tumors. Magnetic hyperthermia using magnetic nanoparticles is a multidiscipline research field which requires the cooperation of physics, chemistry, and biology. This technique, which developed in 1957 [1-2], where maghemite nanoparticles (γ-Fe_2O_3) were used, is based on the report that tumor cells could be destroyed by heating the cells for a duration of time to temperature between 43 and 46 °C while normal cells are less affected [3,4]. The heat tumor cells is enabled by the application of AC magnetic field of suitable amplitude and frequency. One of the major topics that is being studied in magnetic hyperthermia is the reduction of the amount of magnetic nanoparticles that could be used in living organs [3,4]. As shown in Fig. 1.1, if magnetic nanoparticles (typically Fe_3O_4) are put inside a tumor cells and the patient is placed in an alternating magnetic field, the temperature of tumor cells will rise. The temperature elevation causes tumor

oxygenation and radio- and chemosensitivity, hopefully destroying tumors [3]. As in many other research fields—namely materials science [5], energy [6], or health [7] — the progresses made in nanoscience have taken magnetic hyperthermia to a much higher degree of technology. For example, the application of magnetic nanoparticles is moving towards targeting human body areas otherwise difficult to reach, and chemical manipulation at the nanoscale has invested the ability to bound biomolecules like antibodies for a more effective treatment or to accomplish specific targeting. In this manner, magnetic nanoparticles may simultaneously combine several theranostic functionalities such as drug-carriers [8], contrast agents for MRI [9] and/or magnetic heating agents [10].

1.1. Research Objectives

The main practical problem with magnetic hyperthermia is an inadequate magnetic particle supply to the tumor cells [11]. In the case of intra-tumoural injection inhomogeneity of magnetic nanoparticle distribution within the tissue may cause local temperature differences that do not allow the degradation of hyperthermia and thermoablation of tumor. As a result of insufficient temperature increase in some of the tumor there is a risk of multiplying of surviving tumor cells. In this reason, the energy-dissipation or heating efficiency of magnetic nanoparticles should be enhanced to realize high temperature magnetic hyperthermia. In addition, it is desirable to achieve the temperature enhancement needed with as low as possible amount of magnetic nanoparticles. This means that the heat power generated per particle unit mass (specific

loss power, SLP) should be as high as possible. This is particularly important for applications where target concentration is very low as for instance in antibody targeting of tumors [11]. In detail, Fig. 1.2 shows how the SLP needed to obtain a temperature increase of 15 K (which represents the ablation temperature of tumor cells) depends on tumor radii for three different particle concentrations: A typical magnetic nanoparticle concentration is assumed 10 mg magnetic nanoparticle per mL of tumor cells for antibody targeting supply [11]. It can be seen that by antibody targeting of conventional magnetic nanoparticle (typically Fe_3O_4) with SLP of a few 100 W/g, the thermoablation treatment of tumors larger than 8 mm seems promising. However, the heating effect of magnetic nanoparticle applied by antibody targeting is unrealistic for tumors smaller than 3 mm which is the diagnostic limit. The visionary idea of the antibody targeting is the automatic supply of tumor cells smaller than the radius of diagnostic limit. This loading could be obtained by specific binding of systemically applied antibody-labelled nanoparticle to the corresponding tumor cells [11] with the aim of destroying undetected tumor cells with the help of hyperthermia. As shown in Fig. 1.2, heating with magnetic particle concentration of 1 mg/mL particles with a SLP of almost several 1000 W/g are required. However these results suggest that magnetic hyperthermia for tumors in the size range of diagnostic limit seems to be impossible due to the unrealistically large amount of energy-dissipation necessary to obtain a appropriate temperature increase.

To improve the heating performance of magnetic nanoparticles, there have been numerous researches using various analysis methods [12-14]. However, since the mechanism of heat generation from magnetic nanoparticles has not newly proposed,

the reported researches have limitations on the degree of improvement in heating power [11]. In this thesis, we propose a new mechanism for the energy-dissipation of magnetic nanoparticles based on resonance of collective spin dynamics that can maximize the heating power. First, we explored robust non-linear magnetization dynamics and the associated high-efficiency energy-dissipation effect in soft magnetic nanospheres in single-domain states, as excited by oscillating magnetic fields of different frequencies and amplitudes under given static magnetic fields. We conducted micromagnetic simulations to explore the novel magnetization dynamics of soft magnetic particles and additional analytical derivations of the energy-dissipation rate for the steady-state regime by varying the frequency and strength of rotating magnetic fields for different Gilbert damping constants and static magnetic field strengths. All of the simulation results and analytical calculations agree well quantitatively. Next, we have extended the object of the energy-dissipation study by the magnetic resonance phenomenon from the single-domain state to the magnetic-vortex state. Using both micromagnetic simulations and semi-analytical analysis, we addressed the similarities and differences between the single-domain state and magnetic-vortex state in terms of the temporal evolutions of the spin dynamics and energy-dissipation calculated for all variables given to the system. Finally, we identify the existence of spin-dynamics driven energy-dissipation in magnetic nanoparticles from vector network analyzer experiments and compare the results with analytical calculation and micromagnetic simulation. From the experiments, we observed that the energy-dissipation released by the resonance of spins inside the nanoparticles well corresponded to the calculated results.

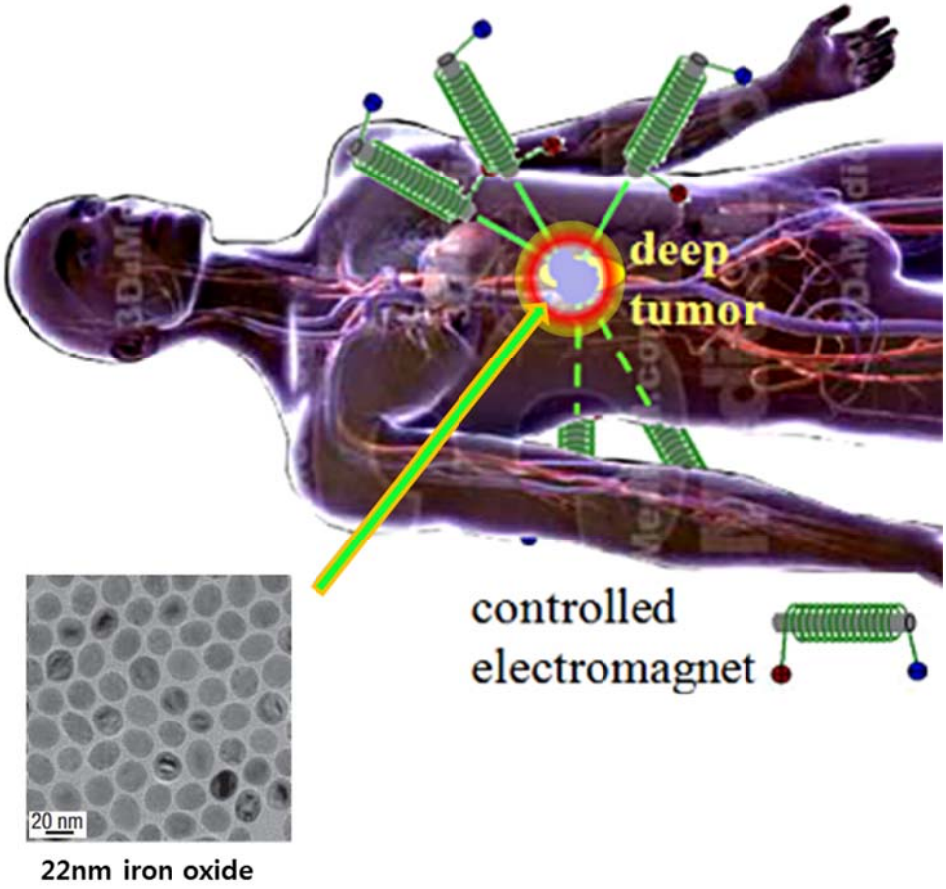

Fig. 1.1. Schematic of the magnetic hyperthermia. The magnetic nanoparticles (typically iron oxide) are put inside deep tumor and the whole patient is placed in an alternating magnetic field, the tumor temperature will rises.

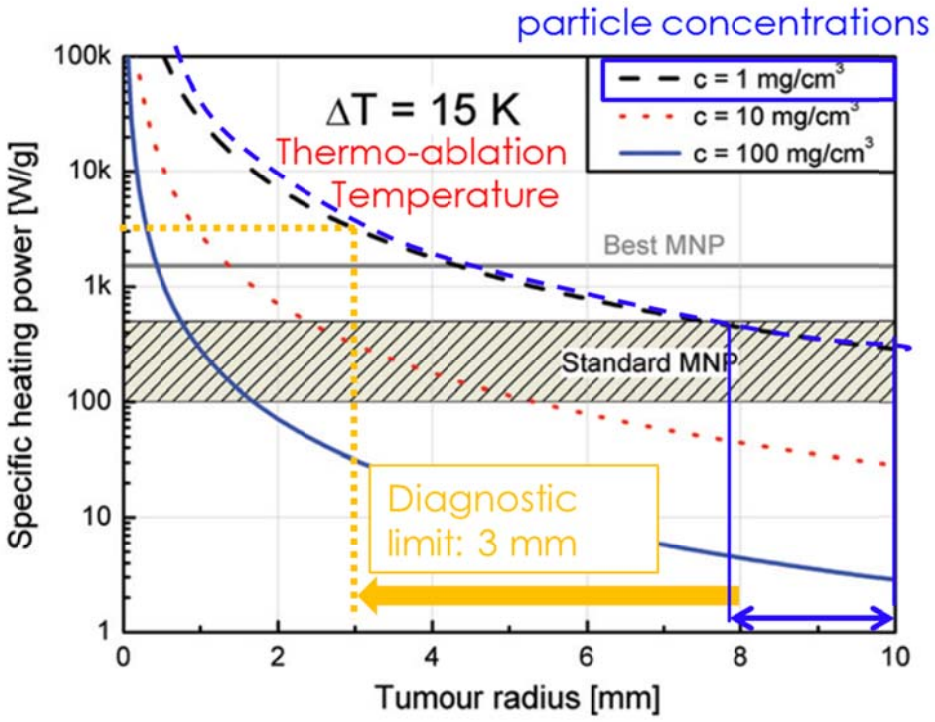

Fig. 1.2. Heating power demand in dependence on tumor size to realise a temperature increase of 15 K for different magnetic nanoparticle concentrations in the tumor tissue. [11]

1.2. References

[1] R. K. Gilchrist, W. D. Shorey, R. C. Hanselman, and J. C. Parrott, Ann. Surg., **146**, 596 (1957)

[2] I. M. Obaidat, B. Issa, and Y. Haik, Nanomater, **5**, 63 (2015).

[3] A. Jordan, R. Scholz, P. Wust, H. Schirra, T. Schiestel, H. Schmidt, and R. Felix, J. Magn. Magn. Mater., **194**, 185 (1999).

[4] P. Moroz, S. K. Johns, and B. N. Gray, Int. J. Hyperth, **18**, 267 (2002).

[5] S. Laurent, S. Dutz, and U. O. Häfeli, Adv. Colloid Interface Sci., **166**, 8 (2011).

[6] H. Jung, Y. S. Choi, K. S. Lee, D. S. Han, Y. S. Yu, M. Y. Im, P. Fischer and S. K. Kim, Acs Nano **6**, 3712 (2012).

[7] D. A. Allwood, G. Xiong, C. C. Faulkner, D. Atkinson, D. Petit and R. P. Cowburn, Science **309**, 1688 (2005).

[8] G. Vallejo-Fernandez, O. Whear, A. G. Roca, S. Hussain, H. Timmis, V. Partel, and K. O'Grady, J. Phys. D., **10**, 312001 (2013)

[9] A. E. Deatsch, and B. A. Evans, J. Magn. Magn. Mater., **354**, 163 (2014)

[10] C. L. Dennis, and R. Ivkov, Int.J. Hyperth., **29**, 715 (2013).

[11] R. Hergt, and Si. Dutz, J. Magn. Magn. Mater., **311**, 187 (2007).

[12] V. Pilati, R. C. Gomes, G. S. Gomide, P. Priscilla, F. G. Silva, F. L. O. Paula, R. Perzynski, G. F. Goya, R. Aquino, and J. Depeyrot, J. Phys. Chem. C, **10**, 1021 (2018).

[13] J. Rácz, P. F. de Châtel, I. A. Szabó. L. Szunyogh, and I. Nándori, Phys. Rev.

E, **93**, 012607(2016).

[14] B. Mehdaoui, A. Meffre, J. Carrey, S. Lachaize, L. -M. Lacroix, M. Gougeon, B. Chaudret, and M. Respaud, Adv. Funct. Mater., **21**, 4573 (2011).

Chapter 2

Research Background

2.1. Size Dependent Properties of Magnetic Nanoparticles

2.1.1. Spin Configurations

Based on the response of the magnetization of magnetic nanoparticles and the net magnetization in the applied magnetic field, magnetic systems are typically classified as being either single-spin, superparamagnetic [1,2], single-domain, magnetic-vortex, multi-domain state [3]. Figure 2.1 shows the spin arrangement for each of these types of magnetic nanoparticles. Below certain critical dimension (about 15 ~ 20 nm diameter), magnetic nanoparticles exhibit magnetic responses reminiscent of those of paramagnetic materials, which is a zero average magnetic moment in the absence of an external field and a rapidly increasing (as compared to paramagnetic materials) magnetic moment under application of an external field in the direction of the field. In

this case where the magnetization of the magnetic particle over the measurement/observation interval is equal to zero in the absence of an external field, such nanoparticles are referred to as superparamagnetic. This phenomenon, observed at temperatures above the so-called blocking temperature, arises from the thermal fluctuations within the nanoparticles being comparable to or greater than the energy barrier for moment reversal, allowing rabid random flipping of the nanoparticle magnetic moments (see Fig. 2.1). Superparamagnetism is especially important in applications such as drug delivery or MRI, where the nanoparticles exhibit no magnetic properties upon removal of the external field and therefore have no attractioin for each other, eliminating the major driving force for aggregation. More importantly, superparamagnetic nanoparticles allow better control over the application of their magnetic properties because they provide a string response to an external magnetic field [4-8].

If the size of magnetic nanoparticle is increased up to a critical size, the magnetic nanoparticles tend to develop as single-domain structure. The single-refers to the state of a ferromagnet in which the magnetization does not vary across the magnet. As shown in Fig. 2.2, if a particle is in the single-domain state, all of its internal magnetization is pointed in the same direction, uniform magnetization. It therefore has the largest possible magnetic moment for a particle of that size. Because the magnetic nanoparticles of single domain state have a high magnetic moment, they are very important in a lot of applications [9]. They are the main source of hardness in hard magnets, the carrier of magnetic storage in tape drives, and recently have been applied into bio-applications that generate strong signals.

For a magnetic nanoparticle without any external forces, the spin configurations are determined mainly by the competition between the exchange energy, which favors spins being parallel to their neighbors, and the magnetostatic energy, which favors spins forming a closed structure to prevent free magnetic poles from generating stray magnetic fields outside the nanoelement. As size of magnetic nanoparticle increases, as shown in Fig. 2.2, the magnetizations are aligned along the boundary of sphere, forming an *y*-*z*-plane curling structure along the *x*-axis to avoid a free pole. However, this continuous variation of the magnetic structure costs exchange energy, which wants variation between adjacent spins. The exchange energy cost increases closer to the *x*-axis inside nanoparticle. Along the *x*-axis, the variation of the magnetization will be relatively high and, as a result, the exchange energy will be high. To stabilize this exchange energy [3], the vortex-core develops along *x*-axis (see Fig. 2.2). This 3D magnetic elements have attracted growing interest, due to their characteristic properties that originate from 3D geometries and their potential applications to memory devices and bioapplications [3, 10-11].

2.1.1. Characteristic Frequencies of Magnetic Nanoparticles

Due to the interactions between magnetic moments in the nanoparticles and external magnetic field, the magnetic nanoparticle has characteristic frequency (resonant frequency) for precessional motion of its spin structure. Understanding the characteristic frequency of magnetic nanoparticle is of significant fundamental and applied interest because theses frequencies allow for more efficient means of activate

spins inside particle. The characteristic frequencies in the magnetic nanoparticles are crucially depending on the spin configuration inside nanoparticle [3, 11]. Since we focused on isotropic sphere system in this theses, only characteristic frequencies for the corresponding system is described in this chapter.

A. Larmor Frequency [12]

The characteristic frequency of precessional motion for single spin, in general, is well known as Larmor frequency. In physics, Larmor precession is the precession of the spin about an external magnetic field (see Fig. 2.3). Spins with a magnetic moment also have angular momentum and effective internal electric flow proportional to their angular momentum. The external magnetic field exerts a torque on the magnetic moment [12],

$$\boldsymbol{\tau} = \boldsymbol{\mu} \times \mathbf{H} = \gamma \mathbf{J} \times \mathbf{B}, \quad (2.1)$$

where $\boldsymbol{\tau}$ is the torque; $\boldsymbol{\mu}$ is the magnetic dipole moment of single spin, **J** is the angular momentum vector, **H** is the external magnetic field, $\times$ means the cross product, and γ is the gyromagnetic ratio of magnetic moment and the angular momentum. The phenomenon is similar to the precession of a tilted classical gyroscope in an external torque-induced by gravitational field. Finally, the **J** precesses about the external static field axis with an angular frequency derived as the characteristic frequency (Larmor frequency),

$$\omega_{\mathrm{L}} = \gamma H. \qquad (2.2)$$

This Larmor precession has very crucial roles in a rich variety of spin- dynamics such

as resonance of electron-spin, intrinsic resonance of nuclei, ferromagnetic resonance, and related magnetization dynamics [13-18]. Such dynamic fundamentals have been widely utilized in a variety number of applications, including material analysis [13, 16], MRI [17,18], and data storage in magnetic media [19,20].

For the isotropic sphere system, the spins inside nanoparticles which have spin configuration of superparamagnetic or single-domain state could be considered as one single spin (e.g. macrospin). So we can consider the characteristic frequencies of those spin configuration as a Larmor frequency.

B. Characteristic Frequency of Precessional Motion of Magnetic-vortex [3]

As reported by S.-K. Kim et al [3], the characteristic frequencies of magnetic-vortex in soft magnetic nanoparticles of spherical shape is totally different against superparamagnetic or single-domain nanoparticles. For the magnetic-vortex structures in Fig. 2.2, when a sizable static field H_{DC} is applied in the +z-direction, the vortex cores for 40 nm < 2R < 150 nm start to reorient to the field direction, but with accompanying precession motions. This precession motion is different from well-known Larmor precession and even the gyration of vortex cores in planar dots [21, 22]. Although very weak spin waves are emitted inside the nanospheres, the vortex's spin configurations are maintained as a whole structure, because the field strength is sufficiently small. In the relaxation process, the core orientation converges in the field direction (+z-direction), reflecting the fact that the m_x averaged over the entire volume of the sphere, $\langle m_x \rangle$, undergoes decaying oscillation through its vortex-core

precession (inset of Fig. 2a.). The precession frequency was obtained by Fast Fourier Transformation (FFT) of the temporal $\langle m_x \rangle$ evolution for the different values of $2R$ and H_{DC} (see Fig. 2.4(a) and (b), respectively). In the cases of uniformly saturated particles (single-domain state, $2R$ = 10, 20 or 30 nm), the frequency independent of $2R$, as determined by the Larmor frequency, Eq (2.2). By contrast, for the vortex-state spheres (40 nm < $2R$ < 120 nm), the precession frequency of a vortex core showed a strong variation with $2R$, as can be expressed by

$$\omega_{MV} = \gamma_{eff} H \quad (2.3)$$

where γ_{eff} is the effective gyromagnetic ratio, which is variable with the sphere diameter. The analytical calculations of characteristic frequencies for magnetic-vortex state are described in the appendix in this chapter.

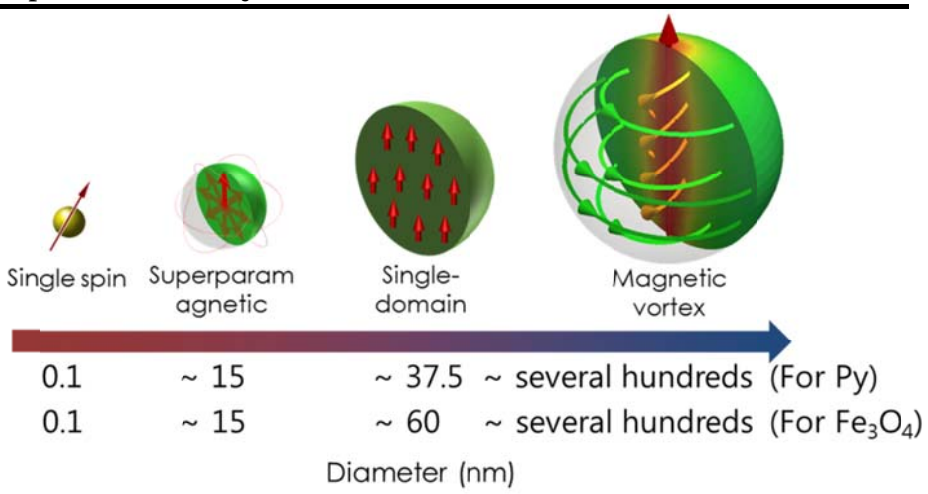

Fig. 2.1. Magnetization configurations of spherical magnetic nanoparticles according to the diameter for Py and Fe_3O_4.

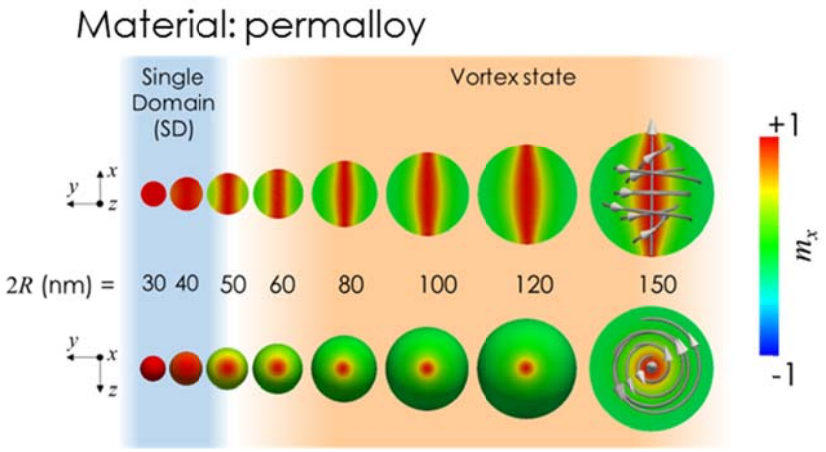

Fig. 2.2. Ground-state magnetization configurations of Py nanospheres according to the diameter as indicated: upper, viewed from positive *z*-direction and sliced across *x*-*y* plane; lower, viewed from positive x-direction and sliced across y-z plane. The color represents the x-component of the local magnetizations, mx = Mx/Ms (see the color bar). The arrows inside the sphere of 2*R* = 150 nm represent the local curling magnetizations. [3]

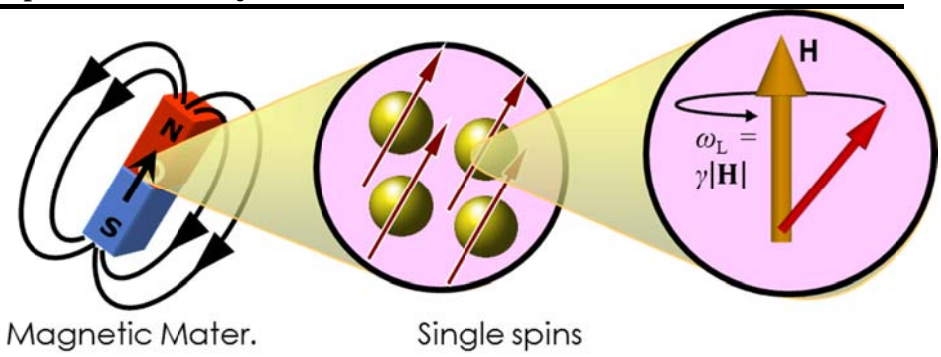

Fig. 2.3. Schematic diagram of Larmor precession motion.

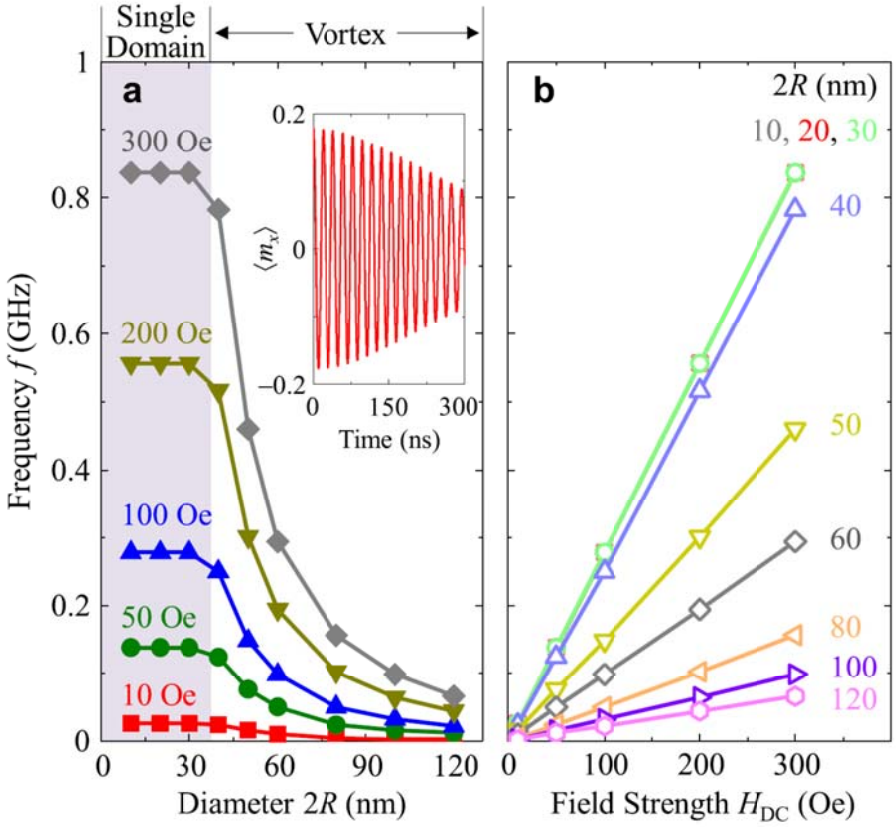

Fig. 2.4. Precession frequency of Py nanospheres as functions of (a) $2R$ and (b) H_{DC} applied in +z-direction (perpendicularly to initial vortex-core orientation). The inset in (a) shows the $<m_x>$ oscillation versus time, for a sphere of $2R$ = 80 nm. In (a), uniform single-domain and vortex states are distinguished at about $2R$ = 37 nm by the gray color. The symbols indicate the micromagnetic numerical calculations, with corresponding lines drawn by eye. In (b), the lines are the results of linear fits for the individual diameters, as indicated. [3]

2.2. Numerical Calculations for Spin Dynamics

2.2.1. Micromagnetics

A. Micromagnetic Energy

Ferromagnetic materials exhibit the important property of long range magnetic order. Fundamentally, this arises from a quantum mechanical effect called the exchange interaction, which forces neighboring atomic spins to be aligned in parallel under certain circumstances. From the Heisenberg model [23], the exchange interaction between neighboring atomic spins can be expressed as

$$\mathbf{H}_{\text{ex}} = -2\sum_{i>j} J_{i,j}\mathbf{S}_i \cdot \mathbf{S}_j, \quad (2.4)$$

where $J_{i,j}$ is referred to as the exchange integral, and $\mathbf{S}_{i,j}$ denotes the spin operator that acts on i^{th} and j^{th} atoms. The sign of J depends on the interatomic distances and can be positive or negative. The sign of J is responsible for parallel or antiparallel spin alignment. Such an exchange integral involves the overlap between wave functions, and its strength decreases very rapidly with increasing distance between ions. Accordingly, this energy, in principle, is only effective on a length scale of sub-nanometers.

The Heisenberg Hamiltonian is isotropic and hence, the magnetic properties should also be isotropic. However, in a real crystal, due to the coupling between the electron orbital angular momentum and spin, spins prefer to be aligned in along certain crystallographic axes. Such direction-dependent energy originates from spin-orbit

coupling and is called magnetocrystalline anisotropy energy. Meanwhile, there is a classical interaction among dipoles, called magnetostatic interaction. In contrast to the exchange interaction, which is dominant only in a short range, the magnetic dipoles play an important role in long-range characteristic within a ferromagnet.

In a realistic model, since the static and dynamic behavior of magnetic materials is determined by competition between all energy terms, all three energy terms should be taken into account. However, there is a major problem when relating fundamental atomic spin to a macroscopic magnetic moment [2]: for the case of exchange interactions, the atomic spin model is adequate, but, for the case of the magnetostatic interaction, this approach is unsuitable. Micromagnetics provides a way to overcome the gap between two different frameworks, the macroscopic Maxwell theory of electromagnetics and the atomic-level quantum theory, by imaging the atomic spins are a vector magnetization **M** whose direction varies continuously with position. Then Eq. (2.5) can be written as

$$E_{\text{ex}} = -2JS^2 \sum_{i>j} \phi_{i,j}, \qquad (2.5)$$

where $\phi_{i,j}$ is the angle difference between two neighboring magnetizations. Here, if we get, for small angles

$$\left|\phi_{i,j}\right| \approx \left|m_i - m_j\right| \approx \left|(r_i \cdot \nabla)m\right|, \qquad (2.6)$$

Changing the summation over i to an integral over the volume, the exchange interaction can be rewritten as

$$E_{\text{ex}} = \int_V A\{(\nabla m_x)^2 + (\nabla m_x)^2 + (\nabla m_x)^2\} d^3r, \qquad (2.7)$$

where A is the exchange constant, where is given as $A = nJS^2 / a$. Here a is the

lattice parameter, and n is 1, 2, and 4 for a simple cubic, body-centered, and face-centered structure, respectively.

There are several kinds of magnetic anisotropies that vary according to their origins. The most common type of anisotropy is magnetocrystalline anisotropy. Magnetocrystalline anisotropy results from spin-orbit coupling, and this, in general, can be expressed in terms of a series expansion of the directional cosine of the local magnetization moment, $\mathbf{m} = (m_x, m_y, m_z)$, relative to the crystalline axis in a lattice. In a hexagonal crystal, for example, the direction of easy magnetization, the easy axis, is the c-axis, and all directions in the basal plane are equally hard. Then, the anisotropy energy depends on only one parameter, the angle, θ, between the magnetization and the c-axis. This type of anisotropy is called uniaxial. In this case, the anisotropy of the system could be derived as

$$E_{\text{ani}} = \int_V K_0' + K_1' \cos^2\theta + K_2' \cos^4\theta dV \,. \quad (2.8)$$

Using the relation, $\cos^2\theta = 1 - \sin^2\theta$, one can rewrite the Eq. (2.8) in the more typical form

$$E_{\text{ani}} = \int_V K_0 + K_1 \sin^2\theta + K_2 \sin^4\theta dV \,. \quad (2.9)$$

Here, K_0, K_1, and K_2 are anisotropy constants for corresponding materials at a given temperature.

In a cubic crystal system, the magnetocrystalline anisotropy energy density is given by

$$E_{\text{ani}} = \int_V K_0 + K_1\left(a_1^2a_2^2 + a_2^2a_3^2 + a_3^2a_1^2\right) + K_2a_1^2a_2^2a_3^2 dV \,, \quad (2.10)$$

where a_1, a_2, and a_3 are the directional cosines of the local magnetization, **m**.

The magnetostatic interaction can be understood as the interaction of the local

magnetization with the magnetic field, called the demagnetizing field, produced by its magnetization configuration. The magnetostatic interaction energy could be expressed by the basic differential laws of electromagnetics,

$$\nabla \cdot \mathbf{B} = 0 , \quad (2.11)$$

$$\nabla \times \mathbf{H} = \mathbf{J} , \quad (2.12)$$

where **J** is current density inside the material. If the current density, **J**, vanishes in some finite region, the right side in Eq. (2.12) becomes zero. Then, we can introduce a magnetic scalar potential, $\mathbf{H} = -\nabla\phi$. Substituting the magnetic scalar potential into Eq. (2.12), a magnetostatic Poisson equation analogous to that in electrostatics can be derived as

$$\nabla^2\phi = -\rho \quad . (2.13)$$

Here, $\rho = -\nabla \cdot \mathbf{M}$ is the magnetic volume charge density. Then, the magnetostatic potential energy is

$$\phi = \frac{1}{4\pi}\int_{\text{all}} \frac{\rho(\mathbf{r}')}{|\mathbf{r}-\mathbf{r}'|} dV' . \quad (2.14)$$

If the system has a finite volume *V*, the system should reach particular boundary conditions at its surfaces. The boundary conditions can be derived from application of the divergence and Stokes theorem to Eq. (2.11) and (2.12), respectively. This reveals that there are effective magnetic surface charges, defined as $\sigma = \mathbf{n} \cdot \mathbf{M}$, where **n** is the unit vector normal to the surface of the element. Then, the total magnetostatic potential energy for the system with a finite volume *V* and surface *S* can be expressed as

$$E_{\text{ms}} = \frac{1}{4\pi}\int_V \frac{\rho(\mathbf{r}')}{|\mathbf{r}-\mathbf{r}'|} dV' + \frac{1}{4\pi}\int_S \frac{\sigma(\mathbf{r}')}{|\mathbf{r}-\mathbf{r}'|} dS' . \quad (2.15)$$

Eq. (2.15) reveals that the magnetostatic energy increases with increasing magnetic

surface and volume charge density. Therefore, the magnetostatic interactions lead to a state with less magnetic surface and volume charges, as expected from the magnetic charge and pole-avoidance principle.

In the presence of an external magnetic field, $\mathbf{H}_a$, there is another type of interaction between the magnetic moment, m, and the field. The applied field makes the magnetic moments align along the applied field direction. This interaction between the external magnetic field and the magnetic moments is called the Zeeman interaction. This type of interaction can be simply expressed as

$$E_{\text{Zeem}} = -\mu_0 \int_V \mathbf{M} \cdot \mathbf{H}_a dV \,. \quad (2.16)$$

B. Magnetic Equilibrium and Brown's Equations

The magnetic equilibrium state is realized by minimizing the total energy of the system,

$$\begin{aligned} E_{\text{total}} = & \int_V \left[A\left(\nabla \mathbf{m}\right)^2 + E_{\text{ani}} - \mu_0 \mathbf{M} \cdot \mathbf{H}_{\text{a}} - \frac{1}{2}\mu_0 \mathbf{M} \cdot \mathbf{H}_{\text{d}} \right] dV \\ & + \int_S \frac{1}{2} K_{\text{s}} \left(\mathbf{n} \cdot \mathbf{m}\right)^2 dS, \end{aligned} \quad (2.17)$$

where $\mathbf{H}_{\text{a}}$ and $\mathbf{H}_{\text{d}}$ denote the applied magnetic field and demagnetizing field, respectively, and E_{ani} is the magnetic anisotropy energy. The second integral on right side in Eq. (2.17) represents the surface anisotropy energy, where **n** denotes the surface normal and K_S is the surface anisotropy constant [24].

For the equilibrium state, since the total energy occurs at the stationary point, the functional variation of total energy should be zero. The first-order functional variation

of the total energy is

$$\begin{aligned}\delta E_{\text{total}} = &\int_V \left[2\nabla\cdot\left(A\nabla\mathbf{m}\right) + \frac{\partial E_{\text{ani}}}{\partial \mathbf{m}} + \mu_0 M_{\text{s}}\mathbf{H}_{\text{a}} - \mu_0 M_{\text{s}}\mathbf{H}_{\text{d}} \right]\cdot\delta\mathbf{m}dV \\ &+ \int_S \left[2A\frac{\partial \mathbf{m}}{\partial \mathbf{n}} + K_{\text{s}}\mathbf{n}\cdot\mathbf{m}\mathbf{n} \right]\cdot\delta\mathbf{m}dS\end{aligned} \tag{2.18}$$

Since the variation $\delta\mathbf{m}$ satisfies the constraint $|\mathbf{m} + \delta\mathbf{m}| = 1$, the possible variations of $\delta\mathbf{m}$ are $\delta\mathbf{m} = \mathbf{m} \times \delta\boldsymbol{\theta}$, where $\delta\boldsymbol{\theta}$ denotes a small vector rotation. Then, after some simple vector calculus, Eq. (2.18) can be rewritten as

$$\begin{aligned}\delta E_{\text{total}} = &\int_V \mathbf{m}\times\left[2\nabla\cdot\left(A\nabla\mathbf{m}\right) + \frac{\partial E_{\text{ani}}}{\partial \mathbf{m}} + \mu_0 M_{\text{s}}\mathbf{H}_{\text{a}} - \mu_0 M_{\text{s}}\mathbf{H}_{\text{d}} \right]\cdot\delta\boldsymbol{\theta}dV \\ &+ \int_S \mathbf{m}\times\left[-2A\frac{\partial \mathbf{m}}{\partial \mathbf{n}} + K_{\text{s}}\mathbf{n}\cdot\mathbf{m}\mathbf{n} \right]\cdot\delta\boldsymbol{\theta}dS\end{aligned} \tag{2.19}$$

For arbitrary $\delta\boldsymbol{\theta}$, Eq. (2.19) can be zero only if

$$\begin{aligned}&\mathbf{m}\times\left[2\nabla\cdot\left(A\nabla\mathbf{m}\right) - \frac{\partial E_{\text{ani}}}{\partial \mathbf{m}} + \mu_0 M_{\text{s}}\mathbf{H}_{\text{a}} + \mu_0 M_{\text{s}}\mathbf{H}_{\text{d}} \right] = 0 \quad \text{in } V \\ &\mathbf{m}\times\left[-2A\frac{\partial \mathbf{m}}{\partial \mathbf{n}} + K_{\text{s}}\mathbf{n}\cdot\mathbf{m}\mathbf{n} \right] = 0 \qquad\qquad\qquad \text{in } S\end{aligned} \tag{2.20}$$

From Eq. (2.20), we can define an effective field as

$$\begin{aligned}\mathbf{H}_{\text{eff}} &= \frac{2}{\mu_0 M_{\text{s}}}\nabla\cdot\left(A\nabla\mathbf{m}\right) - \frac{1}{\mu_0 M_{\text{s}}}\frac{\partial E_{\text{ani}}}{\partial \mathbf{m}} + \mathbf{H}_{\text{a}} + \mathbf{H}_{\text{d}} \\ \mathbf{H}_{\text{eff}}^{S} &= -2A\frac{\partial \mathbf{m}}{\partial \mathbf{n}} - K_S\mathbf{n}\cdot\mathbf{m}\mathbf{n}\end{aligned} \tag{2.21}$$

Rewriting Eq. (2.21), finally, we obtain Brown's equation in the form

$$\begin{aligned}&\mathbf{m}\times\mathbf{H}_{\text{eff}} = 0 \quad \text{in } V \\ &\mathbf{m}\times\mathbf{H}_{\text{eff}}^{S} = 0 \quad \text{on } S\end{aligned} \tag{2.22}$$

C. Equation of Motion of Magnetization

The dynamics of the local magnetization in ferromagnetic materials can be described by

$$\frac{d\mathbf{m}}{dt} = -\gamma \mathbf{m} \times \mathbf{H}_{\text{eff}}, \quad (2.23)$$

where γ is the gyromagnetic ratio, and $\mathbf{H}_{\text{eff}}$ is effective field arising from exchange, anisotropic, and dipolar coupling as well as the external field.

If the system reaches its equilibrium state by releasing its internal energy, the local magnetization will be collinear with the effective field direction. Then, the torque on the magnetization vanishes, as described by Eq. (2.22). This dissipative process can be taken into account by adding a dissipative to right-hand side of Eq. (2.23), as proposed Landau and Lifshitz [25]:

$$\frac{d\mathbf{M}}{dt} = -\gamma \mathbf{M} \times \mathbf{H}_{\text{eff}} - \frac{\gamma\lambda}{M_s^2} \mathbf{M} \times \left(\mathbf{M} \times \mathbf{H}_{\text{eff}} \right), \quad (2.24)$$

where λ is a dissipation parameter. There are several processes that contribute to dissipative processes in a magnetic material. These processes can have intrinsic origins, i.e. the magnon-phonon interaction, and the interaction between 3d and 4s electrons, as well as extrinsic origins. Gilbert proposed a phenomenological damping term, which combines all damping effects in a damping constant [26]. Finally, the equation of motion, called the Landau-Lifshitz Gilbert (LLG) equation, is

$$\frac{d\mathbf{M}}{dt} = -\gamma \mathbf{M} \times \mathbf{H}_{\text{eff}} - \frac{\alpha}{M_s} \mathbf{M} \times \frac{d\mathbf{M}}{dt}, \quad (2.25)$$

with a dimensionless parameter, $\alpha = \lambda / M_s$.

2.2.2. Micromagnetic Simulations

Spin dynamics in magnetic materials can be described by the Landau-Lifshitz-Gilbert (LLG) equation, introduced in Chapter 2.2.1. The LLG equation is a differential equation that describes the dynamics of individual magnetizations interacting with each other through exchange, dipole coupling, magnetocrystalline anisotropy, and the Zeeman field. In obtaining exact solutions to this equation, one confronts many technical difficulties related to the acquisition of boundary and initial conditions. Fortunately, however, an alternative solution is to use a numerical approximation, for which there are two common approaches: the finite-difference method (FDM) and the finite-element method (FEM). Both approaches lead to a set of simultaneous linear equations. In the present work, we used FEM-based Finite Element MicorMagnEtics (FEMME) [28] as simulation tools.

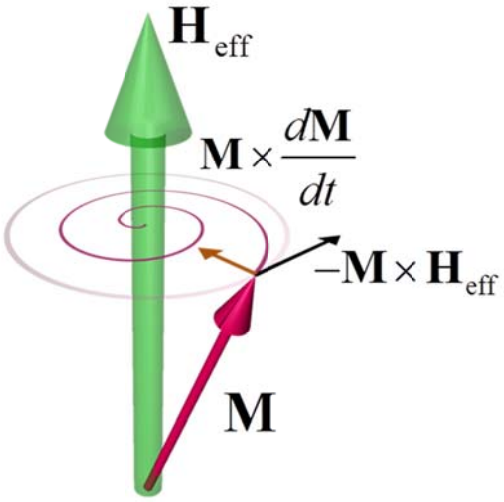

Fig. 2.5. Schematic of magnetization (**M**) precession motion with damping around the effective magnetic field ($\mathbf{H}_{\mathrm{eff}}$).

FDM		FEM
O	Stray field treatment using FFT	X
X	Arbitrary shape	O
Easy	Programming	Hard
OOMMF	Open source release	Magpar Nmag
LLG Micromagus	Commercial package	FEMME Spinflow 3D

Fig. 2.6. Comparison of advantages and disadvantages between FDM and FEM methods for the micromagnetic simulations

2.3. Vector Network Analyzer (VNA)

2.3.1. Vector Network Analyzer–Ferromagnetic Resonance Measurement

Vector network analyzer–ferromagnetic resonance (VNA-FMR) measurement is relatively new induction technique that utilizes VNA devices and high frequency circuit components. The VNA-FMR technique operates over a wide frequency band (up to several tens of gigahertz) and calculates FMR parameters as function of frequency and field in standard scattering parameter measurements. Figure 2.7 shows a diagram of the system. The microwave drive is created by a coplanar waveguide (CWG) excitation structure, after put the sample onto it. The measurements are usually performed by sweeping the desire range of the frequencies in a fixed magnetic field and by recording the signal. The magnetic field is changed and this process is repeated.

As mentioned earlier, VNA provides the scattering parameters (*S*-parameters). There are several models that evaluating the magnetic permeability or magnetic susceptibility from *S*-parameters.

2.3.2. Reflection VNA-FMR technique

One port open circuit reflection measurement has a simplified analysis model proposed by Bilzer *et al*. [29]. The measurements are simpler and faster than two-port measurements. This is because only a single reflection parameter needs to be measured and there is a simplified calibration procedure for a single port.

The one port system consists of the open circuit CWG shown in Figure 2.7. The expression for χ is a value proportional to the susceptibility for the case of ferromagnetic film [29]:

$$\chi = \frac{\ln\left(S_{11,\text{sample}}\right)}{\ln\left(S_{11,\text{reference}}\right)} - 1. \quad (2.26)$$

The FMR frequency and the line width are expressed as χ. For the two-port measurements, all mentioned evaluation methods provide resonance within 1% relative error, including open port technique. At the same time, the relative error of line width depends on the methods discribed above. The Kuanr [30] method has the highest relative error, followed by the Kalarickel method, which reaches a maximum of 10% for both methods in the low fields (i.e. corresponding to low frequencies) and decreases for high frequency cases to around 4% [31]. The open port evaluation method shows a relative error of less than 6% in the line width assessment reported by Bilzer *et al* [29].

2.3.3. Transmission VNA-FMR Technique

Recently, new evaluation method for different physical parameters obtained from VNA-FMR has been proposed and compared with existing extraction methods. A very good examples of this comparison are presented by Kalarickal *et al*. [32] and Bilzer *et al*. [31]. We provides a briefly introduce to some of these methods below.

Kuanr *et al*. [30] directly evaluated the resonance frequency and the linewidth from the amplitude of the transmitted signal, S_{21}. The contribution from the junctions and the substrate wes subtracted from the spectrum of the field where no response was

detected.

Kalarickal *et al*., presented an evaluation of the effective microwave permeability parameter that were not corrected by neglecting reflections. The uncalibrated effective microwave permeability parameter could be provided using only the transmission S_{21}-parameter of the measurements and the measurements in the reference field with parallel pumping, for which no response exists. This uncalibrated effective microwave permeability parameter could be expressed according to Kalarickal *et al*.:

$$U = \pm \frac{i \ln\left[S_{21,\text{sample}} - S_{21,\text{ref}} \right]}{\ln\left[S_{21,\text{ref}} \right]} = \pm i \left(\frac{\ln\left[S_{21,\text{sample}} \right]}{\ln\left[S_{21,\text{ref}} \right]} - 1 \right). \quad (2.27)$$

This equation simplifies additional additional offsets and resonance shape distortions. These distortions can be corrected by introducing additional fitting parameters that reported by Kalarickel *et al*. In this approach -Im(U) is the loss profile of the resonance and Re[U] is the dispersion of the resonance. The sign in the equation of U is chosen so that U is negative near the resonance peak.

Bilzer *et al*. reported another important approach to provide values that are proportional to the complex susceptibility and permittivity for the ferromagnetic sample which requires further calibration for the sample placement and dimensions.

Based on our experience with these experiments, we are trying to provide an experimental design to actually apply the energy-dissipation of nanoparticles with single-domain state. The spherical permalloy nanoparticles can be easily synthesized, as shown in the results reported previously [33]. The magnetization dynamics that occur when permalloy particles interact with each other at close distances may be different from when the particles are independent. Therefore, it is required to apply

silica coating to the particles. The synthesized nanoparticles can be contacted in solid or liquid form with an electrode specifically designed to apply AC magnetic field. From the samples, we can measure the energy dissipated accordingly in a frequency range of up to several GHz using a vector network analyzer (VNA) under DC magnetic fields. We provide a schematic illustration of such an *in-vitro* experiment in Chapter 5. After observing the physical phenomenon that energy-dissipation occurs in superparamagnetic particles with this simple experimental design, it is possible to *in vivo* experiment by changing the MRI device which applies the DC magnetic field and AC magnetic field in a wide space.

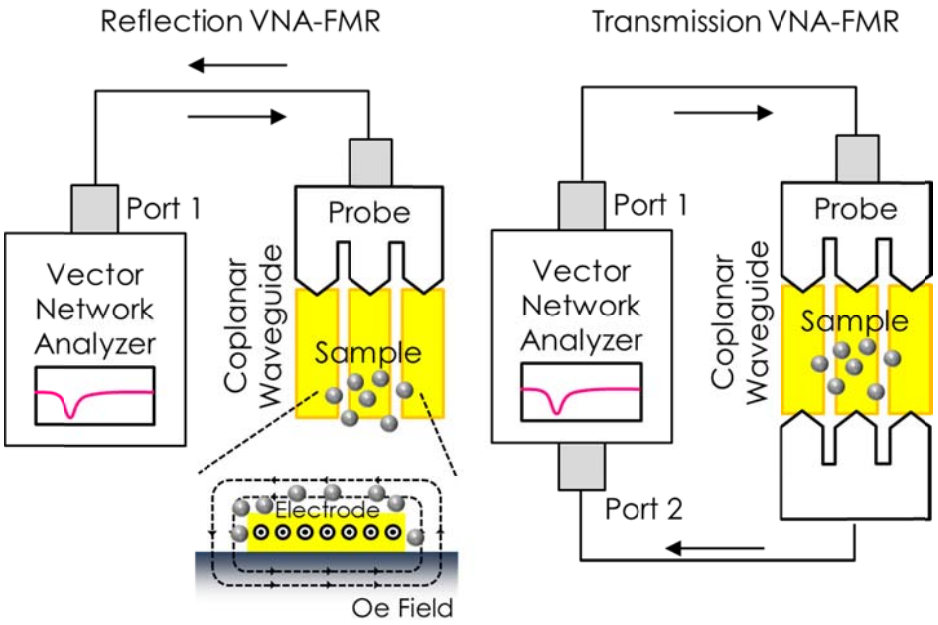

Fig. 2.7. Schematic of the VNA-FMR setup for the reflection and transmission VNA-FMR measurements.

Appendix [3]

Analytical Derivation of Vortex-core Precession in Nanoparticles

The analytical derivation of characteristic frequency of vortex-core precession is reported by S.-K. Kim et al [3]. In modeling, a weak static field was applied in the +*z*-direction, which field sustained the rigid vortex structure in a certain potential, and thus allowed the initial ground-state vortex core to align in the +*z*-direction through the precession around the field direction along with certain damping. We used the local spherical reference frame on infinitesimal segments of the surface, where the unit vector of local magnetizations is expressed as $\mathbf{m} = (m_r, m_\theta, m_\varphi)$, r is the radial distance, θ is the polar angle, and φ is the azimuthal angle, as shown in Fig. 2.8a. Time-variable vortex-core orientation can be defined as a unit vector.

$\mathbf{\Gamma} \equiv (\sin\theta_0 \cos\varphi_0, \sin\theta_0 \sin\varphi_0, \cos\theta_0)$, as illustrated in Fig. 4b. Following the rigid vortex Ansatz, which agreed with the micromagnetic simulation results, local magnetizations inside a given sphere could be expressed as $m_r = f(r, \mathbf{\Gamma}\cdot\hat{\mathbf{r}})$ and $\Phi = -\arctan\left\{(\mathbf{\Gamma}\cdot\hat{\boldsymbol{\theta}})/(\mathbf{\Gamma}\cdot\hat{\boldsymbol{\varphi}})\right\}$, where Φ is the azimuthal angle of the magnetization in the local spherical reference frame (inset of Fig. 2.8a). Here we assume some general shapes of mr that are restricted by the condition f(r,1) = − f(r,− 1) = 1 for all r values. Since m_r and Φ are canonically conjugated variables, the time evolution of the local magnetizations can be determined from the Landau-Lifshitz-Gilbert (LLG) equations as

$$\dot{\mathbf{m}}_r = -\frac{\gamma}{M_s}\frac{\delta E}{\delta \Phi} - \alpha(1-m_r{}^2)\dot{\Phi}, \quad (2.28)$$

$$\dot{\Phi} = -\frac{\gamma}{M_S}\frac{\delta E}{\delta m_r} + \frac{1}{1-m_r{}^2}\dot{m}_r. \quad (2.29)$$

By inserting the mr distribution function of the vortex's spin configuration into Eqs. (2.28) and (2.29), we finally obtained the governing equation for vortex-core precession motion,

$$\dot{\mathbf{\Gamma}} + \frac{\gamma}{M_S V}\mathbf{\Gamma}\times\frac{\partial E}{\partial \mathbf{\Gamma}} + \frac{\alpha}{V}\mathbf{\Gamma}\times\frac{\partial F}{\partial \dot{\mathbf{\Gamma}}} = 0, \quad (2.30)$$

where E is the total magnetic energy, F is a dissipative functional $\left(F = \frac{V}{2}\int d\mathbf{r}\left[\sin^2\Theta(\frac{\partial \Phi}{\partial \mathbf{\Gamma}})^2 + \left(\frac{\partial \Theta}{\partial \mathbf{\Gamma}}\cdot\dot{\mathbf{\Gamma}}\right)^2 \right] \right)$, and $V = 4\pi R^3$ is the sphere volume. The first, second and third terms in Eq. (2.30) correspond to the gyrotropic, potential energy and damping terms, respectively. The total energy E under a weak magnetic field applied along the z-axis, can be expressed simply as $E_H = -\hat{\mathbf{z}}\cdot\mathbf{\Gamma}(t)H_{DC}VM_S\langle m_{\mathbf{\Gamma}}\rangle$, where $\langle m_{\mathbf{\Gamma}}\rangle$ is rewritten as $\langle m_{\mathbf{\Gamma}}\rangle = \frac{1}{M_S V}\int d\mathbf{r}(\mathbf{M}\cdot\mathbf{\Gamma})$. Eq. (2.30) expresses the precession motion of vortex cores in collective spin dynamics; it differs from Thiele's equation to describe the gyration of vortex cores in planar dot systems.

By inserting E_H into Eq. (2.30) and assuming negligible damping, the precession frequency of a rigid vortex core can be given as $\partial\phi_0/\partial t = 2\pi f_{MV}$ with $f_{MV} = (\gamma/2\pi)\langle m_{\mathbf{\Gamma}}\rangle H_{DC}$. Consequently, we obtained the effective gyromagnetic ratio of the motion of a vortex in a given nanosphere as $\gamma_{eff} = \gamma\langle m_{\mathbf{\Gamma}}\rangle$. This analytic form provides a clear physical insight into $2R$-dependent f_{MV}, because $\langle m_{\mathbf{\Gamma}}\rangle$, as indicated in the

micromagnetic simulation results, varies with 2*R*.

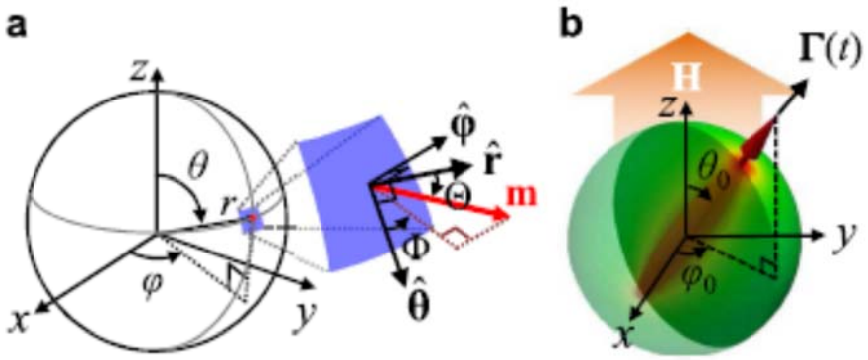

Fig. 2.8. Model for analytical derivation. (a) Definition of spherical coordinates and local spherical reference frame (colored surface) for local magnetization **m**. (b) Schematic of model sphere wherein single rigid vortex core is pointed in direction in direction of θ_0 and φ_0, as defined by the polar and azimuthal angle coordinates. [3]

2.5. References

[1] L. Néel, Ann. Géophys. **5**, 99 (1949).

[2] W. F. Brown Jr, Phys. Rev. **130**, 1677 (1963).

[3] S.-K. Kim, M.-W. Yoo, J.-H. Lee, Y. Gaididei, V. P. Kravchuk, and D. D. Sheka, Sci. Rep. **5**, 11370 (2015).

[4] http://en.wikipedia.org/wiki/Superparamagentism.

[5] Q. A. Pankhurst, J. Connolly, S. K. Jones, and J-. Dobson, J. Phys. D: Appl. Phys. **36**, R167 (2003)..

[6] T. Neuberger, B. Sch Schöpf, H. Hofmann, M. Hofmann, and B. von Rechenberg, J. Magn. Magn. Mater. **293**, 483 (2005).

[7] U. Jeong, X. Teng, Y. Wang, H. Yang, and Y. Xia, Adv. Mater. **19**, 33 (2007).

[8] G. Kandasamy, and D. Maity, Int. J. Pharm. **496**, 191 (2015).

[9] http://en.wikipedia.org/wiki/Single-domain_(magnetic).

[10] L. -M. Lacroix, S. Lachaize, F. Hue, C. Gatel, T. Blon, R. P. Tan, J. Carrey, B. Warot-Fonrose, and B. Chaudret, Nano Lett. **12**, 6 (2012).

[11]. S.-K. Kim, M.-W. Yoo, J. Lee, J.-H. Lee, and M.-K. Kim, Sci. Rep. **6**, 31513 (2016).

[12] http://en.wikipedia.org/wiki/Larmor_precession.

[13] R. C. O'Handley, Modern Magnetic Materials: Principles and Aplications. (Wiley, 1999).

[14] B. Hillebrands, and A. Thiaville, Spin Dynamics in Confined Magnetic Structures 3. (Springer, 2006).

[15] K, S. Lee, K. Y. Guslienko, J. Y. Lee, and S. K. Kim, Phys. Rev. B **76**, 174410 (2007).

[16] J. M. D. Coey, Magnetism and Magnetic Materials. (Cambridge University Press, 2010).

[17] M. Kammerer *et al*, Nat. Commun. **2**, 279 (2011).

[18] M. W. Yoo, and S. K. Kim, Appl. Phys, Lett. **100**, 172413 (2012).

[19] A. Trabesinger, Nature **435**, 1173 (2005).

[20] A. G. Webb, Introduction to biomedical Imaging. (Wiley-IEEE. Press, 2002).

[21] J. Ding, G. N. Kakazei, X. M. Liu, K. Y. Guslienko, and A. O. Adeyeye, Sci. Rep. **4**, 4796 (2014).

[22] S. Mornet, S. Vasseur, F. Grasset, and E. Duguet, J. Mater. Chem. **14**, 2161 (2004).

[23] S. Chikazumi, Physics of magnetizm (John Wiley & Sons, Inc., New York, 1964).

[24] G. T. Rado and J. R. Weertman, Journal of Physics and Chemistry of Solids **11**, 315 (1959).

[25] L. D. Landau and E. M. Lifshitz, Phys. Z. Sowjetunion **8**, 153 (1935).

[26] T. L. Gilbert, Ieee T Magn **40**, 3443 (2004).

[27] See http://math.nist.gov/oommf.

[28] D. Suess, and T. Schrefl, FEMME: Finite Element MicroMagnEtics 5.0.8 (SuessCo, http://suessco.com/).

[29] C. Bilzer, T. Devolder, P. Crozat and C. Chappert, Ieee. T. Magn. **44**, 3265 (2008).

[30] B. K. Kuanr, R. E. Camley and Z. Celinski, J. Magn. Magn. Mater. **286**, 276 (2005).

[31] C. Bilzer, T. Devolder, P. Crozat, C. Chappert, S. Cardoso and P. P. Freitas, J. Appl. Phys. **101**, 074505 (2007).

[32] S. S. Kalarickal, P. Krivosik, M. Z. Wu, C. E. Patton, M. L. Schneider, P. Kabos, T. J. Silva and J. P. Nibarger, J. Appl. Phys. **99**, 093909 (2006).

[33] M.-K. Kim et al., Appl. Phys. Lett., **105**, 232402 (2013).

Chapter 3

Dynamic Origin of Highly Efficient Energy-dissipation in Soft Magnetic Nanoparticles in Single-domain State

3.1. Introduction

Magnetic nanoparticles are of increasing interest due to their unique physical properties such as superparamagnetism [1,2], macroscopic quantum tunneling of magnetizations [3,4], exchange-bias effect [5], and particle-size-dependent static and dynamic properties. These novel characteristics of magnetic nanoparticles make them very attractive for a rich variety of applications such as high-density data storage [6,7], spintronic devices [8-10], and bio-applications including magnetic hyperthermia and MRI contrast agents [11-14]. As an example, the magnetization dynamics of nanoparticles with vortex spin spirals exhibit unique dynamic modes such as resonant

vortex-core precession motion [15] and reversals [16]. Also, soft magnetic nanoparticles in single-domain states exhibit collective Larmor precession of individual spins. In cases where the frequency of time-varying magnetic fields equals the Larmor precession frequency, individual magnetic moments efficiently absorb energies that are transferred from externally applied AC magnetic fields, after which those energies dissipate into other forms due to their intrinsic damping of given materials. Such energy dissipations of magnetic nanoparticles are of crucial importance in low-power-consumption magnetization switching in magnetic memory devices, and also in hyperthermia bio-applications for high specific loss power (SLP) [11,12,17]. Externally applied magnetic fields of several hundred kHz range can be absorbed into/by magnetic nanoparticles and then dissipated via either Brownian rotation of the nanoparticles and/or Néel relaxation [1] of the magnetizations inside them [18,19]. It has been reported that the SLP for the aforementioned mechanisms ranges between 0.5 and 2 kW/g. Contrastingly, Larmor precession motions of individual spins in magnetic particles excited by relatively high-frequency (several hundred MHz) AC magnetic fields can give rise to high-efficiency energy dissipation into a different form of energy (e.g., heat). Thus, their mechanism-related SLP would be higher than those of other mechanisms.

In the present study, we explored robust non-linear magnetization dynamics and the associated high-efficiency energy-dissipation effect in soft magnetic nanospheres in single-domain states, as excited by oscillating magnetic fields of different frequencies and amplitudes under given static magnetic fields. We conducted micromagnetic simulations to explore the novel magnetization dynamics of soft magnetic particles and

additional analytical derivations of the energy-dissipation rate for the steady-state regime by varying the frequency and strength of rotating magnetic fields for different Gilbert damping constants and static magnetic field strengths. All of the simulation results and analytical calculations agree well quantitatively. The dynamic origin of such a high-efficiency energy-dissipation mechanism is completely different from those of the typical ones used in bio-applications. We expect that this efficient, very high energy-dissipation rate will prove implementable in magnetic hyperthermia applications.

3.2. Modeling

In the present study, we conducted finite-element micromagnetic simulations of soft magnetic Permalloy (Py, $Ni_{80}Fe_{20}$) nanospheres in single-domain states, the diameters of which were set to $2R$ = 10, 20, and 30 nm. To numerically solve dynamic motions of magnetizations (**M**), we used the FEMME code (version 5.0.9) [20] that utilizes the Landau-Lifshitz-Gilbert (LLG) equation

$$\frac{d\mathbf{M}}{dt} = -\gamma\left[\mathbf{M}\times\mathbf{H}_{\text{eff}}\right] + \frac{\alpha}{M_{\text{s}}}\left[\mathbf{M}\times\frac{d\mathbf{M}}{dt}\right], \qquad (3.1)$$

where $\mathbf{H}_{\text{eff}}$ is the effective field, M_{s} is the saturation magnetization value, α is the dimensionless Gilbert damping constant, and γ is the gyromagnetic ratio. The effective field is, $\mathbf{H}_{\text{eff}} = -\delta\varepsilon / \delta\mathbf{M}$, is the negative variational derivative of the total energy density, ε, including the exchange, the magnetostatic, the magnetocrystalline anisotropy, and Zeeman energies. The magnetic parameters corresponding to the Py

material were as follows: saturation magnetization M_s = 860 emu/cm^3, exchange stiffness A = 1.3 × 10^{-6} erg/cm, gyromagnetic ratio $\gamma = 2\pi \times 2.8$ $\mathrm{rad \cdot MHz/Oe}$, and zero magneto-crystalline anisotropy. To avoid errors inherent to representation of a spherical geometry with a set of cubic cells, we opted for triangular tessellation using Hierachial Triangular Mesh [21], and the inner volume into tetrahedron elements (mesh size ≤ 3 nm) (see Fig. 3.1(a)).

Through relaxation from initially saturated magnetizations oriented in the +*z*-direction for the Py nanospheres, we obtained uniformly magnetized single-domain ground states for each diameter 2*R* = 10, 20, and 30 nm (see Fig. 3.1(b)). For the Py spheres, the single-domain states were maintained up to 2*R* = ~ 35 nm, which states are the results of competition between strong short-range exchange and weak long-range interactions along with such nano-scale geometrical confinements. Because the spheres are magnetically isotropic insofar as there is no other sources of anisotropy, uniform magnetizations can reorient to the direction of applied static magnetic fields. It is well known that such single-domain magnetic particles exhibit collective Larmor precession motions of individual spins around the axis of a static magnetic field with following characteristic frequency: It is well known that the so-called Ferromagnetic Resonance (FMR) occurs in such a single-domain magnetic particle as a collective laminar leading motion of individual spins around the static magnetic field axis. In a given isotropic system, the resonance frequency of the system is given by

$$f_{\mathrm{L}} = (\gamma / 2\pi) H_{\mathrm{DC}} \qquad (3.2)$$

where H_{DC} is the static field strength.

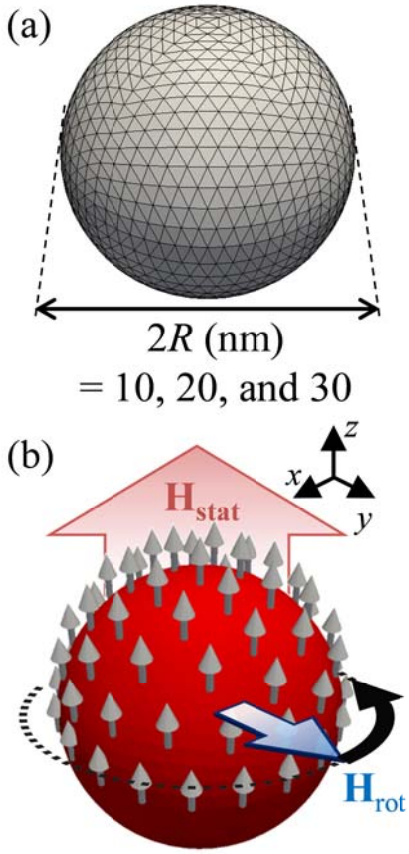

Fig. 3.1. (a) Finite-element sphere model of diameter $2R$ = 10 – 20 nm. (b) Single-domain sphere model of diameter $2R$ = 20 nm under circular-rotating field and static field.

3.3. Results and Discussion

3.3.1. Characteristic Dynamic Motions of Magnetization

To investigate the characteristic dynamic motions of the uniformly oriented magnetizations of the Py spheres, we applied a static field $\mathbf{H}_{\text{stat}} = H_{\text{DC}}\hat{\mathbf{z}}$ in the +z-direction, which allows for the reorientation of the magnetizations in the +z-direction. Since the Larmor precession motion of magnetizations is counter-clockwise (CCW) in its rotation sense, we chose the CCW basis of circular-rotating magnetic fields on the x-y plane, as described by $\mathbf{H}_{\text{rot}} = H_{\text{AC}}\cos\left(2\pi f_{\text{CCW}}t\right)\hat{\mathbf{x}} + H_{\text{AC}}\sin\left(2\pi f_{\text{CCW}}t\right)\hat{\mathbf{y}}$ with the field strength H_{AC} and the field frequency f_{CCW} (see Fig. 3.2(b)). For $2R$ = 20 nm under H_{DC} = 100 Oe, Fig. 3.2 shows the characteristic precession motions' unit vector $\mathbf{m} = \mathbf{M}/M_{\text{s}}$ of the uniform magnetizations excited by two different frequencies, f_{CCW} = 200 and 280 MHz, each of H_{AC} = 4, 5, and 6 Oe. Since the Larmor frequency for the Py sphere of $2R$ = 20 nm under H_{DC} = +100 Oe is equal to f_{L} = 280 MHz in accordance to Eq. (3.2), the application of f_{CCW} = 200 MHz would lead to non-resonant excitations, whereas the application of f_{CCW} = 280 MHz, resonant excitations. At non-resonance excitations (see Fig. 3.2(a)) the in-plane m_x and m_y components are small, while m_z is almost close to unity, indicating that the precession motions of the magnetizations occur while keeping **m** in the +z-direction. On the other hand, at resonance excitations (see Fig. 3.2(b)), the precession motions occur with relatively large in-plane **m** components, even for the very small field strengths H_{AC} = 4, 5, and 6

Oe. All of the dynamic motions for the individual cases finally reach their corresponding steady states with specific m_z values according to the given H_{AC} value. All of the m_z values in the steady states also decrease with increasing H_{AC} until $H_{AC} = 5$ Oe. Beyond the field magnitude $H_{AC} = 5$ Oe, the m_z becomes zero, indicating that all of the final steady states are in the precession motion of **m** on the *x*-*y* plane, i.e., the equator of the sphere. On the other hand, at $H_{AC} = 6$ Oe, for example, the **m** periodically oscillates (switches) between the +*z* and –*z*-directions before converging to the precession motion exactly on the equator, i.e., keeping $m_z = 0$. It was interesting to further examine the frequency of the **m** switching with varying H_{AC}, as shown in Fig. 3.2(c). As evident from the simulation results (symbols), the periodic switching of **m** starts when H_{AC} reaches αH_{DC} for given values of H_{DC} and α. The existence of such a threshold field strength $H_{AC}^{th} = \alpha H_{DC}$ will be explained, immediately below, according to the steady-state torque balance. For the cases of $H_{AC} \gg \alpha H_{DC}$, the novel dynamics are characterized by the fact that the reversal frequency f_{rev} is proportional to H_{AC}, as expressed by $f_{rev} = \gamma H_{AC}$ (indicated by the red solid line).

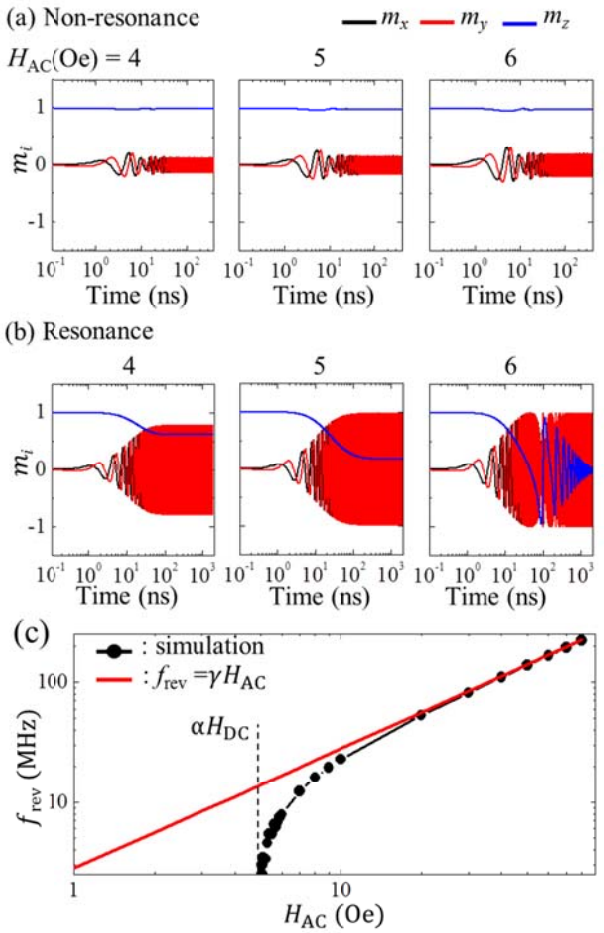

Fig. 3.2. Temporal evolution of *x*-, *y*-, and *z*-components of m for different strengths of circular-rotating fields H_{AC} = 4, 5, and 6 for (a) non-resonant case (f_{CCW}= 200 MHz) and (b) resonant case (f_{CCW} = 280 MHz). (c) f_{rev} obtained by FFT of simulation results of m_z as function of H_{AC}. The symbols with the black solid line denote the micromagnetic simulation results, while the red solid lines correspond to $f_{rev} = (\gamma / 2\pi) H_{AC}$. The static field strength H_{DC} = 100 Oe and damping constant α = 0.05 were used for all of the simulations shown in this figure.

A. Torque Balance Interpretation

In order to understand the distinct dynamic motions occurring for different H_{AC} values, even when varying in steps of 1 Oe, we took into account the magnetic torque balance. As shown in Fig. 3.3(a), the static field $\mathbf{H}_{stat}$ acting on $\mathbf{m}$ leads to the static field torque $\boldsymbol{\tau}_{stat}$ that causes precession of magnetizations around the static field. The rotating field $\mathbf{H}_{rot}$ results in the torque $\boldsymbol{\tau}_{rot}$ that determines the direction of $\mathbf{m}$ with respect to the static field direction in balance with the intrinsic damping torque $\boldsymbol{\tau}_{damp}$ (see Fig. 3.3(a)). The torque balance equation can be derived from the LLG equation as

$$\begin{aligned} \boldsymbol{\tau}_{stat} &= -\mathbf{m}\times\mathbf{H}_{stat}, \\ \boldsymbol{\tau}_{rot} &= -\mathbf{m}\times\mathbf{H}_{rot}, \\ \boldsymbol{\tau}_{damp} &= \frac{\alpha}{\gamma}\mathbf{m}\times\frac{d\mathbf{m}}{dt}. \end{aligned} \qquad (3.3)$$

Here, we considered only the external magnetic fields for $\mathbf{H}_{eff}$, because for the spherical symmetry of nanospheres and their single-domain states, neither the exchange field nor the demagnetization field varies with the orientation of $\mathbf{m}$. The torque term $\boldsymbol{\tau}_{stat}$ has no effect in determining the z-component torque balance, because it is always on the *x*-*y* plane; consequently, its *z*-component is absent. Therefore, the *z*-component torque balance in the steady state always holds for the condition $\overline{\tau}_{rot,z} + \overline{\tau}_{damp,z} = 0$. Hereafter, the "bar" on symbols indicates its steady state. According to Eq. (3.3) and the temporal magnetization variation obtained in the simulations, we calculated (see Fig. 3.3(b)) the *x*-, *y*-, and *z*-components of $\boldsymbol{\tau}_{rot}$ and

$\boldsymbol{\tau}_{\text{damp}}$ as a function of time for different values of H_{AC} = 4, 5, and 6 Oe for the given values of $2R$ = 20 nm, H_{DC} = 100 Oe, and α = 0.05 and the resonance excitation f_{CCW} = f_{L} = 280 MHz, under the same conditions as shown in Fig. 3.2(b). Hereafter, we focus on only the z-component torques, because they determine the m_z values in the steady states during their precession motions. The $|\boldsymbol{\tau}_{\text{rot},z}|$ value for H_{AC} = 4 and 5 Oe continuously increases with time and then reaches its steady-state value $|\overline{\boldsymbol{\tau}}_{\text{rot},z}|$. However, as for H_{AC}= 6, $|\boldsymbol{\tau}_{\text{rot},z}|$ gradually increases and reaches its maximum value, then starts to oscillate with its large amplitude. This large oscillation of $\boldsymbol{\tau}_{\text{rot},z}$ finally converges to its steady-state value, $\overline{\boldsymbol{\tau}}_{\text{rot},z}$. Also, $\boldsymbol{\tau}_{\text{damp},z}$ shows similar behaviors as $\boldsymbol{\tau}_{\text{rot},z}$ does, but the signs are opposite. In the case of magnetization dynamics corresponding to a steady state, it is expected that $\overline{\boldsymbol{\tau}}_{\text{rot},z}$ and $-\overline{\boldsymbol{\tau}}_{\text{damp},z}$ should balance each other. Since $|\overline{\boldsymbol{\tau}}_{\text{rot},z}|$ and $|\overline{\boldsymbol{\tau}}_{\text{damp},z}|$ vary with H_{AC}, it is worthwhile to plot their relation as in Fig. 3.3(d). $|\overline{\boldsymbol{\tau}}_{\text{rot,z}}|$ increases with H_{AC} until H_{AC} approaches the value of αH_{DC}, and then reaches its saturation value even with further increase above the specific field strength $H_{\text{AC}}^{\text{th}} = \alpha H_{\text{DC}}$. This threshold field strength is already shown in the relation of f_{rev} versus H_{AC} (see Fig. 3.2(c)). On the basis of the steady-state torque balance, we obtained the angles $\overline{\theta}$ and $\overline{\phi}$ defined in Fig. 3.3(a) as a function of H_{AC}. In the cases of $H_{\text{AC}} \geq \alpha H_{\text{DC}}$, $\overline{\theta}$ always is maintained at 90°, indicating the

processional motion of **m** on the *x*-*y* plane (equator). For $H_{AC} < \alpha H_{DC}$, **m** and the rotating field vector are not co-planar with respect to the plane of **m** and the static field as shown in Fig. 3.3(a): rather, as H_{AC} is much larger than the threshold field strength $H_{AC}^{th} = \alpha H_{DC}$, **m** rotates coherently with $\mathbf{H}_{rot}$ on the *x*-*y* plane.

B. Analytical Derivation of Magnetization Dynamics

To understand the underlying physics of the magnetization dynamics and associated torque behaviors obtained from the micromagnetic simulations, we additionally derived analytical forms from the LLG equation. By multiplying **m** on both sides of Eq. (3.1), we obtained

$$\frac{d\mathbf{m}}{dt} = -\gamma'\left[\mathbf{m}\times\mathbf{H}_{ext}\right] + \gamma'\alpha\left[\left[\mathbf{m}\times\mathbf{H}_{ext}\right]\times\mathbf{m}\right], \quad (3.4)$$

with $\gamma' = \gamma/\left(1+\alpha^2\right)$, where $\mathbf{H}_{ext}$ is composed of the rotating field on the *x*-*y* plane and the static field applied in the +*z*-direction. Since the **m** vector precesses about the *z*-axis, it is convenient to transform the time-varying **m** vector into its time-independent counterpart **u** vector on the same rotating frame on the *x*-*y* plane, as $\mathbf{u} = \mathbb{N}\mathbf{m}$, with the following transformation matrix [22-25]:

$$\mathbb{N} = \begin{pmatrix} \cos(\omega_{CCW}t) & \sin(\omega_{CCW}t) & 0 \\ -\sin(\omega_{CCW}t) & \cos(\omega_{CCW}t) & 0 \\ 0 & 0 & 1 \end{pmatrix}, \quad (3.5)$$

By inserting the relation of $\mathbf{u} = \mathbb{N}\mathbf{m}$ into Eq. (3.4), the *x*-, *y*-, *z*-components of the **u** vector are solved as

$$u_x = \frac{1-u_z^{\,2}}{\gamma H_{\mathrm{AC}} u_z}\left(\omega_{\mathrm{L}} - \omega_{\mathrm{CCW}}\right), \qquad u_y = -\frac{\alpha\omega_{\mathrm{CCW}}}{\gamma H_{\mathrm{AC}}}\left(1-u_z^{\,2}\right), \tag{3.6}$$

with $\omega_{\mathrm{CCW}} = 2\pi f_{\mathrm{CCW}}$, $\omega_{\mathrm{L}} = 2\pi f_{\mathrm{L}} = \gamma H_{\mathrm{DC}}$.

With $u_x^2 + u_y^2 + u_z^2 = 1$, they lead to the relation

$$\left(\gamma H_{\mathrm{AC}}\right)^2 = \frac{\left(1-u_z^{\,2}\right)}{u_z^{\,2}}\left[\left(\omega_{\mathrm{L}} - \omega_{\mathrm{CCW}}\right)^2 + \left(\alpha\omega_{\mathrm{CCW}} u_z\right)^2\right]. \tag{3.7}$$

Then, finally, it becomes

$$u_z^2 = \frac{-\left[\gamma^2 H_{\mathrm{AC}}^{\,2} - \alpha^2\omega_{\mathrm{CCW}}^{\,2} + \left(\omega_{\mathrm{L}} - \omega_{\mathrm{CCW}}\right)^2\right] + \sqrt{\left[\gamma^2 H_{\mathrm{AC}}^{\,2} - \alpha^2\omega_{\mathrm{CCW}}^{\,2} + \left(\omega_{\mathrm{L}} - \omega_{\mathrm{CCW}}\right)^2\right]^2 + \left[2\alpha\omega_{\mathrm{CCW}}\left(\omega_{\mathrm{L}} - \omega_{\mathrm{CCW}}\right)\right]^2}}{2\alpha^2\omega_{\mathrm{CCW}}^{\,2}}. \tag{3.8}$$

Under the resonance condition of $f_{\mathrm{CCW}} = f_{\mathrm{L}}$, it simply is given as the two different ranges of H_{AC}

$$u_z^{\,2} = 1 - \left(\frac{H_{\mathrm{AC}}}{\alpha H_{DC}}\right)^2, \quad H_{\mathrm{AC}} < \alpha H_{\mathrm{DC}} \tag{3.9a}$$

$$u_z^{\,2} = 0, \quad H_{\mathrm{AC}} \geq \alpha H_{\mathrm{DC}}. \tag{3.9b}$$

Through the relation $\mathbf{u} = \mathbb{N}\mathbf{m}$, we obtained $\overline{m}_x$, $\overline{m}_y$, and $\overline{m}_z$ again as

$$\begin{aligned} \overline{m}_x &= u_x \cos(\omega_{\mathrm{CCW}} t) - u_y \sin(\omega_{\mathrm{CCW}} t), \\ \overline{m}_y &= u_x \sin(\omega_{\mathrm{CCW}} t) + u_y \cos(\omega_{\mathrm{CCW}} t), \\ \overline{m}_z &= u_z. \end{aligned} \tag{3.10}$$

Accordingly, the z-components of the toque terms in the steady state at resonance are represented by $\overline{\boldsymbol{\tau}}_{\mathrm{rot},z} = -H_{\mathrm{AC}} \sin(\overline{\theta}) \sin(\overline{\phi})$ and $\overline{\boldsymbol{\tau}}_{\mathrm{damp},z} = \alpha H_{\mathrm{DC}} \sin^2(\overline{\theta})$ with

$\overline{\theta} = \arccos(u_z)$ and $\overline{\phi} = \arccos(u_x / \sin(\overline{\theta}))$ comment. The analytical calculations of the torques are in excellent agreement with the micromagnetic simulation results (symbols), as shown in Fig. 3.3(e). We also plotted the steady-state angles of $\overline{\theta}$ and $\overline{\phi}$ as a function of H_{AC}, as shown in Fig. 3.3(e). In the range of $H_{AC} < \alpha H_{DC}$, $\overline{\theta}$ increases with H_{AC} up to 90°. We note that $\overline{\theta} = 90°$ corresponds to the precession of uniform magnetizations on the *x*-*y* plane (equator) with $m_z = 0$. The above analytical forms (solid lines) inform us of how the steady-state torques change with H_{AC} and why the torque has its maximum value of αH_{DC}, which is independent of H_{AC} above the threshold field strength $H_{AC} = \alpha H_{DC}$. In the case of $H_{AC} < H_{AC}^{th} = \alpha H_{DC}$, $\overline{\phi}$ is almost 90°, and thus $\overline{\theta}$ is given by $\overline{\theta} = \arcsin(H_{AC} / \alpha H_{DC})$, as indicated by the black solid line shown in Fig. 3.3(e). For the cases of $H_{AC} \geq \alpha H_{DC}$, the torque balance leads to $\overline{\theta}$ = 90° and consequently to $\overline{\phi} = \arcsin(\alpha H_{DC} / H_{AC})$. This means that for the cases of $H_{AC} / H_{AC}^{th} >> 1$, **m** rotates coherently with the rotating field on the *x*-*y* plane. The torque balance equations well explain the steady-state dynamics observed in the present study.

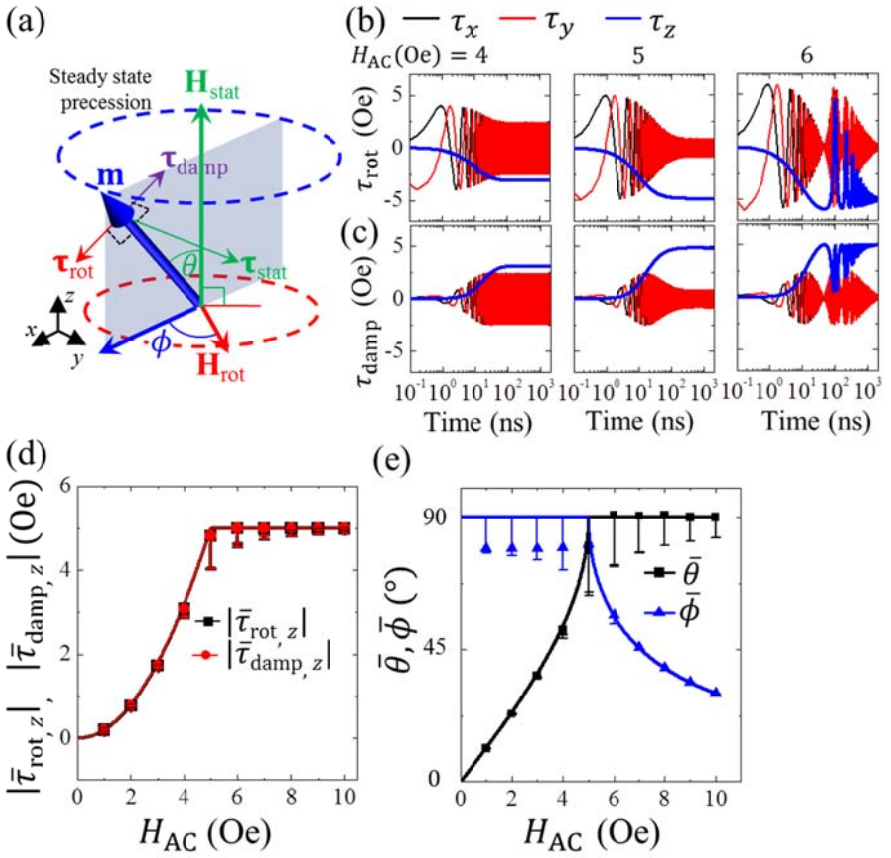

Fig. 3.3. (a) Schematic illustration of dynamic relationship between macrospin (uniform magnetization) and external static field and time-varying circular-rotating field. $\mathbf{H}_{rot}$ is always on the plane perpendicular to the static field direction. Three torque terms $\boldsymbol{\tau}_{stat}$, $\boldsymbol{\tau}_{rot}$, and $\boldsymbol{\tau}_{damp}$ are displayed acting on **m** with θ, which are the angles between **m** with $\mathbf{H}_{stat}$,. The angle that shows the phase delay of **m** from $\mathbf{H}_{rot}$, ϕ, also is displayed. Temporal evolution of x (black), y (red), and z (blue) -components of (b) $\boldsymbol{\tau}_{rot}$ (c) $\boldsymbol{\tau}_{damp}$ for different strengths of circular-rotating fields H_{AC} = 4, 5, and 6 in resonant case (f_{CCW} = 280 MHz). (d) Steady-state values of z-components of $|\boldsymbol{\tau}_{rot}|$ and ‖

$|\boldsymbol{\tau}_{\text{damp}}|$ as function of H_{AC}. (e) Steady-state values of θ, ϕ as functions of H_{AC}. The symbols denote the micromagnetic simulation results, while the solid lines correspond to the analytical calculation data. The static field strength H_{DC} = 100 Oe and damping constant α = 0.05 were used for all of the simulations shown in this figure. The error bars of the simulation values of the torques and angles are plotted for possible $\pm$ 1 % errors that could occur in the micromagnetic simulation.

3.3.2. Energy-dissipation Rate of Single-domain State

Above, we explored both the non-resonant and resonant dynamic motions of the magnetizations of Py nanospheres in single-domain states. The robust dynamics of soft magnetic nanoparticles in nonlinear dynamic regimes can be implemented in magnetic hyperthermia applications. In the research field of magnetic hyperthermia, SLP in the form of Watts/gram (W/g) is widely used to represent heat (or temperature increase) from magnetic particles. On the basis of energy conservation and fundamental Maxwell equations, the power loss can be represented by the magnetic energy-dissipation rate, and can be expressed as [26]

$$Q = -\frac{1}{\rho V}\int_V \left(d\varepsilon_{\mathrm{G}} / dt + \mathbf{M}(t) \cdot d\mathbf{H}_{\mathrm{ext}}(t) / dt \right) dV, \qquad (3.11)$$

where ε_{G} is the Gibbs' energy density with the volume of nanosphere V and the density of permalloy $\rho = 8.72$ g/cm^3. The first and second terms on the right side are the time derivative of magnetic energy and the dual power of external force, respectively (for details, see Ref [26]). In the current research on magnetic hyperthermia, oscillating magnetic fields of a few hundred kHz are typically applied; therefore, the SLP, as a measurable quantity, is redefined to Q averaged over a time period T_0,

$$\langle Q \rangle = -\frac{1}{\rho V T_0}\int_0^{T_0}\oint_V (d\varepsilon_{\mathrm{G}} / dt + \mathbf{M}(t) \cdot d\mathbf{H}_{\mathrm{ext}}(t) / dt) dV dt. \qquad (3.12)$$

Accordingly, from our micromagnetic simulation data, we can directly obtain the quantities of Q and $\langle Q \rangle$ versus a given time for the nonlinear dynamic motions of a single-domain nanosphere of $2R$ = 20 nm for the specific cases of H_{DC} = 100 Oe and

α = 0.05, as excited by two different frequencies, f_{CCW} = 200 (off-resonance) and 280 MHz (resonance) for each of the different values of H_{AC} = 4, 5, and 6 Oe. Whether at resonance or off-resonance, the two different quantities of Q and $\langle Q \rangle$ displayed somewhat distinct behaviors for most of the time, except for their steady states, as shown in Fig. 3.4. For example, in the case of off-resonance, there were large differences between Q and $\langle Q \rangle$, whereas those values became almost equal above t = 100 ns. In the case of resonance, the steady-state wherein both values become equal was achieved after a rather longer time, above 1500 ns. The reason for the equal values of Q and $\langle Q \rangle$ in the steady states is the fact that the $\partial \varepsilon_G / \partial t$ term in both Q and $\langle Q \rangle$ becomes zero, so that Q and $\langle Q \rangle$ are the same. Although the $\langle Q \rangle$ quantity typically represents the measurable SLP, in this study we used the quantity of Q, because it can be calculated analytically for comparison with the corresponding simulation.

Related to the above issue regarding SLP, from now on, we focus only on Q values that can be numerically calculated from the micromagnetic simulation data shown in Fig. 3.4 using Eq. (3.11), and (3.3) can be analytically derived, as shown later. Figure 3.5 compares the individual Q values as well as the negative derivative of energy density $-\frac{1}{\rho V}\int_{\Omega}\left(d\varepsilon_G / dt\right)dV$ and negative dual power density $-\frac{1}{\rho V}\int_{\Omega}\left(d\mathbf{H}_{ext} / dt \cdot \mathbf{M}\right)dV$ calculated from the simulation results for the non-resonant (f_{CCW} = 200 MHz) and resonant ($f_{CCW} = f_L$ = 280 MHz) conditions. At non-resonance, those values largely fluctuate up to 10 ns, after which they reach their steady-state regime. These large oscillations are associated with the initial large perturbations of magnetizations, as shown in Fig. 3.2(a). On the contrary, at resonance,

the values of Q and the $-\frac{1}{\rho V}\int_{\Omega}\left(d\mathbf{H}_{\text{ext}}/dt\cdot\mathbf{M}\right)dV$ slowly increase and then converge to certain corresponding values, due to the fact that their dynamic motions reach their corresponding steady states. For all of the cases, the $-\frac{1}{\rho V}\int_{\Omega}\left(d\varepsilon_{\text{G}}/dt\right)dV$ (black line) converges to zero in the steady states, but the $-\frac{1}{\rho V}\int_{\Omega}\left(d\mathbf{H}_{\text{ext}}/dt\cdot\mathbf{M}\right)dV$ (red color) becomes equal to Q; hereafter, the Q quantity in the steady state is noted as $\overline{Q}$. Therefore, $\overline{Q}$ is determined only by the dual power density. $\overline{Q}$ for the non-resonant and resonant cases contrast starkly. For the non-resonant condition, those energy powers relatively quickly converge to zero or low values after large initial fluctuations. As the H_{AC} increases, the initial oscillations and steady-state values increase. By contrast, at resonance, the initial oscillations disappear, but the time derivatives of energy density and dual power density converge to certain values after a longer time (as late as 1000 ns). Also, using an H_{AC} value larger than 5 Oe, for example 6 Oe, those energy powers oscillate with large fluctuations before reaching the steady state, which oscillations are related to magnetization switching between the $+z$ and $-z$- directions, as already shown in Fig. 3.2.

The quantities of $\overline{Q}$ at resonance are much higher than those at non-resonance. In order to compare $\overline{Q}$ as a function of f_{CCW}, we conducted micromagnetic simulations by varying f_{CCW} within the 20 – 540 MHz range; then, from the simulation results, we numerically calculated $\overline{Q}$ versus f_{CCW}. As shown in Fig. 6, under the application of H_{DC} = 100 Oe, H_{AC} = 5 Oe, we plotted $\overline{Q}$ values versus f_{CCW} for the different values

of α = 0.01, 0.03, 0.05 and 0.07 and for Py nanospheres of $2R$ =10, 20, and 30 nm in single-domain states. As is apparent, there were clear peaks when f_{CCW} reached f_L (=280 MHz), independent of α. These results indicate that the energy forms of the applied magnetic fields are transferred highly efficiently to nanoparticles and then subsequently dissipated via nonlinear magnetization dynamics due to intrinsic damping.

Such a high quantity of $\overline{Q}$ at resonance is important in terms of efficient energy transfer of external magnetic field energy to a magnetic sphere and subsequent release into other energy forms such as heat via dynamic magnetization dissipation. Also, since magnetic particles can be applicable to hyperthermia bio-applications, it was worth examining, for resonance cases, $\overline{Q}$ versus H_{AC} for different H_{DC} fields and values of α. From further micromagnetic simulations, we obtained $\overline{Q}$ at resonance (hereafter noted as $\overline{Q}_{RES}$) versus H_{AC} for the three virtual cases of α = 0.03, 0.05 and 0.07 and for the different values of H_{DC} = 50, 100, 150 Oe. For the given values of α, $\overline{Q}_{RES}$ increases with H_{AC} up to a certain value of H_{AC} (noted as H_{AC}^{th}), thereafter becoming saturated even with the further increase of H_{AC} beyond H_{AC}^{th}. Quite interestingly, H_{AC}^{th} varies with H_{DC} and α. Also, the saturated quantity of $\overline{Q}_{RES}$, $\overline{Q}_{RES}^{MAX}$ increases with H_{DC} as well as α, as shown in Fig. 3.7(b). The underlying physics of these micromagnetic simulation results (symbols) will now be explained with the help of analytical derivation.

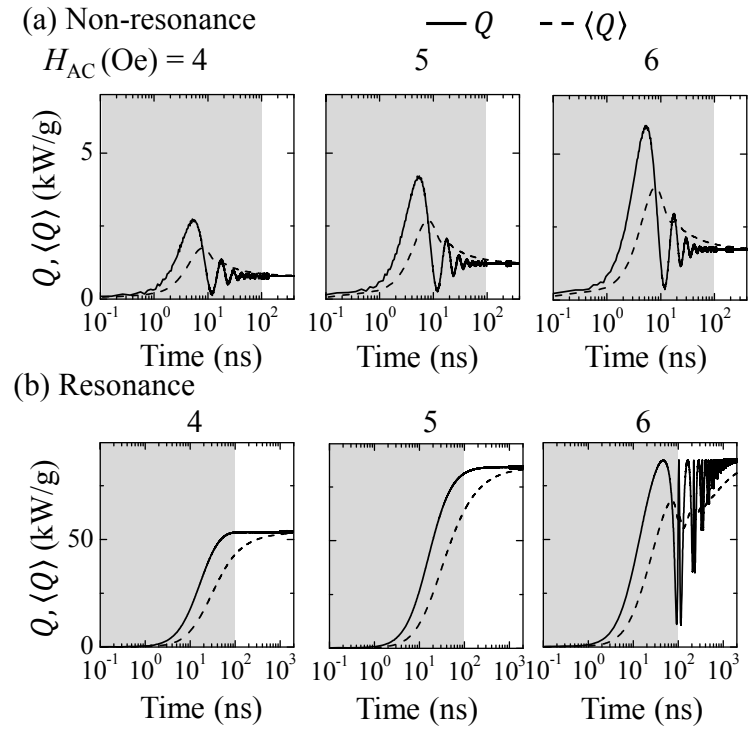

Fig. 3.4. Temporal evolution of energy-dissipation rate, Q, (solid line) and its time average $\langle Q \rangle$ (dashed line) for excitation of Py nanosphere of diameter $2R$ = 20 nm by H_{AC} = 5 Oe, H_{DC} = 100 Oe, α = 0.05, for (a) non-resonant case (f_{CCW} = 200 MHz) and (b) resonant case ($f_{CCW} = f_L$ = 280 MHz). The intervals between 0.1 ns and 100 ns are distinguished by the gray color.

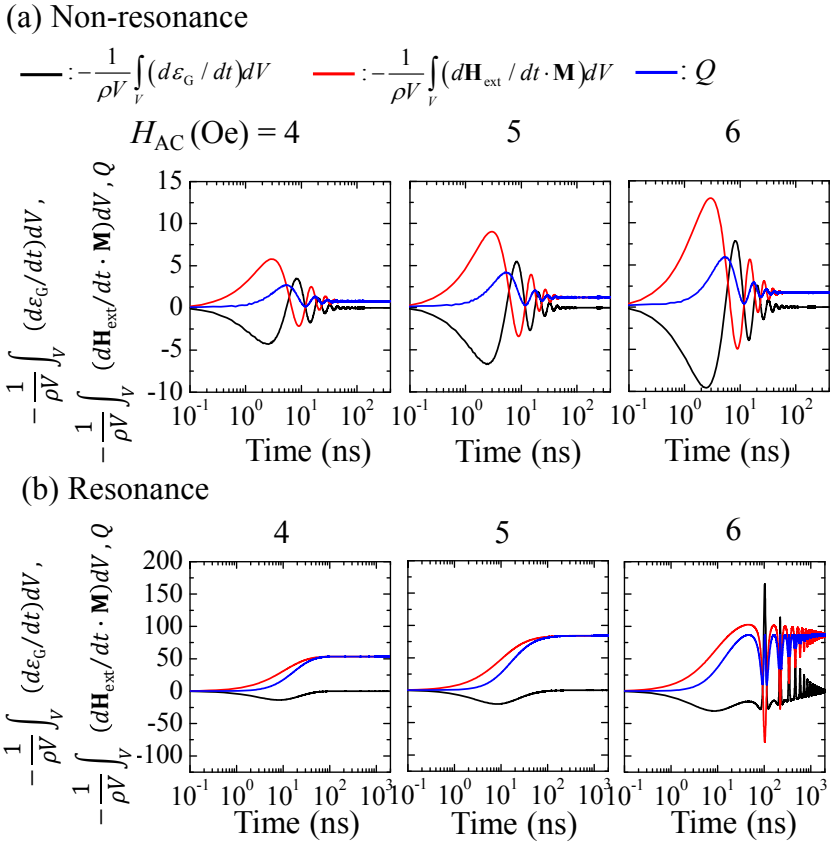

Fig. 3.5. Temporal evolution of energy-dissipation rate (blue), negative dual power density (red), and negative time derivative of total energy density (black) for excitation of Py nanosphere of diameter $2R$ = 20 nm by H_{AC} = 5 Oe, H_{DC} = 100 Oe, α = 0.05, for (a) non-resonant case (f_{CCW}= 200 MHz) and (b) resonant case (f_{CCW} = f_L= 280 MHz)

As shown from the simulation results (see Fig. 3.6) , $\bar{Q}$ can be simply determined from the dual power in the steady state assuming $d\varepsilon_G/dt = 0$:

$$\bar{Q} = \frac{M_s H_{AC} \omega_{CCW}}{\rho}(-u_y)$$
$$= \frac{M_s}{2\rho\gamma\alpha}\left[\frac{(\gamma H_{AC})^2 + (\alpha\omega_{CCW})^2 + (\omega_L - \omega_{CCW})^2 - }{\sqrt{\left[(\gamma H_{AC})^2 - (\alpha\omega_{CCW})^2 + (\omega_L - \omega_{CCW})^2\right]^2 + \left[2\alpha\omega_{CCW}(\omega_L - \omega_{CCW})\right]^2}}\right]. \quad (3.13)$$

From the analytical form of $\bar{Q}$, it is clear that $\bar{Q}$ is a function of $\omega_{CCW} = 2\pi f_{CCW}$, H_{AC}, H_{DC}, and α , because of $\omega_L = \gamma H_{DC}$. Thus, for a given material, the external field parameters of H_{DC}, H_{AC} as well as f_{CCW} determine the value of $\bar{Q}$. Using Eq. (3.13), we numerically calculated the $\bar{Q}$-versus-f_{CCW} behaviors (solid lines) for single-domain-state Py nanospheres of $2R$ = 10, 20, and 30 nm in the following cases: H_{DC} = 100 Oe, H_{AC} = 5 Oe and α = 0.01, 0.03, 0.05 and 0.07. As shown in Fig. 3.6, the analytical derivations were in excellent agreement with the micromagnetic simulation results (symbols). Moreover, the maximum values of $\bar{Q}$ were found at f_{CCW} = 280 MHz, which corresponds to the Py nanospheres' Larmor frequency expressed as $f_L = (\gamma/2\pi)H_{DC}$. The Larmor frequency in the case of single-domain-state nanoparticles does not change with $2R$, as reported in Ref [15]. Note that the largest quantity of $\bar{Q}$ was obtained at resonance by tuning f_{CCW} to f_L.

To gain deeper physical insight in the relations of $\bar{Q}_{RES}$ with H_{AC}, H_{DC}, and α as observed from the micromagnetic simulations shown in Fig. 3.7, we obtained the

analytical forms of $\bar{Q}_{RES}$ by inserting $f_{CCW} = f_L$ into Eq. (3.13):

$$\bar{Q}_{RES} = \frac{1}{\alpha}\left(\gamma M_s {H_{AC}}^2 / \rho\right) \qquad H_{AC} < \alpha H_{DC} \qquad (3.14a)$$

$$\bar{Q}_{RES} = \alpha\left(\gamma M_s {H_{DC}}^2 / \rho\right) \qquad H_{AC} \geq \alpha H_{DC} \qquad (3.14b)$$

The analytical calculations (solid lines) of Eq. (3.14) were in excellent agreement with the simulation results (symbols) already shown in Fig. 3.7. The quantity of $\bar{Q}_{RES}$ increases with H_{AC} in the form of H_{AC}^2 in the range of $H_{AC} < \alpha H_{DC}$, but becomes saturated to its maximum value of $\bar{Q}_{RES}^{MAX} = \alpha\left(\gamma M_s {H_{DC}}^2 / \rho\right)$ in the range of $H_{AC} \geq \alpha H_{DC}$. This saturated quantity is independent of H_{AC} but increases with H_{DC}^2, as shown in Fig. 3.7(b). Interestingly, at a certain critical value of $H_{AC} = \alpha H_{DC}$, Eq. (3.14a) equals Eq. (3.14b). For $H_{AC} < \alpha H_{DC}$, $\bar{Q}_{RES}$ is inversely proportional to α, but for the case of $H_{AC} \geq \alpha H_{DC}$, it proportionally increases with α and H_{DC}^2, as shown in Fig. 3.7. According to the given values of H_{AC} and H_{DC}, $\bar{Q}_{RES}$ can vary proportionally or inversely proportionally with α. Therefore, the quantity of $\bar{Q}_{RES}$ can be readily manipulated by tuning each of H_{AC}, H_{DC}, and α. Eqs. (3.14a) and (3.14)'s benefit is their informing us why $\bar{Q}_{RES}$ increases with α up to 0.05 and then decreases with α = 0.07, as shown in Fig. 3.6. For the given condition imparted by H_{AC} = 5 Oe and H_{DC} = 100 Oe, $\bar{Q}_{RES}$ increases with α for the cases of α = 0.01, 0.03, and 0.05, but decreases again for α = 0.07, as shown in Fig. 3.6.

Also, it was indicated that the maximum value of $\bar{Q}_{\mathrm{RES}}^{\mathrm{MAX}} = \alpha\left(\gamma M_{\mathrm{s}} {H_{\mathrm{DC}}}^2 / \rho\right)$ under the $H_{\mathrm{AC}} \geq \alpha H_{\mathrm{DC}}$ condition is the highest energy-dissipation rate at resonance for a given nanosphere in the single-domain state with intrinsic damping parameter α and static field strength H_{DC}. This fact informs us that Gilbert damping is not the only control parameter but rather, the $H_{\mathrm{AC}}/H_{\mathrm{DC}}$ ratio is another important factor in obtaining the largest value of $\bar{Q}_{\mathrm{RES}}$. The quantity of $\bar{Q}_{\mathrm{RES}}^{\mathrm{MAX}}$ for single-domain Py particles can reach $10^4 – 10^5$ W/g, which is two or three orders of magnitude larger than the typical SLP values of $10^2 – 10^3$ W/g for magnetic hyperthermia based on other mechanisms (Table. 3.1). One such mechanism is the Linear Response Theory (LRT), which describes the dynamic response of an assembly of magnetic nanoparticles using the Néel-Brown relaxation model. The assumption of this model is that magnetic systems respond linearly with externally applied magnetic field, as in $\mathbf{M} = \tilde{\chi}\mathbf{H}_{\mathrm{Linear}}$, where $\tilde{\chi}$ is the complex susceptibility given by $\tilde{\chi} = \chi_0 \dfrac{1}{1 + i\omega_{\mathrm{Linear}}\tau_{\mathrm{R}}}$, with the χ_0 static susceptibility, ω_{Linear} the angular frequency of linearly oscillating magnetic field, and τ_{R} the relaxation time to attainment of the equilibrium state. For aligned magnetic nanoparticles of zero magnetic anisotropy constant (K_{eff}), the SLP is given as $\langle Q \rangle = \dfrac{{H^2}_{\mathrm{Linear}} {M_{\mathrm{S}}}^2}{6k_{\mathrm{B}}T\rho} \dfrac{{\omega_{\mathrm{Linear}}}^2 {\tau_{\mathrm{R}}}}{(1 + {\omega_{\mathrm{Linear}}}^2 {\tau_{\mathrm{R}}}^2)}$, and for aligned magnetic nanoparticles with a strong anisotropy, the SLP is given as $\langle Q \rangle = \dfrac{{H^2}_{\mathrm{Linear}} {M_{\mathrm{S}}}^2}{2k_{\mathrm{B}}T\rho} \dfrac{{\omega_{\mathrm{Linear}}}^2 {\tau_{\mathrm{R}}}}{(1 + {\omega_{\mathrm{Linear}}}^2 {\tau_{\mathrm{R}}}^2)}$ for the given temperature T [32]. The LRT model is valid for cases where magnetic nanoparticles

are under the superparamagnetic limit, assuming $\frac{M_S V H_{\text{Linear}}}{k_B T} \ll 1$ and $\frac{H_{\text{Linear}}}{H_K} \ll 1$, as verified in a large number of experimental studies for anisotropy field H_K [19,32-35]. However, for cases where nanoparticles are close to or over the superparamagnetic limit, the LRT model does not work anymore. In cases where the magnetic anisotropy energy barrier of a given material is greater than the thermal fluctuation, i.e., $\frac{M_S V H_{\text{Linear}}}{k_B T} > 1$, the Stoner-Wohlfarth model (SWM) [36] is more valid for description of the field-dependent magnetic hysteresis loops and the related SLP. Therefore, SLP can be described as $\langle Q \rangle = 4 f_{\text{Linear}} H_K M_S / \rho$. The typical values of SLP are within the range of several hundreds of W/g for the LRT model and several thousands of W/g for the SWM model [32], as compared in Table (3.1).

The advantage of the Resonant Spin Excitation (RSE) model proposed in this study is its utilization of resonant magnetization excitations by externally controllable magnetic fields; the other models, contrastingly, are associated with the intrinsic characteristics of materials (e.g., the relaxation time and the magnetic anisotropy field) as key factors in energy-dissipation. In our RSE model, the maximum energy-dissipation rate can be achieved and readily controlled using only H_{AC} and H_{DC}, whose strengths are as small as 10^{-2} — an order of magnitude smaller than those of the other models — in order to obtain extremely high values (up to 10^4 – 10^5 W/g) at resonance when tuning the oscillating field frequency to the Larmor precession frequency. This is a remarkable achievement: the RSE model is expected to attain an SLP 10^2 times higher than those of the conventional methods by application of extremely small amplitude of AC magnetic field. Also, the model can be extended to

energy dissipation for superparamagnetic nanoparticles that exhibit a super paramagnetic resonance effect [37, 38].

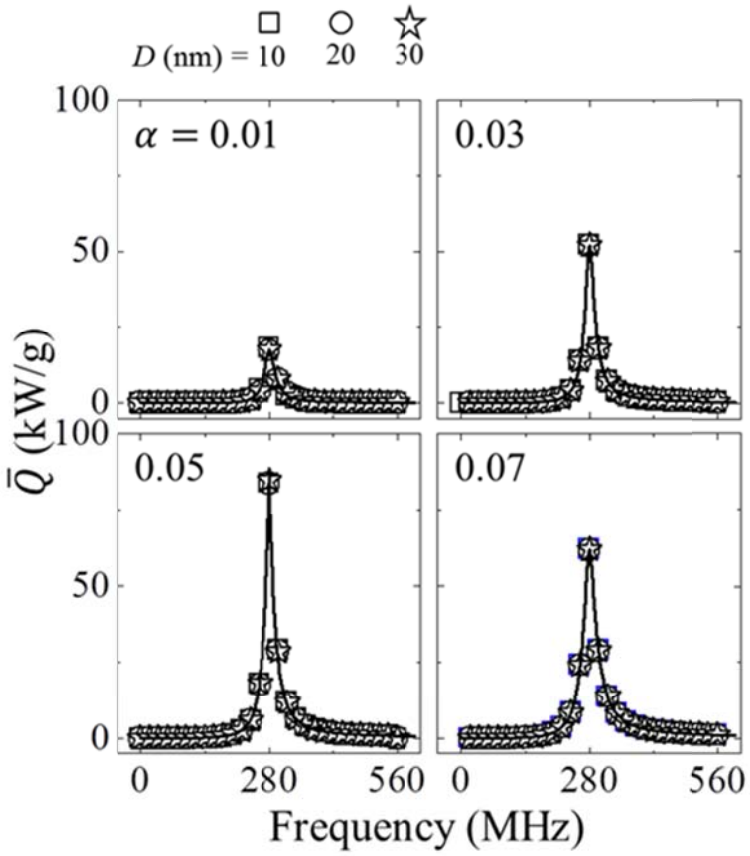

Fig. 3.6. Energy-dissipation rate in steady-state regime as function of frequency of circular-rotating fields for excitation of Py nanospheres of diameter $2R$ = 10, 20, 30 nm with H_{AC} = 5 Oe, H_{DC} = 100 Oe, α = 0.01, 0.03, 0.05 and, 0.07. The symbols and lines represent the micromagnetic simulation and analytical calculation results, respectively.

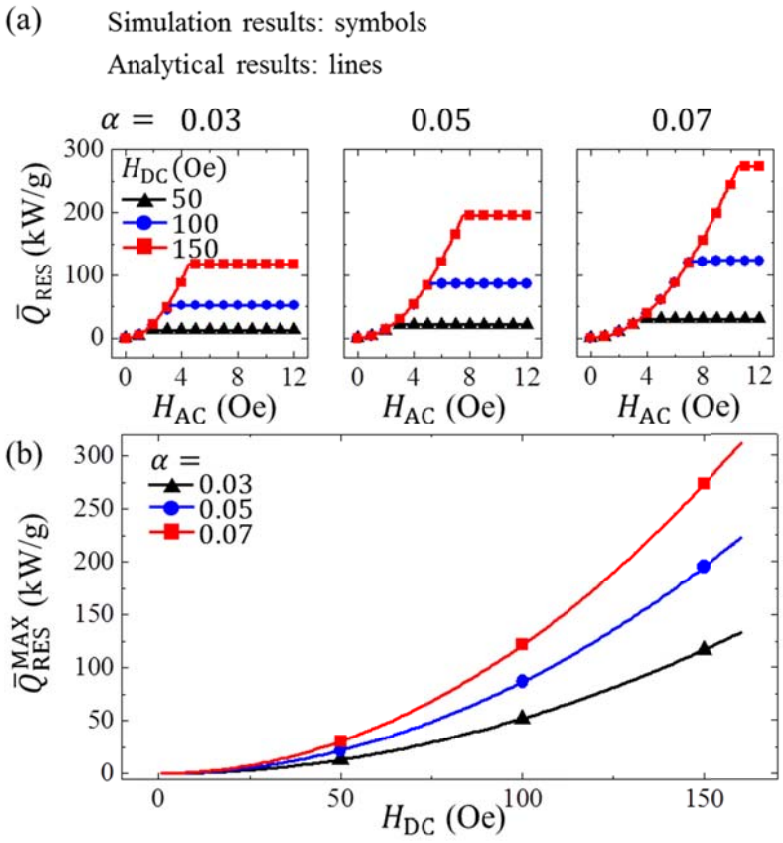

Fig. 3.7. (a) Steady-state energy-dissipation rate at corresponding resonance frequencies as function of H_{AC} for $2R$ = 20 nm with different static field strengths (H_{DC} = 50, 100, 150 Oe) for given damping constants (α = 0.03, 0.05, 0.07). (b) Maximum energy-dissipation rate versus H_{DC} for given damping constants. The symbols and lines indicate the micromagnetic simulation and analytical calculation results, respectively.

Model	LRT[a]	SWM[a,b]	RSE[c]
Mechanism	Thermal-fluctuation-dominated relaxation	Magnetic anisotropy energy barrier	Resonant precession motion
Main factor	τ_R	H_K	α , H_{DC}
Particle size, D	$D <$ Superparamagnetic limit	Superparamagnetic limit $< D <$ Single-domain limit	$D <$ Single-domain limit
Oscillating field Frequency (MHz)	0.01 ~ 1	0.01 ~ 1	100 ~ 1000
Oscillating field amplitude (Oe)	100 ~ 1000	100 ~ 1000	1 ~ 10
SLP (Eqs)	$\lim_{\frac{K_{eff}V}{k_BT}\to 0}\langle Q\rangle = \frac{H^2_{Linear}M_S^2}{6k_BT\rho}\frac{\omega_{Linear}^2\tau_R}{(1+\omega_{Linear}^2\tau_R^2)}$ or $\lim_{\frac{K_{eff}V}{k_BT}\to \infty}\langle Q\rangle = \frac{H^2_{Linear}M_S^2}{2k_BT\rho}\frac{\omega_{Linear}^2\tau_R}{(1+\omega_{Linear}^2\tau_R^2)}$	$\langle Q\rangle = 4f_{Linear}H_KM_S/\rho$	$\bar{Q}_{RES} = \frac{1}{\alpha}\left(\gamma M_s H_{AC}^2/\rho\right)$ for $H_{AC} < \alpha H_{DC}$ or $\bar{Q}_{RES} = \alpha\left(\gamma M_s H_{DC}^2/\rho\right)$ for $H_{AC} \geq \alpha H_{DC}$
Order of SLP (W/g)	~ 100	~ 1,000	~ 10,000 – 100,000

[a]Reference [32]

[b]Reference [19]

[c]Present study

Table 3.1. Comparison of characteristics of three models

3.4. References

[1] L. Néel, Ann. Géophys. **5**, 99 (1949).

[2] W. F. Brown Jr, Phys. Rev. **130**, 1677 (1963).

[3] E. M. Chudnovsky, J. Appl. Phys. **73**, 6697 (1993).

[4] L. Thomas, F. Lionti, R. Ballou, and D. Gatteschi, Nature **383**, 145 (1996).

[5] J. Nogués, J. Sort, V. Langlais, V. Skumryev, S. Surinach, J. Munoz, and M. Baró, Phys. Rep. **422**, 65 (2005).

[6] C. A. Ross, Annu. Rev. Mater. Res. **31**, 203 (2001).

[7] A. Moser, K. Takano, D. T. Margulies, M. Albrecht, Y. Sonobe, Y. Ikeda, S. Sun, and E. E. Fullerton, J. Phys. D: Appl. Phys. **35**, R157 (2002).

[8] S. Wolf, D. Awschalom, R. Buhrman, J. Daughton, S. Von Molnar, M. Roukes, A. Y. Chtchelkanova, and D. Treger, Science **294**, 1488 (2001).

[9] I. Žutić, J. Fabian, and S. D. Sarma, Rev. Mod. Phys. **76**, 323 (2004).

[10] T. Shinjo, Nanomagnetism and spintronics (Elsevier, 2013).

[11] Q. A. Pankhurst, J. Connolly, S. K. Jones, and J. Dobson, J. Phys. D: Appl. Phys. **36**, R167 (2003).

[12] V. Labhasetwar and D. L. Leslie-Pelecky, Biomedical applications of nanotechnology (John Wiley & Sons, 2007).

[13] M. Ferrari, Nat. Rev. Cancer. **5**, 161 (2005).

[14] J. Gao, H. Gu, and B. Xu, Acc. Chem. Res. **42**, 1097 (2009).

[15] S.-K. Kim, M.-W. Yoo, J.-H. Lee, Y. Gaididei, V. P. Kravchuk, and D. D. Sheka, Sci. Rep. **5**, 11370 (2015).

[16] S.-K. Kim, M.-W. Yoo, J. Lee, J.-H. Lee, and M.-K. Kim, Sci. Rep. **6**, 31513 (2016).

[17] T. Neuberger, B. Schöpf, H. Hofmann, M. Hofmann, and B. Von Rechenberg, J. Magn. Magn. Mater. **293**, 483 (2005).

[18] M. Shliomis, Phys. Usp. **17**, 153 (1974).

[19] R. Hergt, S. Dutz, R. Müller, and M. Zeisberger, J. Phys: Condens. Matter **18**, S2919 (2006).

[20] T. Schrefl and J. Fidler, J. Magn. Magn. Mater. **155**, 389 (1996).

[21] A. S. Szalay, J. Gray, G. Fekete, P. Z. Kunszt, P. Kukol, and A. Thakar, arXiv preprint cs/0701164 (2007).

[22] P. De Châtel, I. Nándori, J. Hakl, S. Mészáros, and K. Vad, J. Phys: Condens. Matter **21**, 124202 (2009).

[23] I. Nándori and J. Rácz, Phys. Rev, E **86**, 061404 (2012).

[24] T. Lyutyy, S. Denisov, A. Y. Peletskyi, and C. Binns, Phys. Rev. B **91**, 054425 (2015).

[25] S. I. Denisov, T. V. Lyutyy, P. Hänggi, and K. N. Trohidou, Phys. Rev. B **74**, 104406 (2006).

[26] T. Roubíček, G. Tomassetti, and C. Zanini, J. Math. Anal. Appl. **355**, 453 (2009).

[27] J. Rácz, P. De Chatel, I. Szabó, L. Szunyogh, and I. Nándori, Phys. Rev. E **93**, 012607 (2016).

[28] P. Déjardin, Y. P. Kalmykov, B. Kashevsky, H. El Mrabti, I. Poperechny, Y. L. Raikher, and S. Titov, J. Appl. Phys. **107**, 073914 (2010).

[29] P.-M. Déjardin and Y. P. Kalmykov, J. Magn. Magn. Mater. **322**, 3112 (2010).

[30] P. Cantillon-Murphy, L. L. Wald, E. Adalsteinsson, and M. Zahn, J. Magn. Magn. Mater. **322**, 727 (2010).

[31] B. Mehdaoui, J. Carrey, M. Stadler, A. Cornejo, C. Nayral, F. Delpech, B. Chaudret, and M. Respaud, Appl. Phys. Lett. **100**, 052403 (2012).

[32] J. Carrey, B. Mehdaoui, and M. Respaud, J. Appl. Phys. **109**, 083921 (2011).

[33] R. Hiergeist, W. Andrä, N. Buske, R. Hergt, I. Hilger, U. Richter, and W. Kaiser, J. Magn. Magn. Mater. **201**, 420 (1999).

[34] X. Wang, H. Gub and Z. Yang, J. Magn. Magn. Mater. **293**, 334 (2005).

[35] B. Mehdaoui, A. Meffre, L.-M. Lacroix, J. Carrey, S. Lachaize, M. Respaud, M. Gougeon, and B. Chaudret, J. Appl. Phys. **107**, 09A324 (2010).

[36] E. C. Stoner and E. P. Wohlfarth, Philos. Trans. R. Soc. London, Ser. A **240**, 599 (1948).

[37] . Berger, J. Kliava, J. C. Bissey, and V. Baïetto, J. Phys.: Condens. Matter **10**, 8559 (1998).

[38] S. V. Titov, P.-M. Dejardin, H. El Mrabti, and Y. P. Kalmykov, Phys. Rev. B **82**, 100413(R) (2010).

Chapter 4

A Study on the Physical Origin of Low Frequency and High Efficiency Energy-dissipation Due to Resonant Precession of Magnetic-vortex Core

4.1. Introduction

The precession of spins inside magnetic nanoparticle is a universal dynamic phenomenon in nature that represents the precession of a magnetic moment about a magnetic field at a characteristic frequency (Larmor frequency for single spin), which is expressed as $f_L = (\gamma / 2\pi)H_{DC}$, where γ is gyromagnetic ratio and H_{DC}, the static field strength. This type of precession plays very important roles in a rich variety of applications such as analysis of material [1,2], information storaging [3,4] and bio-medical imaging (MRI, MPI) [5,6]. As an example, in our earlier study, soft magnetic nanoparticles in single-domain states exhibit collective Larmor precession of individual spins. In cases where the frequency of time-varying magnetic fields equals the Larmor precession frequency, individual magnetic moments efficiently absorb energies that are transferred from externally applied AC magnetic fields, after which those energies dissipate into other forms due to their intrinsic damping of given materials. Such energy-dissipations of magnetic nanoparticles provides the highest

SLP (Specific Loss Power) value, on the order of 10^4 – 10^5 W/g, and enables ready controllability by externally applied magnetic fields using single-domain magnetic particles in magnetic hyperthermia applications (chapter 3). From this research, we report that there was a possibility of generating heat more than 100 times higher than the conventional heating mechanism for hyperthermia, but the range of frequency of applied magneetic field is several hundreds MHz ~ several GHz, which is technically difficult to generate. As for soft-magnetic nano-sphere, our previous papers [7, 8] reported that they bear specific spiral magnetizations around a uniformly magnetized core region, the so-called vortex core, in cases where the particle diameter is larger than single-domain size but smaller than multiple-domain size. We have also demonstrated using magnetic holography technique that magnetic-vortex is present in Py nanoparticles above a certain size (see Fig. 4.1) [9]. As shown in ref. [7], the vortex core in nano-spheres is found to exhibit a unique precession motion around the direction of an externally applied static field, and, further, the precession frequency is determined by the sphere size as well as the static field strength. The core precession thus can be excited with high energy-dissipation when the frequency of an externally applied AC magnetic field is tuned to the eigen frequency of the core-precession mode, though eigen frequency is sufficiently reduced from that of precession in single-domain state.

In the present study, we explored energy-dissipation of magnetic vortex state driven by AC magnetic fields with the assistance of excited vortex-core precession in soft magnetic nano-spheres. This energy-dissipation of magnetic vortex is completely different from typical resonant frequency-assisted energy-dissipation in single-domain

nano sphere. The relevant dynamics serve as a robust mechanism of efficient energy-dissipation from vortex-state magnetic particles: application of sufficiently weak AC magnetic fields and low frequencies allow for resonant energy-dissipation from external magnetic fields to vortex-state nano-spheres. Such an efficient means of high power and low frequency energy-dissipation rate could be implemented in possible future bio-diagnostic and magnetic-hyperthermia-treatment applications.

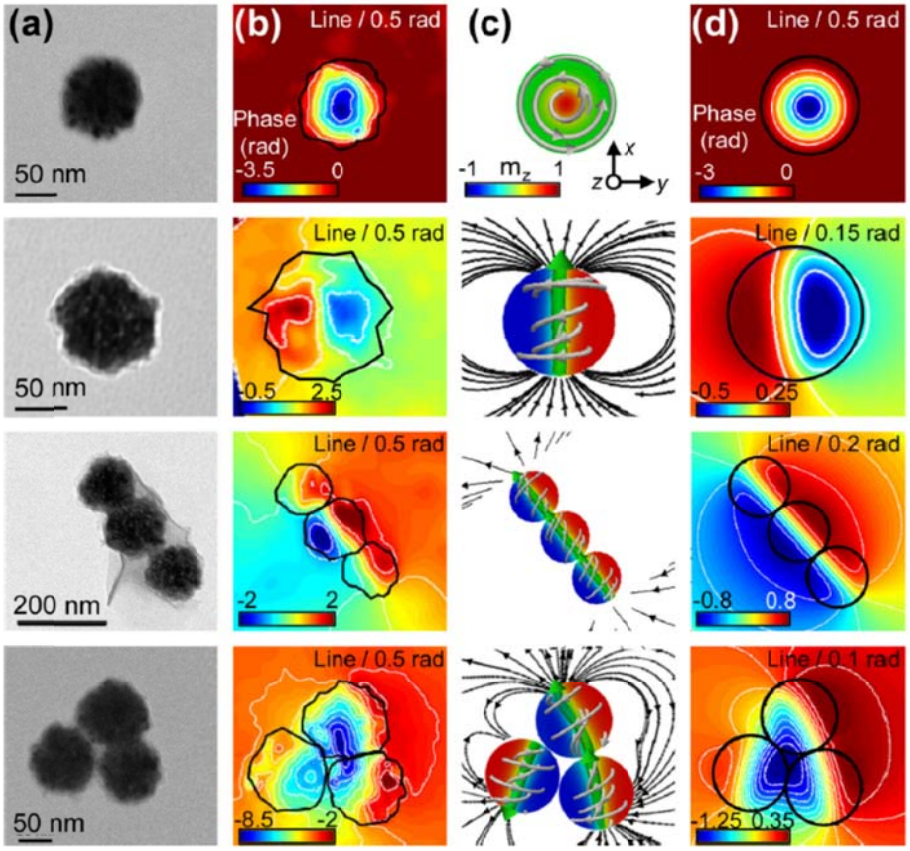

Fig. 4.1. (a) Bright-field TEM images of single Py nanoparticle, triple-particle linear, and triple-particle triangular arrangements. (b) Magnetic phase-shift images of corresponding particles, as obtained by EH imaging. (c) 3D spin configurations obtained by micromagnetic simulations and (d) correspoinding magnetic phase-shift images. In (b) and (d), the contour lines correspond to the isophase lines (the radian separation is indicated in each image).

4.2. Modeling

We conducted finite-element micromagnetic simulations of soft magnetic Permalloy (Py, $Ni_{80}Fe_{20}$) nanospheres in single domain states and magnetic vortex state, the diameters of which were set to $2R$ = 10 ~ 75 nm. To numerically solve dynamic motions of magnetizations (**M**), we used the FEMME code (version 5.0.9) [10] that utilizes the Landau-Lifshitz-Gilbert (LLG) equation.

The magnetic parameters corresponding to the Py material were as follows: saturation magnetization M_s = 860 emu/cm^3, exchange stiffness A = 1.3 × 10^{-6} erg/cm, gyromagnetic ratio $\gamma = 2\pi \times 2.8$ rad · MHz/Oe, and zero magneto-crystalline anisotropy. To avoid errors inherent to representation of a spherical geometry with a set of cubic cells, we opted for triangular tessellation using Hierachial Triangular Mesh [11], and the inner volume into tetrahedron elements (mesh size ≤ 3 nm) (see Fig. 4.2(a)).

Through relaxation from initially saturated magnetizations oriented in the +z-direction for the Py nanospheres, we obtained single-domain ground states for each diameter $2R$ = 10 ~ 35 nm and magnetic vortex state for $2R$ = 35 ~ 75 [7]. For the Py spheres, the single-domain states were maintained up to $2R$ = ~ 35 nm, which states are the results of competition between strong short-range exchange and weak long-range interactions along with such nano-scale geometrical confinements. Figure 4.2(b) shows the ground state of a permalloy (Py) nano-sphere of $2R$ = 50 nm diameter as obtained by relaxation from the saturated magnetizations in the +z-direction. The spin microstructure indicates a rather uniformly magnetized vortex core with spiral

magnetizations around the core. Because the spheres are magnetically isotropic insofar as there is no other sources of anisotropy [12, 13], vortex-core can reorient to the direction of applied static magnetic fields. It is well known that such magnetic-vortex particles exhibit collective precession motions of individual spins around the axis of a static magnetic field with following characteristic resonance frequency [7, 8]:

$$f_{\mathrm{RES}} = (\gamma_{\mathrm{eff}} / 2\pi) H_{\mathrm{DC}} \qquad (4.1)$$

where H_{DC} is the static field strength and γ_{eff} is the effective gyromagnetic ratio, which is expressed by $\gamma_{\mathrm{eff}} = \langle m_{\Gamma} \rangle \gamma$. The $\langle m_{\Gamma} \rangle$ is the average magnetization component over the sphere volume in the vortex-core orientation. In Fig. 4.2(d), $\langle m_{\Gamma} \rangle$ obtained by micromagnetic simulation was plotted against sphere diameter, 2*R*. As reported by ref [7], $\langle m_{\Gamma} \rangle$ decreases sharply as the particle size increases, so the resonance frequency also decreases according to Eq. (4.1).

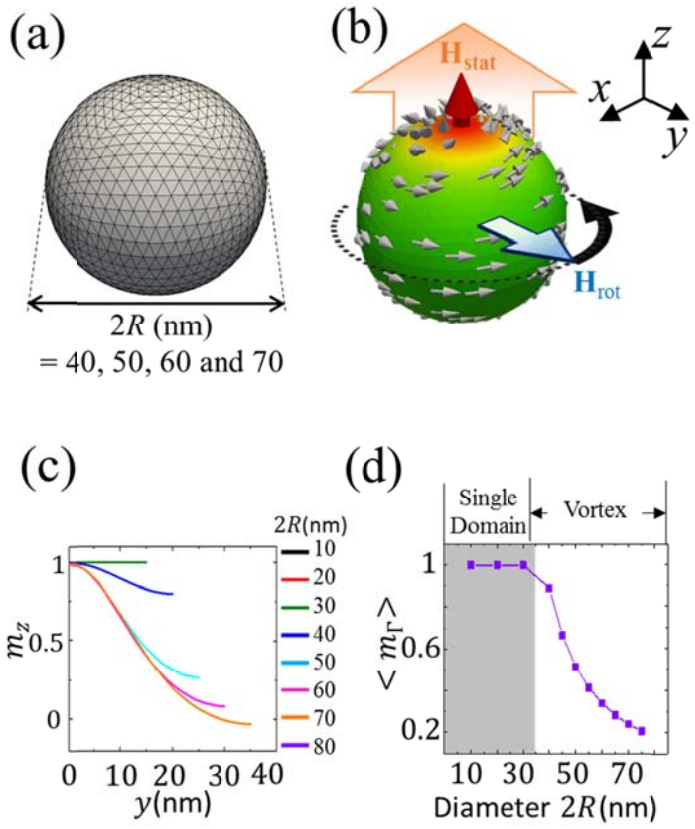

Fig. 4.2. (a) Finite-element sphere model of diameter $2R$ = 10 – 75 nm. (b) Magnetic-vortex sphere model of diameter $2R$ = 50 nm under circular-rotating field and static field. (c) m_z profile along y-axis for different diameters. (d) $\langle m_r \rangle$ obtained from micromagnetic calculations for different diameters.

4.3. Results and Discussion

4.3.1. Characteristic Dyanmic Motions of Magnetic-vortex Core

To investigate the resonantly excited dynamic motions of the magnetic vortex of the Py spheres, we applied a static field $\mathbf{H}_{\text{stat}} = H_{\text{DC}}\hat{\mathbf{z}}$ in the +z-direction, which allows for the reorientation of the vortex core in the +z-direction. Since the characteristic precession motion of vortex-core is counter-clockwise (CCW) in its rotation sense, we chose the CCW basis of circular-rotating magnetic fields on the x-y plane, as described by $\mathbf{H}_{\text{rot}} = H_{\text{AC}}\cos\left(2\pi f_{\text{RES}}t\right)\hat{\mathbf{x}} + H_{\text{AC}}\sin\left(2\pi f_{\text{RES}}t\right)\hat{\mathbf{y}}$ with the field strength H_{AC} and the resonance frequency f_{RES} (see Fig. 4.2(b)). In order to compare the difference of the precession of the magnetization of the single-domain state and the magnetic vortex-core, we also performed a similar simulation for the sphere with single-domain state. For $2R$ = 20 and 50 nm under H_{DC} = 100 Oe, Fig. 4.3 shows the characteristic precession motion of unit vector $\mathbf{m} = \mathbf{M}/M_{\text{s}}$ and vortex-core $\boldsymbol{\Gamma}$ excited by two different resonance frequencies, f_{RES} = 280 and 114 MHz, each of H_{AC} = 5, 6, 7 and 8 Oe. Since the $\langle m_{\Gamma}\rangle$ for the Py sphere of $2R$ = 20 and 50 nm is 1 and 0.54, respectively, the application of f_{RES} = 280 and 114 MHz would lead to resonant excitations in accordance to Eq. (4.1) for H_{DC} = 100 Oe. For both single-domain and magnetic vortex (see Fig. 4.3), the precession motions occur with large in-plane $\mathbf{m}$ and $\boldsymbol{\Gamma}$ components, even for the very small field strengths H_{AC} = 5, 6, 7, and 8 Oe. All of the dynamic motions for the individual cases finally reach their corresponding steady

states with specific m_z and Γ_z values according to the given H_{AC} value. However, the magnetization of single-domaint state and the magnetic-vortex showed a big difference in detailed dynamic motion. For single-domain state (see Fig. 4.3(a)), magnetization reversal occurred under the condition of $H_{AC} > \alpha H_{DC}$ (αH_{DC} = 5 for given field strength and damping constant). Beyond H_{AC} = 6 Oe, for example, the **m** periodically oscillates (switches) between the +*z* and –*z*-directions before converging to the precession motion exactly on the equator, i.e., keeping m_z = 0. This magnetization reversal creteria for resonance condition has already revealed in previous chapter. For magnetic-vortex state (see Fig. 4.3(b)), even under H_{AC} = 6 Oe, the magnetic-vortex core did not show reversal movement. The vortex-core started reversal movement for the first time when H_{AC} exceeds 7 Oe. In addition, the single-domain magnetization reversal motion changes m_z to 0 rotating around the equator when it is in a steady state over time (chapter 3). However, as shown in Fig. 4.3(b), the *z*-component of vortex-core orientation, Γ_z, is considerably larger than 0, even for steady state. This fact apparently demonstrates that the steady state dynamics of the magnetic-vortex differs from that of the single-domain state.

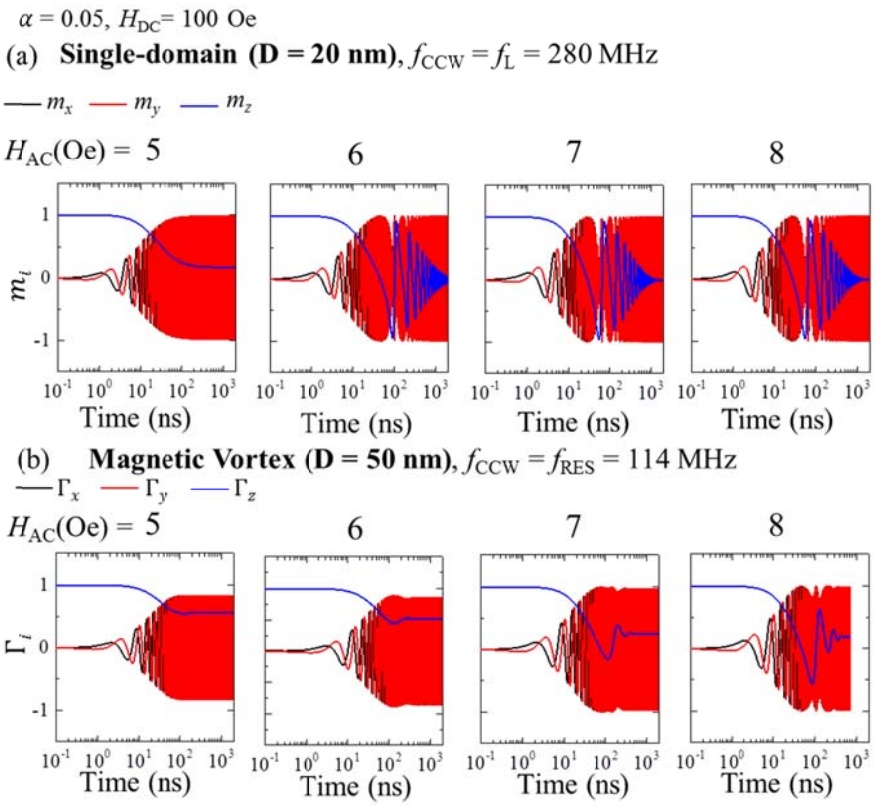

Fig. 4.3. Temporal evolution of *x*-, *y*-, and *z*-components of **m** and **Γ** for different strengths of circular-rotating fields H_{AC} = 5, 6, 7, and 8 for (a) single-domain case (f_{RES} = 280 MHz, $2R$ = 20 nm) and (b) magnetic-vortex case (f_{RES} = 114 MHz, $2R$ = 50 nm). The static field strength H_{DC} = 100 Oe and damping constant α = 0.05 were used for all of the simulations shown in this figure.

4.3.2. Energy-dissipation Rate of Magnetic-vortex State

Above, we explored the resonant dynamic motions of the magnetizations of Py nanospheres in both the single-domain states and magnetic vortex state. We confirmed that the dynamics of single-domain and magnetic vortex showed a big difference. So, we tried to examine the effect of this difference of dynamics on energy-dissipation. Organizing, the resonance frequency of precession motion of vortex-core is much smaller than the resonance frequency of single-domain state. In addition, the threshold field strength that generates the reversal motion of the vortex-core has been found to be larger than that of the magnetization of single-domain state ($H_{\mathrm{AC}}{}^{\mathrm{th}} = \alpha H_{\mathrm{DC}}$) and the vortex-core does not rotate on the equator even after reaching a steady state over time. The unique non-linear dynamics of magnetic-vortex, which is different from single-domain state, causes energy-dissipation, and the energy-dissipation is directly related to SLP in the research field of hyperthermia. On the basis of energy conservation and fundamental Maxwell equations, the power loss can be represented by the magnetic energy-dissipation rate in the form of Watt/gram (W/g), and can be expressed as [14]

$$Q = -\frac{1}{\rho V}\int_V \left(d\varepsilon_{\mathrm{G}} / dt + \mathbf{M}(t) \cdot d\mathbf{H}_{\mathrm{ext}}(t) / dt \right) dV , \qquad (4.2)$$

where ε_{G} is the Gibbs' energy density with the volume of nanosphere V and the density of permalloy $\rho = 8.72$ g/cm^3. The first and second terms on the right side are the time derivative of magnetic energy and the dual power of external force, respectively (for details, see Ref [14]). Accordingly, from our micromagnetic simulation data, we can directly obtain the quantities of Q versus a given time for the

nonlinear dynamic motions of a single-domain and magnetic-vortex nanosphere of 2R = 20 and 50 nm for the specific cases of H_{DC} = 100 Oe and α = 0.05, as excited by two different resonant frequencies, f_{RES} = 280 (for single-domain) and 114 MHz (for magnetic-vortex) for each of the different values of H_{AC} = 5, 6, 7, and 8 Oe. And we compares the individual Q values as well as the negative derivative of energy density $-\frac{1}{\rho V}\int_{\Omega}\left(d\varepsilon_{G}/dt\right)dV$ and negative dual power density $-\frac{1}{\rho V}\int_{\Omega}\left(d\mathbf{H}_{ext}/dt\cdot\mathbf{M}\right)dV$ calculated from the simulation results for the single-domain and magnetic-vortex conditions. As shown in Fig. 4.4, for all of the cases, the $-\frac{1}{\rho V}\int_{\Omega}\left(d\varepsilon_{G}/dt\right)dV$ (black line) converges to zero in the steady states, but the $-\frac{1}{\rho V}\int_{\Omega}\left(d\mathbf{H}_{ext}/dt\cdot\mathbf{M}\right)dV$ (red color) becomes equal to Q; hereafter, the Q quantity in the steady state is noted as $\overline{Q}$. For both single-domain state and magnetic-vortex, the time derivatives of energy density and dual power work converge to certain values after about 1000 ns. In particular, it is necessary to pay attention to the fact that time derivatives of energy density converges to 0. Therefore, $\overline{Q}$ is determined only by the dual power density. For single-domain state, using an H_{AC} value larger than 5 Oe, for example 6 Oe, those energy powers oscillate with large fluctuations before reaching the steady state, which oscillations are related to magnetization switching between the +z and –z directions, as already shown in Fig. 4.3(a). In the case of magnetic-vortex, the values of Q and the $-\frac{1}{\rho V}\int_{\Omega}\left(d\mathbf{H}_{ext}/dt\cdot\mathbf{M}\right)dV$ slowly increase and then converge to certain corresponding values, even when H_{AC} exceeds 5 Oe and reaches 7 Oe. When H_{AC} is 8 Oe, the energy powers start to oscillate with large fluctuations, as in

the case of H_{AC} = 6, 7, and 8 Oe in the single-domain case before reaching a steady state. However, the frequencies at which energy powers oscillate are much smaller than those of the single-domain state. This is because the vortex-core reversal frequency is smaller than that of the magnetization of the single-domain state. As reported by earlier studies [8], the reversal frequency f_{REV} is proportional to H_{AC} for both single-domain and magnetic vortex state, as expressed by $f_{REV} = (\gamma_{eff}/2\pi) H_{AC} = (\gamma/2\pi)\langle m_{\Gamma}\rangle H_{AC}$. In the above equation, $\langle m_{\Gamma}\rangle$ is 1 for single-domain state and $\langle m_{\Gamma}\rangle$ for magnetic-vortex state is less than 1, so that the f_{REV} for vortex-core reversal becomes smaller than that of a single-domain, and consequently also applies to oscillations of energy powers.

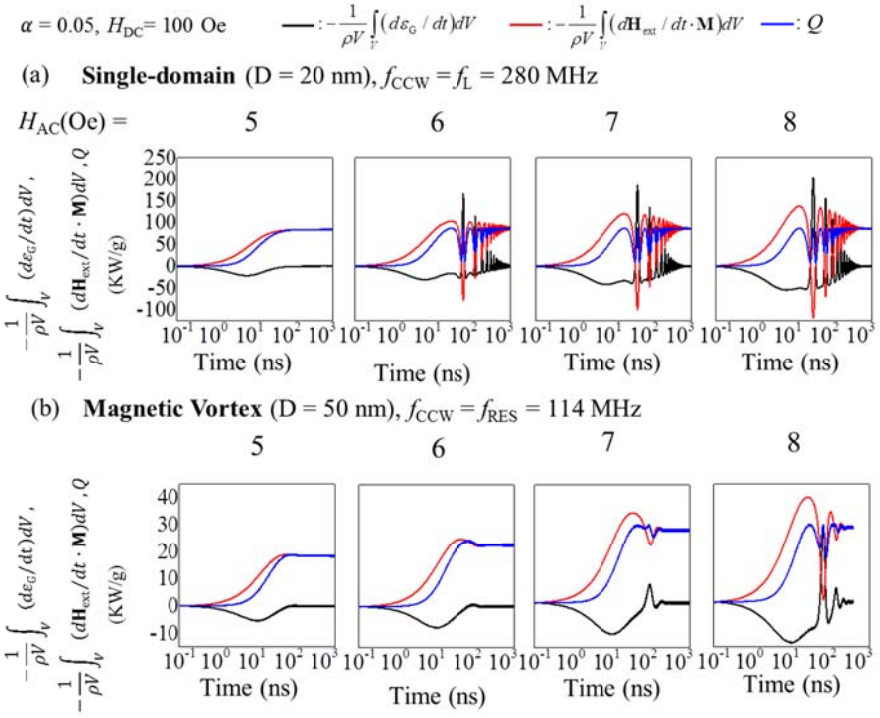

Fig 4.4. Temporal evolution of energy-dissipation rate (blue), negative dual power density (red), and negative time derivative of total energy density (black) for resonant excitation of Py nanosphere by H_{AC} = 5 Oe, H_{DC} = 100 Oe, α = 0.05, for (a) single-domain case (f_{RES} = 280 MHz, $2R$ = 20 nm) and (b) magnetic-vortex case (f_{RES} = 114 MHz, $2R$ = 50 nm).

As reported in chapter 3, the steady state energy-dissipation $\bar{Q}$ could be treated the same as the measurable SLP, from now on, we focus only on $\bar{Q}$ values that can be numerically calculated from the micromagnetic simulation data shown in Fig. 4.5. For the single-domain and magnetic-vortex cases, the quantities of $\bar{Q}$ contrast starkly. In order to compare $\bar{Q}$ for different sphere radius as a function of f_{CCW}, we conducted micromagnetic simulations by varying f_{CCW} within the 20 – 540 MHz range; then, from the simulation results, we numerically calculated $\bar{Q}$ versus f_{CCW}. As shown in Fig. 4.5, under the application of H_{DC} = 100 Oe, H_{AC} = 5 Oe, α = 0.01, we plotted $\bar{Q}$ values versus f_{CCW} for the different radius of Py nanospheres of $2R$ =10 ~ 70 nm in single-domain states and magnetic vortex. As is apparent, there were clear peaks of $\bar{Q}$ when f_{CCW} reached $f_{RES} = (\gamma_{eff} / 2\pi)H_{DC}$ for each size of the particles. As described above, as the particle size increases, the precession frequency of vortex-core decreases, so the frequencies at which $\bar{Q}$ peaks occur decreases more and more. It was also confirmed that the height of peaks at each resonance frequency also decreases as the particle size increases. Such a quantity of $\bar{Q}$ at resonance is important in terms of efficient energy transfer of external magnetic field energy to a magnetic sphere and subsequent release into other energy forms such as heat via dynamic magnetization dissipation. The quantity of $\bar{Q}$ generated by the resonance of magnetic-vortex is smaller than the $\bar{Q}$ for single-domain state, but it is larger than about several hundred

to several thousand W/g levels of SLP applied to the conventional hyperthermia [15, 16]. Also, for the hyperthermia application, the magnetic-vortex has advantages when implemented technically because the value of the resonant frequency to be applied to the system is smaller than the single-domain state. So, it was worth examining, for resonance cases, $\bar{Q}$ versus all variables (H_{AC}, H_{DC} and α) for different radii.

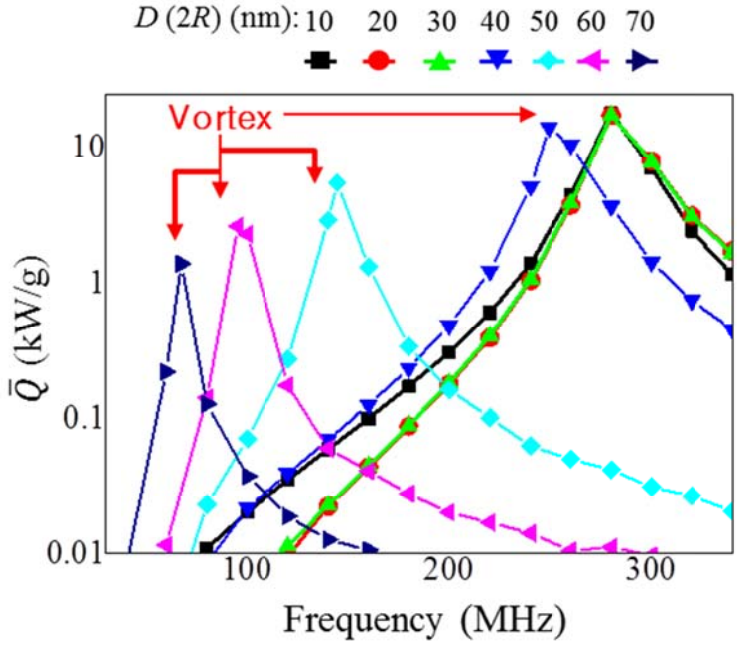

Fig. 4.5. Energy-dissipation rate in steady-state regime as function of frequency of circular-rotating fields for excitation of Py nanospheres of diameter $2R$ = 10 ~ 70 nm with H_{AC} = 5 Oe, H_{DC} = 100 Oe, α = 0.01.

From further micromagnetic simulations, we obtained $\bar{Q}$ at resonance (hereafter noted as $\bar{Q}_{\mathrm{RES}}$) versus H_{AC} (for α = 0.05, H_{DC} = 100 Oe), H_{DC} (for α = 0.05, H_{AC} = 5 Oe) and α (for H_{AC} = 5 Oe, H_{DC} = 100 Oe) for $2R$ = 20 ~ 75 nm. We plotted all the micromagnetic simulation results on Fig. 4.6 and displayed the values of $\langle m_{\Gamma} \rangle$ for each radius. As can be seen from overall image of Fig. 4.6, it is confirmed that as $2R$ increases and $\langle m_{\Gamma} \rangle$ decreases, the $\bar{Q}_{\mathrm{RES}}$ for magnetic vortex state (hereafter noted as $\bar{Q}_{\mathrm{RES,\,v}}$) decreases as compared with $\bar{Q}_{\mathrm{RES}}$ for single-domain state (hereafter noted as $\bar{Q}_{\mathrm{RES,\,s}}$). In addition, the tendency for $\bar{Q}_{\mathrm{RES,\,s}}$ and $\bar{Q}_{\mathrm{RES,\,v}}$ to change when each variable is changes is significantly different. In detail, as shown in Fig. 4.6(a), for the given values of H_{DC} and α, $\bar{Q}_{\mathrm{RES,\,s}}$ increases with H_{AC} up to a certain value of H_{AC} (noted as $H_{\mathrm{AC}}^{\mathrm{th}}$), thereafter becoming saturated even with the further increase of H_{AC} beyond $H_{\mathrm{AC}}^{\mathrm{th}}$. As reported previous study, $H_{\mathrm{AC}}^{\mathrm{th}}$ for $\bar{Q}_{\mathrm{RES,\,s}}$ is αH_{DC} (5 Oe for given condition). Like $\bar{Q}_{\mathrm{RES,\,s}}$, the $\bar{Q}_{\mathrm{RES,\,v}}$ shows a tendency to increase as H_{AC} increases and then saturated. However, $\bar{Q}_{\mathrm{RES,\,v}}$ did not saturate even when H_{AC} reaches $H_{\mathrm{AC}}^{\mathrm{th}}$, and showed a tendency to be saturated after smoothly increasing while H_{AC} increased more than $H_{\mathrm{AC}}^{\mathrm{th}}$. This phenomenon agrees well with the criteria change of reversal dynamics of vortex-core and magnetization of single-domain state described above section. By pinning other variables and changing and

changing the H_{DC}, it is more clearly confirmed that the $\overline{Q}_{RES,\,s}$ and $\overline{Q}_{RES,\,v}$ change in different ways. As shown in Fig. 4.6(b), for the given values of H_{AC} and α, $\overline{Q}_{RES,\,s}$ and $\overline{Q}_{RES,\,v}$ increases with H_{DC} up to a certain value of H_{DC} (noted as H_{DC}^{th}), thereafter $\overline{Q}_{RES,\,s}$ becomes saturated while $\overline{Q}_{RES,\,v}$ decreases with the further increase of H_{DC}.

The aspect where $\overline{Q}_{RES,\,v}$ changes by H_{DC} seems to be affected by complex non-linear dynamics of vortex-core. As shown in Fig. 4.6(b), for the case of $\overline{Q}_{RES,\,v}$ decreases with the H_{DC}, the $\overline{Q}_{RES,\,v}$ gradient of 40 nm diameter which is closest to the size of the single-domain is steepest, and the absolute value of the $\overline{Q}_{RES,\,v}$ gradient gradually decreases as the particle size increases. In the case of particles larger than 70 nm, the $\overline{Q}_{RES,\,v}$ gradient for $H_{DC} > H_{DC}^{th}$ condition became almost zero, showing a trend similar to that of $\overline{Q}_{RES,\,s}$. Also in the Fig. 4.6(c), it was confirmed that $\overline{Q}_{RES,\,v}$ reacts complicatedly to external variables. In Fig. 4.6(c), we plotted the $\overline{Q}_{RES,\,s}$ and $\overline{Q}_{RES,\,v}$ versus α for H_{DC} = 100 Oe and H_{AC} = 5 Oe. Overall, $\overline{Q}_{RES}$ tended to create a tented shape for α. For the $\overline{Q}_{RES,\,s}$, it was confirmed that the peak of the graph is exactly formed in 0.05 satisfying the $\alpha^{th} = H_{AC}^{th} / H_{DC}^{th}$. However, the peaks of $\overline{Q}_{RES,\,v}$ are formed when α is than 0.05 and its position varies depending on the particle size. In the case of 40 nm sphere with magnetic-vortex, α^{th} is 0.04 and in the

case of 45nm sphere, α^{th} is about 0.05 larger than that of 40 nm sphere. And $\overline{Q}_{RES,\,v}$ shows a tendency to decrease gradually for spheres of diameter greater than 45 nm. The underlying physics of these micromagnetic simulation results will now be explained in comparison with the analytical calculation result of the single-domain state.

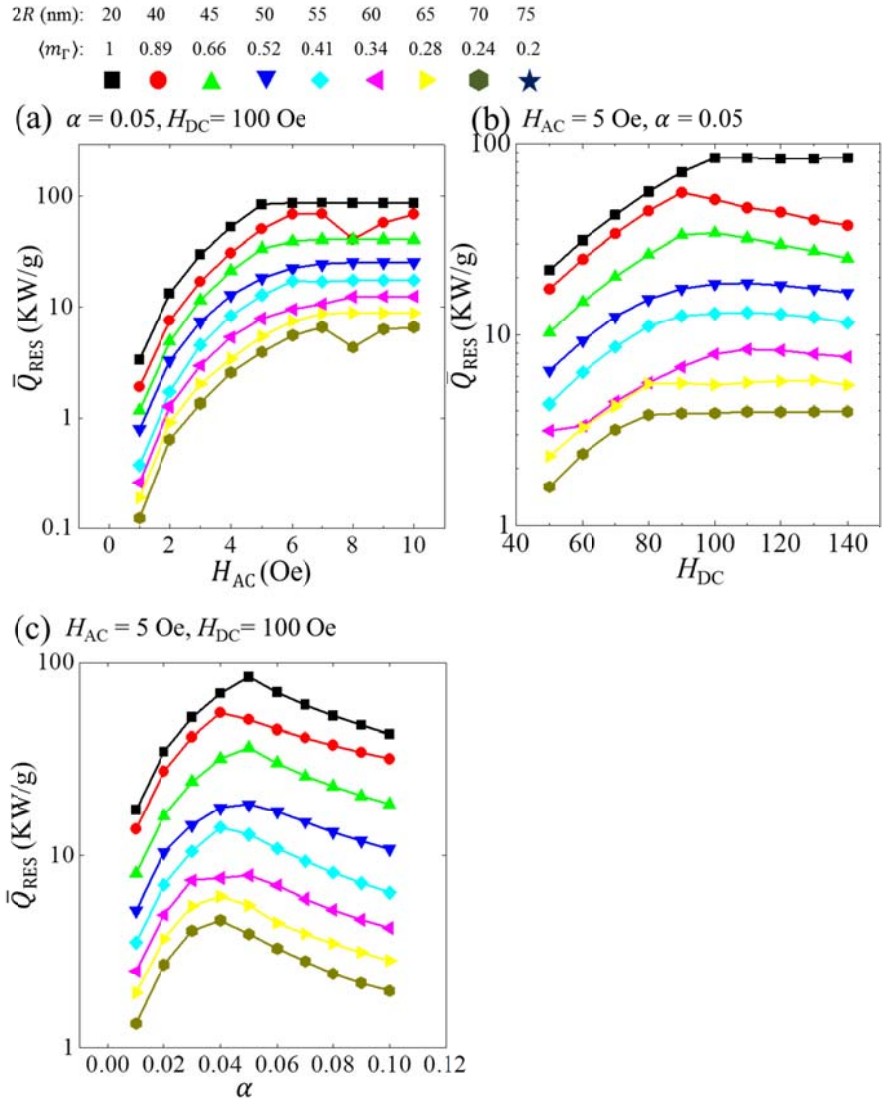

Fig. 4.6. Steady-state energy-dissipation rate at corresponding resonance frequencies for $2R = 20 \sim 75$ nm with as function of (a) H_{AC} ($H_{DC} = 100$ Oe, $\alpha = 0.05$), (b) H_{DC} ($H_{AC} = 5$Oe, $\alpha = 0.05$), and (c) α ($H_{AC} = 5$Oe, $H_{DC} = 100$ Oe).

Semi-Analytical Analysis of $\overline{Q}_{\mathrm{RES}}$

For both the magnetic-vortex and single-domain state, $\overline{Q}$ can be simply determined from the dual power in the steady state assuming $d\varepsilon_{\mathrm{G}}/dt = 0$:

$$\overline{Q} = -\frac{1}{\rho V}\int_{V}\left(\mathbf{M}(t)\cdot d\mathbf{H}_{\mathrm{ext}}(t)/dt\right)dV. \qquad (4.3)$$

Applying the above equation to spin configuration of magnetic-vortex, we can eliminate the integral using $\langle m_{\Gamma}\rangle$ as follows:

$$\overline{Q} = -\frac{M_{\mathrm{s}}\langle m_{\Gamma}\rangle}{\rho V}\int_{V}\left(d\mathbf{H}_{\mathrm{ext}}/dt\cdot\boldsymbol{\Gamma}\right)dV. \qquad (4.4)$$

Now that we focus on the resonance condition, so the external field is expressed as follows: $\mathbf{H}_{\mathrm{ext}} = H_{\mathrm{AC}}\cos\left(\gamma_{\mathrm{eff}}H_{\mathrm{DC}}t\right)\hat{\mathbf{x}} + H_{\mathrm{AC}}\sin\left(\gamma_{\mathrm{eff}}H_{\mathrm{DC}}t\right)\hat{\mathbf{y}} + H_{\mathrm{DC}}\hat{\mathbf{z}}$. Then, we obtain the analytical forms of $\overline{Q}_{\mathrm{RES,v}}$ by inserting $\mathbf{H}_{\mathrm{ext}}$ into Eq. (4.4):

$$\overline{Q}_{\mathrm{RES,v}} = \frac{(M_{\mathrm{s}}\langle m_{\Gamma}\rangle)H_{\mathrm{DC}}H_{\mathrm{AC}}\gamma_{\mathrm{eff}}}{\rho V}(-u_{y,\mathrm{v}}) \qquad (4.5)$$

where the $u_{y,\mathrm{v}}$ is the y-component of $\boldsymbol{\Gamma}$ vector on the rotating frame on the x-y plane [16]. At a value of $\langle m_{\Gamma}\rangle = 1$, $\gamma_{\mathrm{eff}} = \gamma$, and $u_{y,\mathrm{v}} = u_y$, $\overline{Q}_{\mathrm{RES,v}}$ Eq. (4.5) equals $\overline{Q}_{\mathrm{RES,s}}$ for single-domain state. To compare the difference of energy-dissipation rate of the single-domain state and the magnetic-vortex, we calculated the ratio of $\overline{Q}_{\mathrm{RES,s}}$ and $\overline{Q}_{\mathrm{RES,v}}$ as follows:

$$\frac{\overline{Q}_{\mathrm{RES,v}}}{\overline{Q}_{\mathrm{RES,s}}} = \langle m_{\Gamma}\rangle^{2}\frac{u_{y,\mathrm{v}}}{u_y}. \qquad (4.6)$$

In Eq. (4.6), the ratio between $u_{y,\mathrm{v}}$ and u_y is a term that is directly related to the non-linear dynamics of vortex-core. It is difficult to calculate this term analytically, and we assume that this term is directly related to the structural constant of magnetic-vortex, $\langle m_\Gamma \rangle$. Through above assumption, we connect the relation of $\langle m_\Gamma \rangle$ and $u_{y,\mathrm{v}}/u_y$ by $u_{y,\mathrm{v}}/u_y = \langle m_\Gamma \rangle^A$ where the A is the parameter representing the degree of non-linearity of the dynamic motion of the vortex-core. Then Eq. (4.6) is simply modified as $\overline{Q}_{\mathrm{RES,v}}/\overline{Q}_{\mathrm{RES,s}} = \langle m_\Gamma \rangle^{2+A}$. The A could be calculated by fitting $u_{y,\mathrm{v}}/u_y$ obtained by micromagnetic simulation. In Fig. 4.7, we plotted A versus H_{AC}, H_{DC}, and α. As in the case of plotting Fig. 4.5, and Fig 4.6, we fixed one physical constant as a variable and fixed other constants. As shown in Fig. 4.7(a), (b), and (c), the quantities of A show nonsimplicable curves. For each variable, A shows a decreasing curve for H_{AC} (Fig. 4.7(a)), an increasing curve for H_{DC} (Fig. 4.7(b)), and a curve that saturates after increasing for α (Fig. 4.7(c)). Quite interestingly, A represents a peak showing a value of 0.2 for all variables when $H_{\mathrm{AC}} = \alpha H_{\mathrm{DC}}$ is satisfied. Focusing on this, we judged that A has a relationship with proportion of H_{AC} and αH_{DC}, and plotted A against $H_{\mathrm{AC}}/\alpha H_{\mathrm{DC}}$ (Fig. 4.7(d)). As can be seen in Fig. 4.7(d), A appears to be independent of each variable for the condition of $H_{\mathrm{AC}} < \alpha H_{\mathrm{DC}}$. However, with respect to the condition of $H_{\mathrm{AC}} \geq \alpha H_{\mathrm{DC}}$, A represents a unified trend for each variables (H_{AC}, H_{DC} and α). This means that under certain conditions, A is a controllable factor that could be controlled with an integrated variable $H_{\mathrm{AC}}/\alpha H_{\mathrm{DC}}$.

Through the above analysis, the results that the quantities of $\overline{Q}_{\mathrm{RES,v}}$ are smaller than those of $\overline{Q}_{\mathrm{RES,s}}$ as the radii of spheres become larger could be explained well. As shown in Fig. 4.7, the quantities of A is between -0.2 ~ 0.6, so the values of $\overline{Q}_{\mathrm{RES,v}}/\overline{Q}_{\mathrm{RES,s}} = \langle m_{\Gamma} \rangle^{2+A}$ could be estimated as $\langle m_{\Gamma} \rangle^{2.6} \sim \langle m_{\Gamma} \rangle^{1.8}$. As confirmed in Fig. 4.2(d), since $\langle m_{\Gamma} \rangle$ is a function that becomes smaller than 1 as the particle radius increases, $\overline{Q}_{\mathrm{RES,v}}/\overline{Q}_{\mathrm{RES,s}} = \langle m_{\Gamma} \rangle^{2+A}$ decreases as the particle size increases. We can devide the physical origin of the fact that the quantity of $\overline{Q}_{\mathrm{RES,v}}$ is less than that of $\overline{Q}_{\mathrm{RES,s}}$. In the relational expression of $\overline{Q}_{\mathrm{RES,v}}/\overline{Q}_{\mathrm{RES,s}} = \langle m_{\Gamma} \rangle^{2+A}$, $\langle m_{\Gamma} \rangle^{2}$ is a perfect predictable factor that occurs because the total volume specific magnetization and the resonance frequency of the magnetic-vortex are smaller than those of single-domain state. $\langle m_{\Gamma} \rangle^{A}$, on the other hand, is a factor that is difficult to predict if certain condition ($H_{\mathrm{AC}} \geq \alpha H_{\mathrm{DC}}$) is not satisfied, which is directly related to the non-linear dynamics of the vortex-core. This result is meaningful in that it provides a theoretical basis for predicting the energy-dissipation that occurs when the resonance phenomenon of the magnetic-vortex in nanoparticle is applied to bio-applications.

Also, as shown in Fig. 4.6(a), it was indicated that the maximum value of $\overline{Q}_{\mathrm{RES,v}}^{\mathrm{MAX}} = \langle m_{\Gamma} \rangle^{2+A} \overline{Q}_{\mathrm{RES,s}}^{\mathrm{MAX}}$ under the $H_{\mathrm{AC}} \gg \alpha H_{\mathrm{DC}}$ condition is the highest energy-dissipation rate at resonance for a given nanosphere in the vortex state with intrinsic damping parameter and static field strength H_{DC}. The quantity of $\overline{Q}_{\mathrm{RES,v}}^{\mathrm{MAX}}$ for

magnetic-vortex Py particles can reach 10^3 – 10^4 W/g, which is one or two orders of magnitude smaller than the $\overline{Q}_{\mathrm{RES,s}}^{\mathrm{MAX}}$ values of 10^4 – 10^5 W/g for resonant spin excitation of single-domain state. (Table. 4.1). However, this quantity of $\overline{Q}_{\mathrm{RES,v}}^{\mathrm{MAX}}$ is one two orders of magnitude larger than the typical SLP values of 10^2 – 10^3 W/g for magnetic hyperthermia based on conventional mechanisms [15-18]. The Resonant Vortex-core Excitation (RVE) model proposed in this study has the advantages of the Resonant Spin Excitation (RSE) model against the existing model (Linear Response Theory and Storner-Wohlfarth model) for conventional hyperthermia. The one of the advantage of the Resonant Vortex-core Excitation (RVE) model proposed in this study is its utilization of resonant magnetization excitations by externally controllable magnetic fields; the models for conventional hyperthermia, contrastingly, are associated with the intrinsic characteristics of materials (e.g., the relaxation time and the magnetic anisotropy field) as key factors in energy-dissipation. In our RVE model, the maximum energy-dissipation rate can be achieved and readily controlled using only H_{AC} and H_{DC}, whose strengths are as small as 10^{-2} — an order of magnitude smaller than those of the conventional models — in order to obtain high values (up to 10^3 – 10^4 W/g) at resonance when tuning the oscillating field frequency to the resonance frequency. In addition, the RVE model has several advantages over the RSE model for single-domain state. As reported in previous studies, the nanoparticles of magnetic-vortex state are known to be advantageous for bio-medical applications because of their small remanence and less aggregation than nanoparticles with single-domain state. For RVE, it is also possible to circumvent the technical problem of

applying the high frequency magnetic field by reducing the resonance frequency of the precession motion of the vortex-core by controlling the size of the particles.

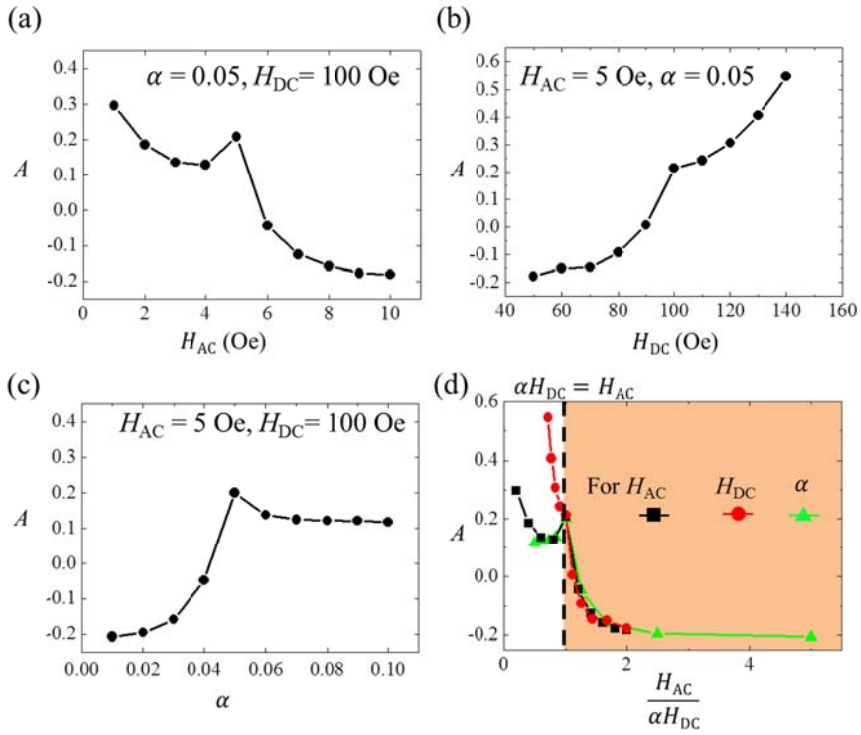

Fig. 4.7. A parameter at corresponding resonance frequencies for $2R = 20 \sim 75$ nm with as function of (a) H_{AC} (H_{DC} = 100 Oe, $\alpha = 0.05$), (b) H_{DC} (H_{AC} = 5 Oe, $\alpha = 0.05$), (c) α (H_{AC} = 5Oe, H_{DC} = 100 Oe), and (d) unified variable $H_{AC}/\alpha H_{DC}$.

Model	LRT and SWM[a]	RSE[b]	RVE[c]
Mechanism	Thermal-fluctuation-dominated relaxation, magnetic anisotropy	Resonant precession motion of singl-domain	Resonant precession motion of magnetic vortex-core
Main factor	τ_R, H_K	α, H_{DC}	α, H_{DC}
Particle size, D	D < Single-domain limit	Super-paramagnetic limit < D < Single-domain limit	Single-domain limit < D < multi-domain limit
Oscillating field Frequency (MHz)	0.01 ~ 1	100 ~ 1000	10 ~ 300
Oscillating field amplitude (Oe)	100 ~ 1000	1 ~ 10	1 ~ 10
Aggregation	Almost none	Concerned	Almost none
Order of SLP (W/g)	~ 1000	~ 10,000 – 100,000	~ 1000 – 10,000

[a]Reference [19]

[b]Reference [chapter 3 (unpublished)]

[c]Present study

Table 4.1. Comparison of characteristics of three models.

4.3.3. Consideration on Influence of Temperature

In this thesis, we studied energy dissipation phenomenon of soft-magnetic nanospheres in the single-domain state and magnetic-vortex state with the aim of application to magnetic hyperthermia at room temperature. However, it is assumed that the dynamics of the nanoparticle magnetic moment is governed by the deterministic LLG equation at 0 K. In this section, we want to discuss theoretically and experimentally whether this assumption is valid.

Theoretically, it is well known that the thermal fluctuations do not play an important role in the dynamics of **m** if the themal energy k_BT (k_B is the Boltzmann constant, T is the absolute temperature) is much smaller than the energy scale of system [19]. For a spherical isotropic system, the driving force that generates magnetization dynamics is Zeeman energy. From this, it follows that the thermal energy can be neglected if $\kappa = E_{\text{Zeeman}} / k_{\text{B}}T \gg 1$. When the strength of the magnetic field is 100 Oe and the rotating field strength is 5 Oe, Zeeman energy density obtained by simulation and analytical calculation for permalloy nanoparticle is calculated as about $MH = 8600$ J/m^3. Then κ at body temperature is expressed as $\kappa = 1.05 \times 10^{24} d^3$ where the d is diameter of sphere. According to the above formula, when the particle diameter exceeds about 21.2 nm, the κ exceeds 10. Then, the thermal fluctuation can be ignored to some extent under the condition of $21.2 < d(nm)$. Since the cancer cells die even when the body temperature rises by 5 to 10 K, the change range of T is about 315 to 330 K [20]. By contrast, the Zeeman energy could be increase several times

depending on the strength of the magnetic field and the size of the particles. Therefore, assuming an actual application, Zeeman energy could be much larger than thermal fluctuation, and the above assumption is sufficiently rigorous. These rigorous estimations clearly show that the description of the dynamics of nanoparticle magnetic moments by the deterministic LLG equation is quite justified, and this approach can be used even at body temperature.

In addition, there are experimental evidences that the dynamics of magnetization generated at a temperature above the room temperature coincides well with the micromagnetic simulation and analytical calculation at 0 K. We have reported several room temperature experiments on the dynamics of magnetic vortex which is unique nanostructure formed in the nano-disc [21-23]. All experiments were carried out at room temperature but were found to be in good agreement with the results calculated by the micromagnetic simulation performed at 0 K. For instance, we report on the direct experimental demonstration, by means of time-resolved Scanning Transmission X-ray Microscopy (STXM), of collective dynamics of spins inside nano-discs interacting with each other in [22]. In this report, the resonantly excited collective motions of spins inside the nano-discs were described very well as results of analytical derivation, numerical calculation and micromagnetic simulation at 0 K. Since the magnetic resonance phenomenon is explained well with the calculation result at 0 K in a very complicated system composed of five nano-discs at room temperature, the resonantly excited mode of magnetic nanoparticle is expected that it agrees well with the calculation results at 0 K.

4.4. Reference

[1] R. C. O'Handley, Modern Magnetic Materials: Principles and Applications. (Wiley, 1999).

[2] J. M. D. Coey, Magnetism and Magnetic Materials. (Cambridge University Press, 2010).

[3] A. Trabesingle, Nature **435**, 1173 (2005).

[4] A. G. Webb, Introduction to Biomedical Imaging. (Wiley-IEEE Press, 2002).

[5] T. Devolder, and C. Chappert, Eur. Phys. J. B **36**, 57 (2003).

[6] S. K. Kim, K. S. Lee, Y. S. Yu, and Y. S. Choi, Appl. Phys. Lett. **92**, 022509 (2008).

[7] S.-K. Kim, M.-W. Yoo, J.-H. Lee, Y. Gaididei, V. P. Kravchuk, and D. D. Sheka, Sci. Rep. **5**, 11370 (2015).

[8] S.-K. Kim, M.-W. Yoo, J. Lee, J.-H. Lee, and M.-K. Kim, Sci. Rep. **6**, 31513 (2016).

[9] M.-K. Kim et al., Appl. Phys. Lett., **105**, 232402 (2013).

[10] T. Schrefl and J. Fidler, J. Magn. Magn. Mater. **155**, 389 (1996).

[11] A. S. Szalay, J. Gray, G. Fekete, P. Z. Kunszt, P. Kukol, and A. Thakar, arXiv preprint cs/0701164 (2007).

[12] C. Kittel, J. Phys. Radium **12**, 291 (1951).

[13] Osborn, Phys. Rev. 67, 351 (1945).

[14] T. Roubíček, G. Tomassetti, and C. Zanini, J. Math. Anal. Appl. **355**, 453

(2009).

[15] R. Hiergeist, W. Andrä, N. Buske, R. Hergt, I. Hilger, U. Richter, and W. Kaiser, J. Magn. Magn. Mater. **201**, 420 (1999).

[16] X. Wang, H. Gub and Z. Yang, J. Magn. Magn. Mater. **293**, 334 (2005).

[17] B. Mehdaoui, A. Meffre, L.-M. Lacroix, J. Carrey, S. Lachaize, M. Respaud, M. Gougeon, and B. Chaudret, J. Appl. Phys. **107**, 09A324 (2010).

[18] J. Carrey, B. Mehdaoui, and M. Respaud, J. Appl. Phys. **109**, 083921 (2011).

[19] T. Lyutyy, S. Denisov, A. Y. Peletskyi, and C. Binns, Phys. Rev. B **91**, 054425 (2015).

[20] Y. -S. Yu, D. –S. Han, M. –W. Yoo, K. -S. Lee, Y. –S. Choi, H. Jung, J. Lee, M. –Y. Im, P. Ficher, and S. –K. Kim, Sci. Rep. **3**, 1310 (2012).

[21] D. –S. Han, A. Vogel, H. Jung, K. –S. Lee, M. Weigand, H. Stoll, G. Schütz, P. Ficher, G,. Meier, and S. –K. Kim, Sci. Rep. **3**, 1038 (2013).

[22] H. Jung, Y. –S. Choi, K. –S. Lee, D. –S. Han, Y. –S. Yu, M. –Y. Im, P. Ficher, and S. –K. Kim, ACS NANO, **5**, 3712 (2012).

Chapter 5

Measurement of Energy-dissipation Caused by Spin Dynamics

5.1. Introduction

In the previous chapters, we studied the magnetization dynamics and related energy-dissipation rate of Py magnetic nanospheres in the single-domain state and magnetic-vortex state, as resonantly excited by rotating magnetic fields under given static magnetic fields. And it is expected that the measurement of energy-dissipation caused by resonance in those systems could be very meaningful. However, for various reasons it is difficult to measure energy-dissipation caused by resonance phenomenon using Py nanoparticles. First, it is not easy to synthesize well-defined Py nanoparticles of size and shape. As reported by our previous results [1], the permalloy nanoparticles could by synthesized using typical polyol method. The shape of prepared Py nanoparticles was almost sphere. However, the created particles could not be considered to be perfect

spheres. It is possible that the demagnetization field that occurs, rather than the perfect sphere (our system), has a crucial effect on the spin dynamics, so that the desired resonance phenomenon cannot be observed. In addition, it is very difficult to implement a technique of applying an alternating magnetic field of a frequency of MHz range to an appropriate area in a current laboratory environment.

To overcome these experimental difficulties, we proposed a new experimental design that indirectly estimates energy-dissipation of magnetic nanoparticles. First, we used iron oxide or doped (Ni) iron oxide nanoparticles instead of a permalloy nanoparticles, which is not easy to synthesize well defined spherical shape. From a theoretical point of view, we have assumed that the resonantly excited magnetization dynamics in superparamagnetic nanoparticles are same with spin dynamics of single-domain state at room temperature. The validity of this assumption is discussed below. The magnetization dynamics that occur when superparamagnnetic particles interact with each other at close distances may be different from when the particles are independent. Therefore, it is required to apply silica coating to the particles. The synthesized nanoparticles can be contacted in solid form with an electrode specifically designed to apply AC magnetic field. From the samples, we can measure the energy dissipated accordingly in a frequency range of up to several GHz using a vector network analyzer (VNA) under DC magnetic fields [2]. We provide a schematic illustration of such an *in-vitro* experiment in Fig. 5.1.

In short, we identify the existence of the energy-dissipation of superparamagnetic nanoparticles from Vector network analyzer–ferromagnetic resonance (VNA-FMR) experiments and compare the results with analytical calculations. From the

experiments and calculations, we observed energy-dissipation with resonantly excited spin dynamics.

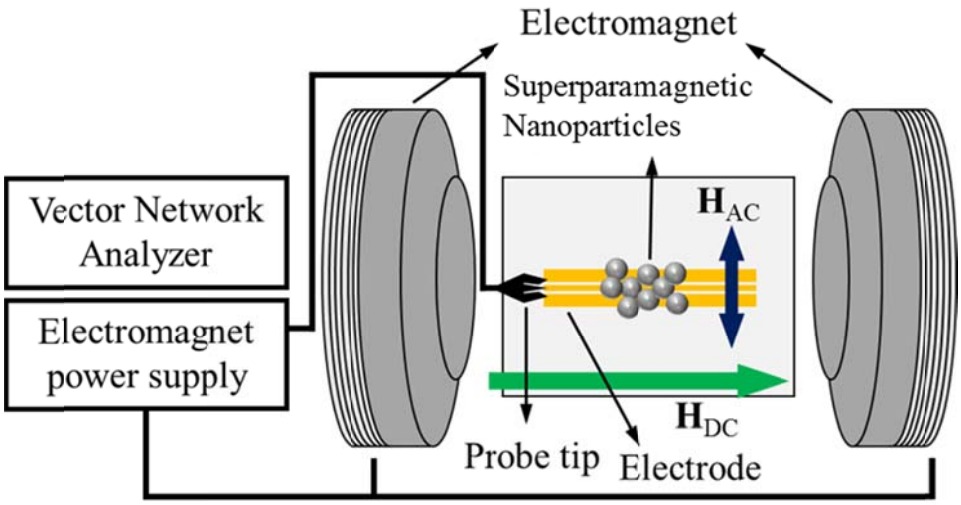

Fig. 5.1. Schematic illustration of experimental design for measurement of the energy-dissipation of nanoparticles.

5.2. Assumption and Validity

In this section, we discuss the validity of replacing superparamagnetic nanoparticles (Fe_3O_4 or doped Fe_3O_4) with single-domain nanoparticles (Py) for experiment. As shown in Fig. 5.2, when static field is applied to superparamagnetic nanoparticle, spins in a random direction due to thermal fluctuation is directed in the direction of static field to form the overall magnetic momentum of particle. If the responses of induced magnetization of superparamagnetic nanoparticles react to the external AC magnetic field in the same way as the single-domain state of the Py nanoparticles, then we can conclude that the physical origins of the energy-dissipation occurring in the superparamagnetic nanoparticles could be treated to the same with single-domain state. Looking at the Ref 3, they reported the resonance frequency of superparamagnetic nanoparticles varying DC magnetic field. The characteristic frequency of induced magnetization for superparamagnetic nanoparticle is given by

$$\omega_{\mathrm{RES,superpara}} = \gamma\left[H_{DC} + 2\frac{K}{M_s}\xi\right]. \qquad (5.1)$$

where the K is anisotropy constant of iron oxide and ξ is the complex variable which consists of langevin functions with temperature, Gilbert damping constant, anisotropic axis as variables. As the temperature increases, the complex variable ξ decreases quickly. When the temperature reaches critical value (Above room temperature for iron oxide), the characteristic frequency of induced magnetization for superparamagnetic nanoparticle is given by

$$\omega_{\mathrm{RES,superpara}} = \gamma H_{DC}. \qquad (5.2)$$

Eq. 5.2 is exactly the same as the characteristic frequency of a Py nanoparticle in which a single-domain state is formed. Under appropriate temperature conditions, superparamagnetic nanoparticles of iron oxide material exhibit the same spin-dynamic behavior as single-domain particle of permalloy material, and thus the assumption of this experiment is reasonable.

As can be seen from Eq. 5.1, the superparamagnetic nanoparticles generate resonance phenomena similar to Py nanosphere as K become smaller. Therefore, we conducted experiments using $NiFe_2O_4$ particles with the smallest K among the superparamagnetic nanoparticles of selectable materials.

Based on this assumption, we estimate the resonance energy-dissipation, $\bar{Q}_{\mathrm{RES}}$, for both Py and $NiFe_3O_4$ using the analytical calculation reported in chapter 3 and 4. Then the $\bar{Q}_{\mathrm{RES}}$ is given by following equation:

$$\bar{Q}_{\mathrm{RES}} = M_{\mathrm{ave}}\left(\tfrac{1}{\alpha}\gamma {H_{\mathrm{AC}}}^2 / \rho\right), \qquad H_{\mathrm{AC}} < \alpha H_{\mathrm{DC}} \tag{5.3}$$

where the $\underline{M}_{\mathrm{ave}}$ is average magnetization for nanosphere. Note that the M_{ave} is $M_{\mathrm{s}}\langle m_{\mathrm{r}}\rangle$ for magnetic-vortex state. The systematic data of M_{ave} for the static field of 100 Oe are not reported at present, so M_{ave} is qualitatively obtained using the results of previous studies [4].

In the Fig. 5.3, the analytical calculation results of $\bar{Q}_{\mathrm{RES}}/M_{\mathrm{s}}$ for Py and doped iron oxide spheres are plotted as a function of diameter. In the cases of superparamagnetic spheres (0 nm < $2R$ < 20 nm), both Py nanosphere with zero-anisotropy and doped iron oxide sphere with anisotropy have energy-dissipation due to resonance phenomenon. Because the M_{ave} is increases with the size of sphere in the

superparamagnetic region, the $\overline{Q}_{\mathrm{RES}}/M_{\mathrm{s}}$ increases with 2*R*. The energy-dissipation rate due to resonance in superparamagnetic nanoparticles is clearly smaller than the single-domain state, but is expected to be higher than conventional hyperthermia. However, in the region where the sizes of nanosphere for single-domains and magnetic vortex are occur, the $\overline{Q}_{\mathrm{RES}}$ cannot is cannot defined for the iron oxide series materials with non-zero anisotropy energy.

In this section, we discussed whether the superparamagnetic state could be treated as a single-domain state, and derived the expected results of energy-dissipation rate due to resonance phenomenon. According to the analysis, the anisotropy in the superparamagnetic state in iron oxide series particle behaves as if it is zero-anisotropy by being neutralized by thermal fluctuations (for room temperature). Thus the induced magnetization in superparamagnetic state reacts to external fields as if it were a single-domain in the Py sphere. Although there are parts that need verification experimentally and theoretically, this work provides research methodology into the fundamentals of resonantly excited magnetization dynamics in superparamagnetic magnetic particles and the associated energy dissipation effect, and suggests a highly efficient means of magnetic-hyperthermia-applicable energy dissipation.

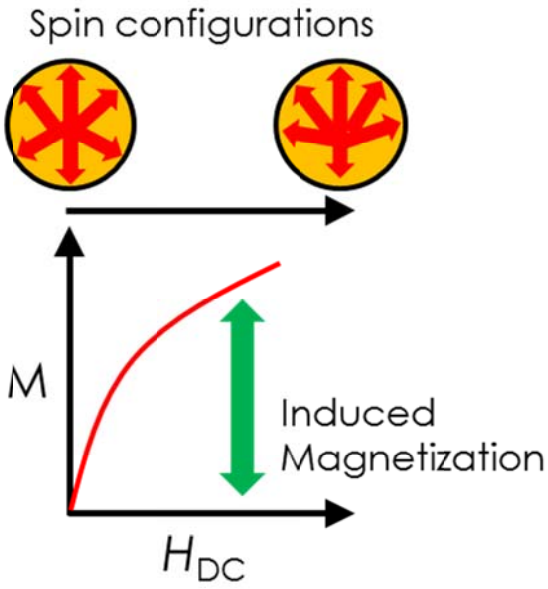

Fig. 5.2. H_{DC} versus induced magnetization curve of superparamagnetic nanoparticles and corresponding spin configurations.

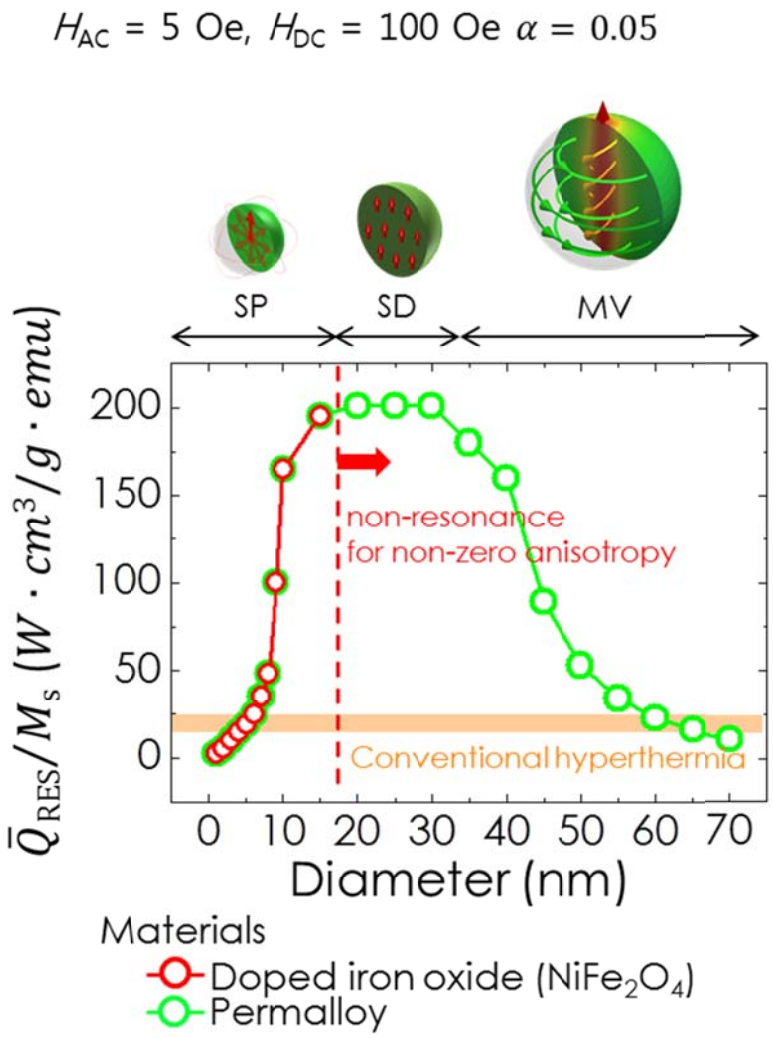

Fig. 5.3. Normalized (by M_s) steady state energy-dissipation rate at room temperature for Py and doped iron oxide nanospheres as function of diameter. The SLP values for conventional hyperthermia are distinguished by the orange color. The static field strength H_{DC} = 100 Oe, oscillating field strength H_{AC} = 5 Oe and damping constant α = 0.05 were used for all of the calculations shown in this figure.

5.3. Method

5.3.1. Experimental Method

In this study, we used the VNA-FMR method to observe energy-dissipation in $NiFe_3O_4$ nanoparticles. The $NiFe_2O_4$ ($2R$ = 12 nm) nanoparticles were prepared by Prof. Cheon's lab. The transmission electron microscope (TEM) images of sphere nanoparticles are shown in Fig. 5.4. As shown in the TEM image, the $NiFe_2O_4$ nanoparticles are capped by silica shells. Each particle cannot interfere with each other by this silica shell. The measurements were carried out using an Agilent E5071B VNA working at frequencies up to 20 GHz. A VNA-FMR inductive technique was used to determine the FMR frequency and the line width. As shown in Fig. 5.4, the nanoparticles were dropped (liquid form) and dried on top of the coplanar waveguide (CPW) (see Fig. 5.5). As shown in the Fig. 5.5(c), $NiFe_2O_4$ nanoparticles were deposited in the cluster forms on the CPW. The measurements were made by sweeping the frequency of an excitation signal, which was provided by VNA port 1 that runs through a CPW creating an RF field component (under 1 Oe), in the sample. This geometry ensures that the precession of the magnetization around the superparamagnetic state is small. In order to evaluate the energy-dissipation, we measured the reflection signal in port 1, which is known as S_{11}. We set an input power of about 2 dbm at room temperature and averaged S_{11} 100 times. The static field strength H_{DC} was increased 0 to 3000 Oe. The signal was measured in the frequency range of 0 to 20 GHz.

5.3.2. Analytical Calculation Method

To estimate the energy-dissipation of the superparamagnetic $NiFe_2O_4$ nanoparticles obtained from the VNA measurement, we additionally modified analytical forms of energy-dissipation. The energy-dissipation could be analytically solved by adding a given condition (linear polarized field, weak field strength condition) to the solution of the LLG equation given in Chapter 3, given below [5]:

$$\bar{Q} = \frac{1}{V} M_{\text{ave}} \frac{\alpha\gamma H_{\text{DC}} {H_{\text{AC}}}^2 \omega^2 \left[(\gamma H_{\text{DC}})^2 + \omega^2 + \alpha^2\omega^2 \right]}{\rho\left[(\gamma H_{\text{DC}})^2 - \omega^2 + \alpha^2\omega^2 \right] + 4\alpha^2\omega^2} \tag{5.4}$$

For the superparamagnetic nanoparticles, we can measure the M_{ave}, γ, and α by experiment. Then, we can use those values to estimate energy-dissipation using Eq. (5.4).

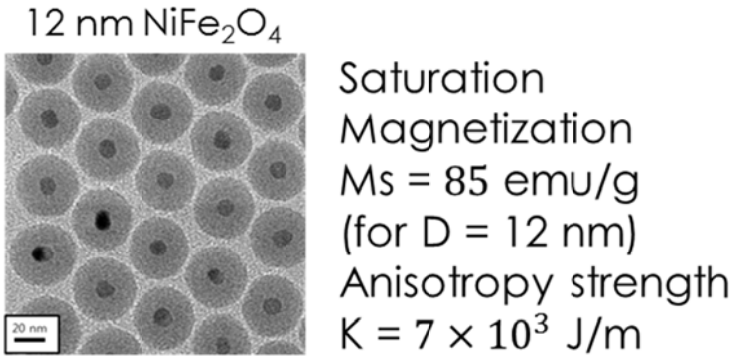

Fig. 5.4.TEM image of $NiFe_2O_4$ nanoparticles capped by silica shells. The magnetic properties of $NiFe_2O_4$ nanoparticles are briefly demonstrated.

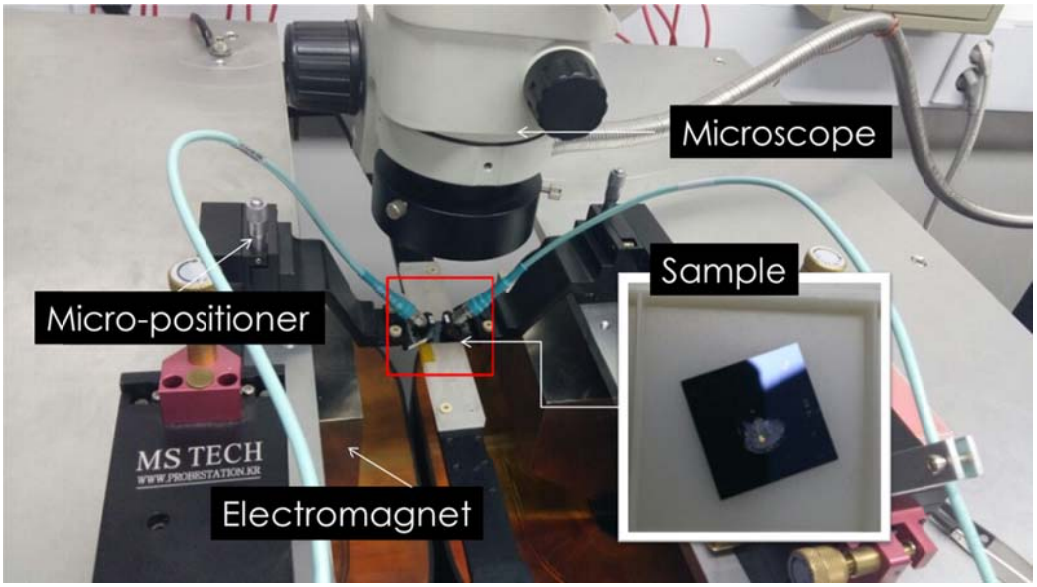

Fig. 5.5. Photograph of the experimental setup of VNA.

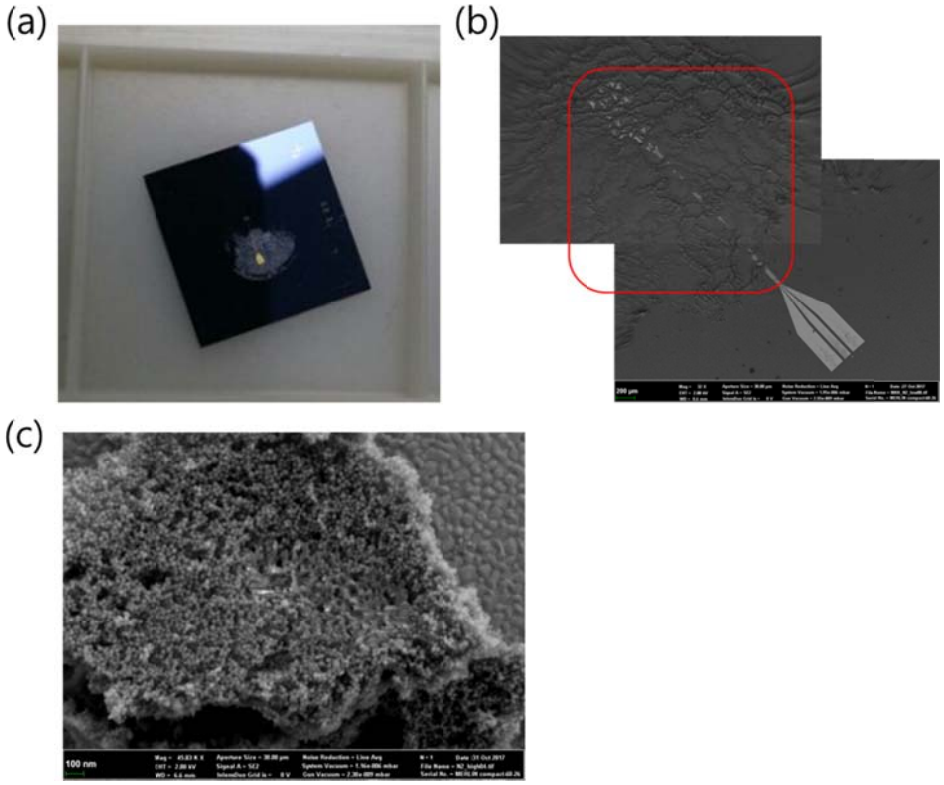

Fig. 5.6. (a) Overview of CPW sample covered by $NiFe_2O_4$ nanoparticles. (b) Low magnification SEM image of sample. (c) High magnification SEM image of sample.

5.4. Results and Discussion

Figure 5.7(a) shows the obtained S_{11} parameter of the $NiFe_2O_4$ superparamagnetic nanoparticles which had a diameter of $2R$ = 12 nm. We plotted the S parameter obtained by increasing increasing H_{DC} at 400 Oe to 200 Oe intervals. The S_{11} curves for each value of H_{DC} showed a peak at a certain frequency and we expected that these peaks would be peaks for the resonance precession of induced magnetization for superparamagnetic nanoparticles. These peaks are plotted for corresponding H_{DC} in Fig. 5.7(b). As shown in Fig. 5.7(b), the resonance frequency is linearly increased with H_{DC}. By calculating the slope of the straight fitting line, we can get the following formula:

$$\omega_{RES} = 0.9\gamma_0 H_{DC} \qquad (5.4)$$

where the γ_0 is defined by the gyromagnetic ratio of Py (which was used for micromagnetic simulations). The reason why the gyromagnetic ratio obtained by experiment shows 10 % difference against the calculation is probably that $NiFe_2O_4$ nanoparticles has thermal fluctuation and anisotropy energy difference from Py. In fact, the gyromagnetic ratio of a substance is obviously different because it is a changing value depending on what the material is [6-8]. And the result shows that the assumption that superparamagnetic nanoparticles will show a resonance phenomenon similar to the permalloy single-domain nanoparticles at room temperature is quite reasonable.

We also plotted Full Width Half Maximums (FMHM) of the curves in Fig. 5.7(a) for the corresponding H_{DC}. The FMHM results are well known to be useful in determining the Gilbert damping constant of the material. For the sphere geometry, the

Gilbert damping constant could be calculated by the equation given below [9]:

$$\Delta f = \alpha\gamma H_{DC}/\pi + \Delta f_0. \quad (5.5)$$

where the Δf is the full width half maximum of S_{11} peak, and Δf_0 is the residual frequency factor which is related to the non-linear effect of spin dynamics. The FWHM obtained by S_{11} parameter is plotted in Fig. 5.7(c). Using Eq. (5.5), the value of α of $NiFe_2O_4$ superparamagnetic nanoparticles was obtained as 0.032 ± 0.0036.

The S_{11} parameter could be expressed as the ratio between dissipated energy and input power from following equation:

$$\Delta S_{11} = 20\log(1 - \bar{Q}/I_0). \quad (5.6)$$

where the I_0 is the input power supplied by VNA system.

To estimate the value of Q, frequency resolved I_0 should be obtained. But frequency resolved I_0 could not be obtained by VNA measurement. The value of I_0 could be expressed as the function of magnetic field:

$$I_0(\omega) = \frac{V'}{2}\frac{H_{AC}{}^2}{\mu}, \quad (5.7)$$

where the V' is the volume affected by magnetic field, and μ is the magnetic susceptibility of system. Because I_0 is proportional to H_{AC}^2, we can solve Eq. 5.6 and qualitatively campare $\bar{Q}/I_0$ with analytical calculation results. The analytical calculation results obtained by Eq. 5.4 and the values of $\bar{Q}/I_0$ obtained by experimentally are plotted in Fig. 5.8. As shown in Fig. 5.8 , the values of $\bar{Q}/I_0$ (Fig. 5.8(a)) are in qualititive agreement with the analytical calculation results (Fig. 5.8(b)).

For both analytical calculation and experimental results, the maximum values of $\bar{Q}/I_0$ were found at $\omega_{\mathrm{RES}} = 0.9\gamma_0 H_{\mathrm{DC}}$, which is almost same with the characteristic frequency of Py nanosphere with single-domain state. In addition, the experimental results show that the height of the peak increases with increasing H_{DC}, and the analytical calculation results show the same shape. These results confirm the fact that the resonance phenomenon of the superparamagnetic nanoparticle amplifies the energy absorption and emission, and it is meaningful that it can be explained by the theory of the energy-dissipation for single-domain state.

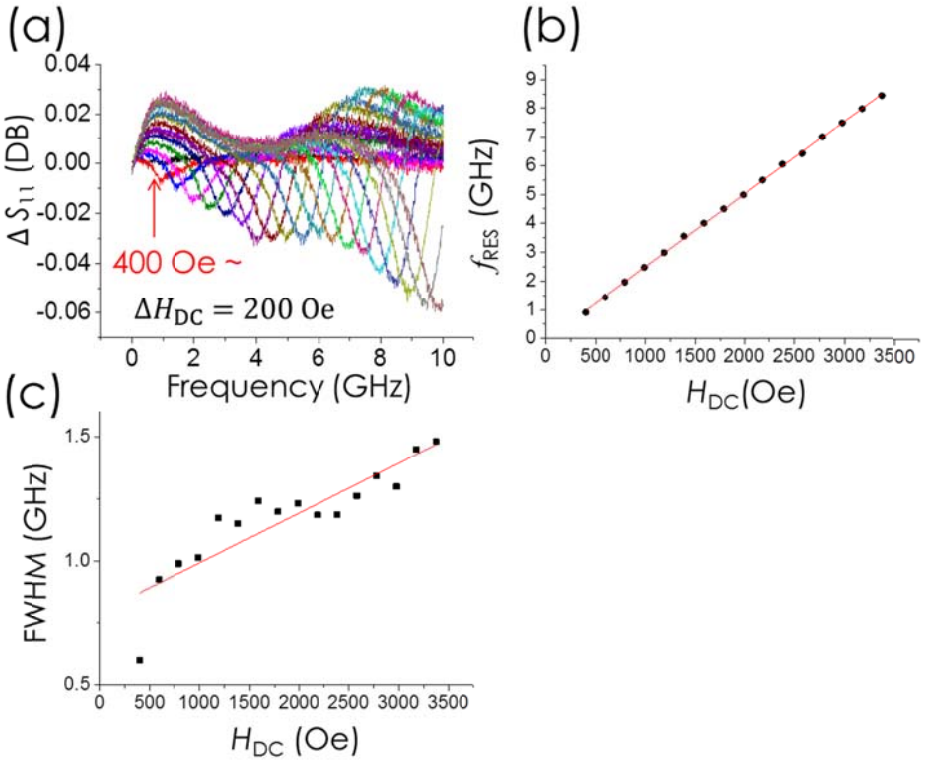

Fig. 5.7. (a) S_{11} parameter obtained by VNA measurement. The data was plotted by increasing H_{DC} at 400 Oe to 200 Oe intervals. (b) The resonance frequency versus H_{DC} obtained by S_{11}. (c) The Full Width Half Maximum values of curves in (a) is plotted as a function of H_{DC} for resonance frequencies.

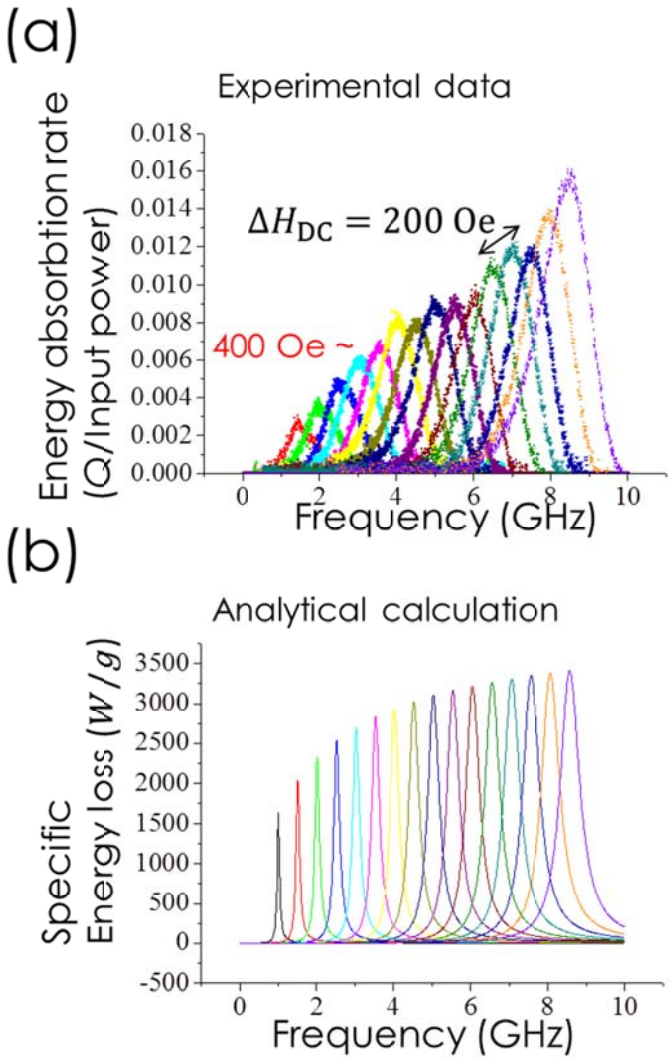

Fig. 5.8. (a) The energy absorbtion rate obtained by VNA measurement as a function of f and H_{DC}. (b) The analytically calculated energy-dissipation rate versus frequency as a function of H_{DC}. The H_{AC} is set to 1 Oe for Fig. (b).

5.5. Reference

[1] M. –K. Kim, P. Dhak, H. –Y. Lee, J. –H. Lee, M. –W. Yoo, J. Lee, K. Jin, A. Chu, K. T. Nam, H. S. Park, S. Aizawa, T. Tanigaki, D. Shindo, M. Kim, and S. –K. Kim, Appl. Phys. Lett. **105**, 232402 (2014).

[2] S. Park, Y. –S. Chung, Y. Kwon, and C. Cheon, Microw. Opt. Technol. Lett. **51**, 2977 (2009)

[3] Y. L. Raikher, and V. I. Stepanov, Zh. Esp. Teor. Fiz. **102**, 1409 (1992).

[4] C. Liu, and Z. J. Zhang, Chem. Mater. **13**, 2092 (2011).

[5] T. Lyutyy, S. Denisov, A. Y. Peletskyi, and C. Binns, Phys. Rev. B **91**, 054425 (2015).

[6] G. G. Scott, Rev. Mod. Phys **34**, 102, (1962).

[7] V. N. Sharma, J. Appl. Phys **36**, 1450 (1965).

[8] J. P. Nibarger, R. Lopusnik, Z. Celinsk, and T. J. Silva, Appl. Phys. Lett. **83**, 93 (2003).

[9] V. Sharma, J. Saha, S. Patnaik, and B. K. Kuanr, AIP Advances **7**, 056405 (2017).

[10] S. S. Kalaricka, P. Krivosik, M. Wu, C. E. Patton, M. L. Schneider, P. Kabos, T. J. Silva, and J. P. Nibarger, J. Appl. Phys. **99**, 093909 (2006).

Chapter 6

Conclusion

In this thesis, we studied energy-dissipation mechanism in soft magnetic nanoelements using excitations of the colletive spin dynamics.

First, we studied the magnetization dynamics and related energy-dissipation rate of soft magnetic nanospheres in the single-domain state, as excited by rotating magnetic fields under given static magnetic fields. The energy-dissipation rate was found to have its maximum value at resonance in cases where the frequency of the rotating magnetic fields is equal to that of the Larmor precession of uniform magnetizations for a given Gilbert damping constant. The resonant energy-dissipation rate in the steady state, $\overline{Q}_{\mathrm{RES}}$, is simply given in terms of H_{AC} and H_{DC} for a given damping constant. For the cases of $H_{\mathrm{AC}} \geq \alpha H_{\mathrm{DC}}$, the quantity of $\overline{Q}_{\mathrm{RES}}$ reaches its maximum value of $\overline{Q}_{\mathrm{RES}}^{\mathrm{MAX}} = \alpha\left(\gamma M_{\mathrm{s}} {H_{\mathrm{DC}}}^{2} / \rho\right)$. This explicit form provides the highest SLP value, on the order of 10^4 – 10^5 W/g, and enables ready controllability by externally applied magnetic fields using single-domain magnetic particles in magnetic hyperthermia applications.

In the next chapter, we studied the magnetization dynamics and related energy-dissipation rate of soft magnetic nanospheres in the magnetic-vortex state, as excited by rotating magnetic fields under given static magnetic fields. The energy-dissipation rate was found to have its maximum value at resonance in cases where the frequency

of the rotating magnetic fields is equal to that of the precession motion of vortex-coreThe resonant energy-dissipation rate in the steady state for magnetic-vortex, $\overline{Q}_{\mathrm{RES,v}}$, is estimated by comparing with energy-dissipation rate of the single-domain state, $\overline{Q}_{\mathrm{RES,s}}$, for all given parameters. The quantities of $\overline{Q}_{\mathrm{RES,v}}$ show a small value when compared with $\overline{Q}_{\mathrm{RES,s}}$, and the ratio is given as $\overline{Q}_{\mathrm{RES,v}} / \overline{Q}_{\mathrm{RES,s}} = \langle m_{\mathrm{r}} \rangle^{2+A}$. Also, the response to the change of each variable is similar to $\overline{Q}_{\mathrm{RES,v}}$ and $\overline{Q}_{\mathrm{RES,s}}$, but the detailed tendency is different. The energy-dissipation rate of magnetic-vortex, $\overline{Q}_{\mathrm{RES,v}}$, provides the SLP value, on the order of 10^3 – 10^4 W/g, and enables ready controllability by externally applied low-frequency magnetic fields using uncluttered magnetic-vortex magnetic particles in hyperthermia applications.

Finally, to investigate energy-dissipation of nanoparticles induced by resonantly excited spin dynamics, we detected the ratio between input power and output power in the magnetic nanoparticles using the VNA-FMR technique. We also have conducted analytical calculations and compared the results with our experimental data. Consequently, we have qualitatively confirmed the energy-dissipation caused by resonance phenomenon in a given system.

This work provides further insights into the fundamentals of resonantly excited magnetization dynamics in magnetic particles and the associated energy dissipation effect, and suggests a highly efficient means of magnetic-hyperthermia-applicable energy dissipation.

Publications

1	S. I. Kim J. H. Choi, C. W. Baik, H. Y. Ahn, Y. S. Lee, J. An, C. –S. Choi, K. Pyun, H. –S. Lee, D. –H. Kwon, M. –K. Kim, M. Kim, and S. Lee, *Electrically driven diffraction grating designed for visible-wavelength region,* IEEE ELECTRON DEVICE LETT. **34**, 84 (2013).
2	M. –K. Kim, P. Dhak, H. –Y. Lee, J. –H. Lee, M. –W. Yoo, J. Lee, K. Jin, A. Chu, K. T. Nam, H. S. Park, S. Aizawa, T. Tanigaki, D. Shindo, M. Kim, and S. –K. Kim, *Self-assembled magnetic nanospheres with three-dimensional magnetic vortex*, Appl. Phys. Lett. **105**, 232402 (2014).
3	S. K. S. Patel, P. Dhak, M. –K. Kim, J. –H. Lee, M. Kim, and S. K. –Kim, *Structural and magnetic properties of Co-doped Gd_2O_3 nanorods*, J. Magn. Magn. Mater. **403**, 155 (2016).
4	P. Dhak, S. K. S. Patel, M. –K. Kim, J. –H. Lee, M. Kim, and S. K. Kim, *Hydrothermal synthesis, structural analysis and room-temperature ferromagnetism of $Y_2O_3:Co^{2+}$ nanorods*, J. Magn. Magn. **408**, 67 (2016).
5	S. –K. Kim, M. –W. Yoo, J. Lee, J. –H. Lee, and M. –K. Kim, *Resonant vortex-core reversal in magnetic nano-spheres as robust mechanism of efficient energy absorption and emission*, Sci. Rep. **6**, 31513 (2016).
6	P. Dhak, M. –K. Kim, J. –H. Lee, M. Kim, and S. K. Kim, *Linear-chain assemblies of iron oxide nanoparticles*, J. Magn. Magn. **433**, 47 (2017).

7	J. –H. Lee, J. Kim, M. –K. Kim, J. Sim, and S. K. Kim, *Single-drystalline Gd-doped $BiFeO_3$* nano wires: R3c-toPn21a phase transition and enhancement in high-coercivity ferromagnetism, J. Mater. Chem. **6**, 526 (2018).
8	S. K. S. Patel, J. –H. Lee, M. –K. Kim, B. Bhoi, and S. K. –Kim, *Structural and magnetic properties of Co-doped Gd_2O_3 nanorods*, J. Magn. Magn. Mater. **403**, 155 (2016).
9	M. –K. Kim, J. Sim, J. –H. Lee, M. Kim, and S.-K. Kim, *Dynamic origin of highly efficient energy-dissipation in soft magnetic nanoparticles in signle-domain state* (submitted).

요약(국문초록)

자성 입자를 이용한 자성 온열 치료 기법은 현재 암 치료 분야에서 활발하게 연구되고 있다. 자성 온열 치료는 자성 나노 입자에 교류 자기장을 걸어서 여러가지 에너지-분산을 열의 형태로 발생시키며 입자의 주변에 있는 암 세포들에 열적 충격을 가하여 파괴시킨다. 자성 온열 치료에서 입자가 열을 발생시키는 메커니즘으로는 닐-브라운 완화 메커니즘과 자기 이력 손실이 대표적이다. 이러한 기존 자성 온열 치료에서 이용되는 에너지-분산 메커니즘에 의해 발생하는 열은 암세포를 죽이기에 충분하지 않아 자성 온열 치료를 상용화하기 위해서는 발생열을 높여야만 한다. 입자가 발생하는 열 효율을 높이기 위해서 다양한 분석 방법을 이용한 연구들이 진행되어 왔다. 그러나 자성 입자가 열을 발생시키는 열 발생 메커니즘에 대해서는 새롭게 연구된 바가 없으며, 결국 여러 가지 연구들에서 자성 입자에 의해 발생하는 열 효율을 향상시키는 정도에는 한계가 있을 수 밖에 없었다. 이에 우리는 자성 입자가 발생시키는 열적인 에너지-분산의 새로운 메커니즘을 제안하였으며, 본 메커니즘은 스핀의 공명 현상을 기반으로 하여 입자의 에너지-분산을 최대화할 수 있게 설계되었다.

첫째로 단-자구 구조가 형성된 연자성 나노구에서 여러가지 다른 세기와 주파수를 가진 자기장을 가하여 발생하는 자화의 비-선형 동역학과 이에 의해 발생하는 에너지-분산에 대해 연구하였다. 우리는 입자에 가해지는 여러가지 변수 (교류 자기장 세기, 직류 자기장 세기, 길버트 감쇄 상수) 미소 자기 전산 모사 방법을 이용하여 연자성 구에서

발생하는 자화의 동역학을 규명하는 한 편, 분석적 방법을 이용하여 계가 정상상태일 때 발생하는 에너지-분산을 연구하였다. 모든 전산 모사 결과와 분석적인 계산 결과는 일치하는 것을 확인하였다. 연구 결과 공명 현상에 의해 고 효율의 에너지 분산이 발생하였으며, 이러한 고 효율 에너지 분산이 발생하는 메커니즘은 기존의 자성 온열 치료에서 제시하는 메커니즘과 확실히 다른 것이었다.

또한 공명 현상을 응용한 에너지-분산 연구를 단-자구 구조에서 자기-소용돌이 구조로 확장하였다. 미소 자기 전산 모사 방법과 준 분석적인 방법을 이용, 주어진 시스템의 모든 변수를 변화시키며 단-자구 구조와 자기-소용돌이 구조에서 발생하는 스핀 동역학 및 에너지-분산의 시간에 대한 변화의 유사 점과 차이 점을 비교하였다. 자기 소용돌이에서 공명 현상에 의해 발생하는 에너지-분산은 단자구에 비해 작았으며, 이러한 에너지-분산의 크기 관계는 입자의 평균 자화량인 $\langle m_r \rangle$ 과 직접적으로 연관이 있다.

마지막으로 자성 입자 내에서 스핀-동역학에 의해 발생하는 에너지-분산을 벡터 네트워크 분석기를 이용해 확인하고 결과를 분석적 계산과 비교하였다. 본 실험으로 나노 입자 내의 스핀들에 의한 공명 현상 및 공명에 의해 발생하는 에너지-분산이 존재함을 확인했고 계산 결과와도 정성적으로 일치하는 것을 확인했다.

본 연구는 입자 내의 자화 동역학 및 관련된 에너지-분산 효과를 연구하여 고 효율 자성 온열 치료에 응용 가능한 새로운 에너지-분산 메커니즘을 제시하였다는 데에 의의가 있다.

주요어: 자성 입자, 에너지-분산, 공명 현상, 단−자구 구조, 자기 소용돌이 구조, 미소 자기 전산 모사, 벡터 네트워크 분석기.

학 번: 2011-20626